

Rapid Dissipative Ground State Preparation at Chemical Transition States

Thomas W. Watts,^{1,2,*} Soumya Sarkar,^{2,†} Daniel Collins,² Nam Nguyen,³ Luke Quezada,⁴ Michael J. Bremner,² and Samuel J. Elman^{2,‡}

¹*HRL Laboratories, LLC, Malibu, CA, USA*

²*Centre for Quantum Software and Information, School of Computer Science, Faculty of Engineering & Information Technology, University of Technology Sydney, NSW 2007, Australia*

³*Applied Mathematics, Boeing Research & Technology, Huntington Beach, USA*

⁴*Media Arts + Practice Division, University of Southern California, Los Angeles, CA 90089, USA*

Simulating chemical reactions exhibits a pronounced unevenness in computational difficulty: while equilibrium reactant and product geometries are often tractable, transition-state (TS) geometries frequently display strong multi-reference character that challenges both classical solvers and coherent quantum state-preparation methods. We introduce a dissipative continuation protocol for preparing electronic ground states along reaction paths that targets this transition-state bottleneck. Starting from a warm start at a tractable geometry, the algorithm transports the state along a discretized reaction coordinate using orbital-aligned Hamiltonians and engineered dissipative cooling primitives that repeatedly contract population into the instantaneous low-energy sector. We prove that, for reaction paths satisfying a Lipschitz smoothness condition and a localized downward-drift (ETH-motivated) mixing assumption within the relevant energy window, the ground state at a target geometry can be prepared to energy error ϵ_E with total gate complexity $\tilde{O}(C_{DK}^2 N_o / \epsilon_E)$, where C_{DK} quantifies ground-state rotation along the path. This identifies a structured chemical regime in which dissipative continuation provides a controlled and scalable route to ground-state preparation at strongly correlated transition-state geometries.

I. INTRODUCTION

Accurate electronic ground states along a reaction path are essential for predicting chemical reactivity and thermodynamic observables. On a typical potential energy surface (PES), reactants and products correspond to metastable basins of attraction: collections of nuclear geometries that relax under energy minimization to distinct local minima representing chemically identifiable species, and are often well approximated by tensor-network solvers and other classical methods. In contrast, transition-state (TS) geometries lie near the dividing surface between these basins, where bonds are formed and broken and electron–electron correlations become strong. In this regime, classical solvers are often unreliable or prohibitively expensive. As a result, reaction paths typically exhibit a highly uneven computational profile, with most geometries being classically tractable while the TS region forms a computational bottleneck.

In this work, we present dissipative evolution, a quantum algorithm for preparing ground states at strongly correlated TS geometries along reaction paths. At a high level, the algorithm approximates the evolution along a reaction path from a system with an easy-to-prepare ground state to a system of interest by applying dissipative cooling primitives at a sequence of successive geometries along the discretized reaction path. The flexibility of the approach lies in the choice of reaction path, which can

be modified and optimized for desirable properties and in the design of the cooling primitive. For example, one may consider simple linear paths passing through the TS, as in traditional adiabatic simulation [2] or chemically motivated choices such as the minimum-energy path (MEP) on the potential energy surface [3]. In this work, we focus on preparing the TS ground states along the MEP, as these geometries are of primary interest in quantum chemistry; however, our algorithm will apply to any path which is smooth.

We show that, provided the Hamiltonian and its ground state vary smoothly along the reaction path—a property we quantify in terms of the smoothness of the pathway—ground states at transition-state geometries can be prepared with only polynomial overhead relative to the cost of preparing ground states at equilibrium reactant or product geometries. Specifically, in addition to the cost of state preparation, our algorithm has a runtime complexity bounded above by $\tilde{O}(N_o^3 / \epsilon_E)$ where ϵ_E is the final energy error and N_o is the number of (spatial/spin) orbitals. In practice, the complexity of our algorithm depends highly on the smoothness of the Hamiltonian along reaction paths which can be quantified with a *Davis-Kahan*-like constant C_{DK} . Physically, this constant quantifies how quickly the ground state “rotated” along the reaction path. Our algorithm’s complexity in these terms becomes $\tilde{O}(C_{DK}^2 N_o / \epsilon_E)$. Therefore, our algorithm obtains a substantial speed-up over the worst-case complexity bound precisely when the reaction path admits a smoothly varying Hamiltonian, and thereby, a smoothly evolving electronic ground state which is typically the case within the Born-Oppenheimer regime.

* thomas.watts@student.uts.edu.au

† soumya.sarkar@student.uts.edu.au

‡ samuel.elman@uts.edu.au

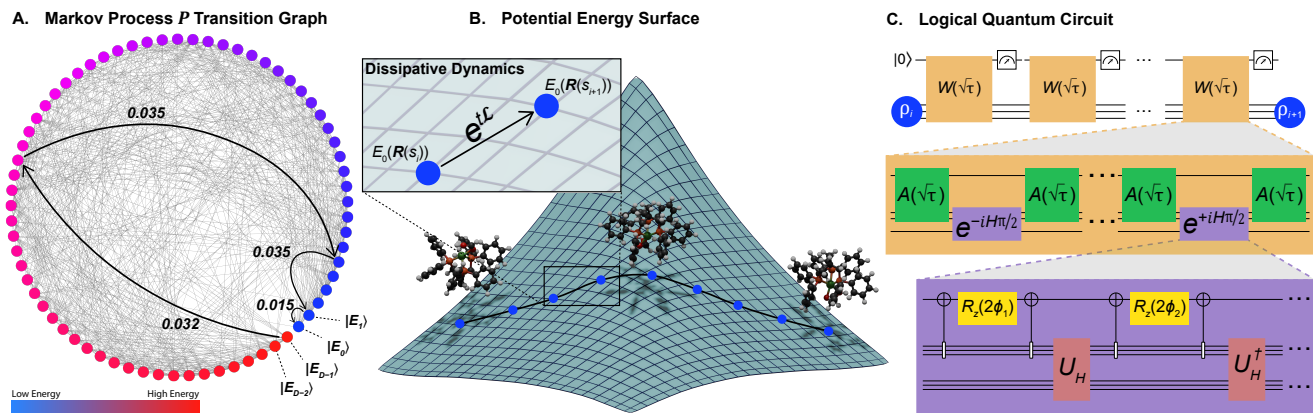


FIG. 1. (a) The transition digraph associated with the Lindbladian-induced Markov process P depicting the longest canonical path between an excited state and the ground state; this path length indicates that the Markov process will mix rapidly. The underlying transition graph is a numerical example of H_4 molecule at its multi-reference square geometry (see Figs. 3 and 4); the transition graph has the same number of nodes as the FCI dimension $D = \binom{2N_o}{N_e} = 70$ for a CAS(4, 4) active space in the STO-3G orbital basis. The values above each arrow are the transition probabilities from $|E_j\rangle \rightarrow |E_k\rangle$, $P_{j \rightarrow k}$ along the longest path; in this case the longest path is $|E_{D-1}\rangle \rightarrow |E_0\rangle$ with length $\ell = 4$ whose transition probabilities are bounded below by $P_{j \rightarrow k} \geq 0.01$. (b) An example of a Ru-based carbon-capture catalyst reaction VIII \rightarrow VIII-IX (transition state) \rightarrow IX of the multi-step reaction mechanism for CO_2 reduction [1]; the 2D potential energy surface (PES) is representative of a more complex, multi-dimensional mechanism underlying the reaction. (c) The logical quantum circuit for implementing the *purely dissipative* map $e^{t\mathcal{L}}$ that sends the approximate ground state ρ_i and geometry $\mathbf{R}(s_i)$ to the next ground state along the reaction path ρ_{i+1} where circuit U_H denotes the block encoding of a chemical Hamiltonian which is used to implement the logical circuit described in Section H.

While our protocol transports a state along a reaction path, it should not be viewed as a dissipative analogue of adiabatic continuation. Adiabatic approaches rely on coherent evolution and require suppressing diabatic transitions globally along the path, leading to worst-case runtime bounds governed by small spectral gaps. In contrast, our method performs a sequence of local dissipative stabilization steps that repeatedly re-concentrate population into the instantaneous low-energy manifold. The role of the reaction path is therefore not to define a slow physical evolution, but to ensure geometric smoothness so that each cooling stage begins from a warm start with bounded excess energy. Algorithmic efficiency arises from mixing-time properties of the engineered Lindbladian rather than from adiabatic gap protection. In particular, path optimization is used here as a computational design principle: by selecting geometries that avoid abrupt projector rotations or strong bottlenecks, the continuation problem is converted from a coherent transport task into a sequence of locally contracting dissipative updates. This distinction places the present work conceptually closer to continuation methods with stabilization than to digital adiabatic simulation, even though both frameworks exploit smooth Hamiltonian deformations.

Tensor network methods and quantum algorithms for ground state preparation have now matured to the point at which we can obtain accurate ground states at equilibrium geometries [4, 5]. Our algorithm amplifies the utility of this capability to prepare ground states at reactants and products, given that the real difficulty in accurately

modeling quantum chemical systems is obtaining accurate TS ground states, and thereby accurate energetics, during bond breaking/bond forming. Our algorithm allows quantum computers to probe bond breaking/bond forming, which is the very essence of chemistry, thus opening up an entirely new class of chemical problems with provable quantum advantage. This work identifies a structured regime in which dissipative continuation yields polynomial overhead beyond equilibrium ground-state preparation [6].

Our protocol is designed for the common setting where high-quality states are available at equilibrium geometries but degrade near the TS. Instead of requiring a fresh, high-overlap guiding state at the hardest geometry, we assume a warm start at an easy geometry (e.g., reactant or product minimum) and transport it along the discretized reaction coordinate by repeatedly applying a dissipative cooling primitive at intermediate geometries. Operationally, each step combines (i) maintaining a consistent orbital gauge along the path (so that successive Hamiltonians are compared in a smooth frame) and (ii) applying an engineered open-system map that contracts toward the instantaneous low-energy sector. This shifts the state-preparation burden from “guessing” the TS ground state to “stabilizing” a transported warm start as correlations strengthen along the path.

This design targets the uneven computational profile of chemistry. The approach is most beneficial when (a) equilibrium regions admit reliable classical or hybrid preparation (e.g., tensor-network/DMRG-quality warm starts), (b) the TS window is strongly multi-reference so pointwise

overlaps can become extremely small, and (c) the path is sufficiently smooth that successive low-energy projectors rotate gradually, allowing modest cooling at each step to maintain high overlap. Conversely, if a globally good guiding state exists at all geometries, or if the path crosses an abrupt rearrangement with extremely small gaps and sharp wavefunction changes that violate the smoothness and rapid-mixing conditions, then pointwise methods or coherent transport may be preferable.

Quantum computers offer the potential to provide high-accuracy approximations to ground states even in these strongly-correlated regimes through algorithms such as quantum phase estimation (QPE) [7–15] and quantum imaginary time evolution (QITE) [16]. Yet, the performance of these approaches is constrained by the availability of a good initial guess, a state with nontrivial overlap with the target ground state [17–19]. Recent progress on engineered open-system (Lindbladian) protocols has also enabled thermal and ground state preparation for chemical Hamiltonians [20, 21]. In particular [20] provides detailed analysis on cooling sub-routines that we build on here by applying to transition state chemistry and modifying the family of filter functions used. These methods, too, require the provision of a “warm start,” an initial guess that has some guarantee to be close to the true ground state in order to avoid sub-optimal local minima in the energetic landscape [22]. Providing such an approximation is far from trivial, as the electronic-structure Hamiltonian is known to be QMA-complete and NP-Hard depending on the setting [23–25]. This worst-case hardness motivates the question of whether chemically structured instances admit defensible quantum speedups in practice [6], especially those with clear scientific or economic value.

Chemical accuracy (~ 1 kcal/mol ≈ 1.6 mHa) sets the bar for the performance—and thereby the quantum resources—required to determine ground-state energies along a reaction path. In chemical kinetics, the *rate constant* $k(T)$ is the temperature-dependent proportionality factor that relates reactant concentrations to the reaction rate; it provides a direct, quantitative link between microscopic energetics and macroscopic observables such as reaction timescales, selectivity, and temperature dependence. Because $k(T)$ is exponentially sensitive to the activation barrier, quantitative kinetics requires barrier heights at approximately chemical accuracy. In particular, within an Arrhenius or transition-state approximation,

$$k(T) \propto \exp\left(-\frac{\Delta E^\ddagger}{k_B T}\right), \quad (1)$$

where $\Delta E^\ddagger = E_{\text{TS}} - E_{\text{R}}$ is the activation barrier between the reactant minimum and the transition state. At room temperature, $k_B T \approx 0.6$ kcal/mol, so an error of 1 kcal/mol in ΔE^\ddagger changes the predicted rate by a factor of $\exp(1/0.6) \approx 5$. This motivates the usual “chemical accuracy” target: relative energies—especially barrier heights—should be accurate to ~ 1 kcal/mol ≈ 1.6 mHa.

The standard quantum algorithmic approach is to determine the reaction path classically using density functional theory (DFT) calculations, applying QPE to an ansatz state that can be efficiently described classically at a fixed geometry along the path. [26]. The success of this approach relies on an initial state with significant overlap with the true ground state; however, in strongly correlated regimes the overlap can be exponentially small in the number of system qubits, rendering QPE inefficient as a ground-state preparation routine on its own. This motivates end-to-end strategies that propagate a warm start along a reaction path, maintaining efficiency as the system enters the strongly correlated transition-state region separating reactants and products.

Very recently, Puig *et al.* [27] proposed a similar warm-start strategy that tracks a discretized Hamiltonian deformation along an arbitrary path through configuration space. The approach of Puig *et al.* [27] uses a variational ground-state preparation technique at each Hamiltonian along the discretized path, using each solution to initialize the next. The authors argue that this can improve trainability when the path avoids gap closings. Our work shares the same path-tracking intuition, but targets the transition-state bottleneck with an engineered dissipative cooling primitive designed to stabilize a transported warm start as correlations strengthen.

Relative to a single QPE application at the TS, the advantage regime is precisely the overlap-limited setting. In QPE used as a state-preparation primitive, the expected repetition overhead scales as $1/p_0$, where p_0 is the squared overlap of the input state with the TS ground state; if p_0 is exponentially small, this factor dominates even when Hamiltonian simulation is efficient. Dissipative evolution avoids this bottleneck by using a contractive open-system primitive to repeatedly re-concentrate weight into the instantaneous low-energy manifold as the system moves along the path, thereby maintaining a warm start without requiring a separate, high-overlap TS ansatz.

Our work complements recent progress on dissipative and hybrid strategies for chemical state preparation along reaction coordinates, including constructions that improve warm starts and enable controlled access to excited manifolds [28, 29]. In this emerging picture, equilibrium-quality classical (or hybrid) preparation supplies high-fidelity endpoints, while path-based dissipative evolution provides a principled mechanism to carry those warm starts through the transition-state bottleneck where classical guiding states are least reliable.

The remainder of the paper is organized as follows. In Section II, we prove the efficiency i.e., identify the regime in which our algorithm requires $O(\text{poly}(N_o))$ quantum resources, and show how to optimize the reaction path to ensure efficiency. In Section III we provide an implementation of our algorithm, we present a set of numerical models to validate the algorithm and provide evidence for the ubiquity of the ETH-like regime, and present resource estimates associated with running our algorithm on real-world chemical problems for fault-tolerant

quantum computers. In Section IV, we discuss how our algorithm fits into the ongoing pursuit of developing practical fault tolerant quantum algorithms for studying chemical reactions. In Sections B and F, we provide proofs of theorems introduced herein, in addition to the methodology behind our resource estimation for practical quantum circuit implementations of our algorithm in Sections H and I. Additionally, we establish our algorithm within the broader landscape of ground-state preparation methods through a detailed comparative analysis in Sections C and D.

II. DISSIPATIVE EVOLUTION

In this section, we present the *dissipative evolution*, and the conditions under which it may be used to prepare the ground state of a chemical Hamiltonian with a target geometry. The efficiency proof has two parts: a smoothness bound that controls how the ground state changes as the geometry is varied along the path, and a Markov-process bound that controls how many cooling steps are needed at each discretized geometry.

A. Definitions and Assumptions

We begin by introducing the key definitions we require to analyze the complexity of the dissipative evolution algorithm. Our analysis begins with the mathematical basis for the *smoothness* of the reaction path. Within the Born-Oppenheimer approximation, we study the electronic structure Hamiltonian $H_{\text{el}}(\mathbf{R})$ acting on the Hilbert space spanned by Slater determinants of N_e electrons in N_o spatial orbitals, with Full Configuration Interaction (FCI) dimension $D = \binom{2N_o}{N_e}$. A *reaction path* (or path-way) is a one-dimensional manifold of nuclear geometries $\mathbf{R} : [0, 1] \rightarrow \mathbb{R}^{3N_{\text{nuc}}}$ that connects reactant and product basins on the potential energy surface (PES), parameterized by a reaction coordinate s . We choose $s = 0$ and $s = 1$ to coincide with the optimized equilibrium geometries of the reactants and products, respectively. The transition-state geometry $\mathbf{R}_{\text{TS}} := \mathbf{R}(s^*)$ lies at the highest point along the minimum-energy pathway and corresponds to a first-order saddle point of the PES (Fig. 1b).

Definition 1 (Reaction path Hamiltonian). Let $\mathbf{R} : [0, 1] \rightarrow \mathbb{R}^{3N_{\text{nuc}}}$ be a reaction path and define $H(s) = H_{\text{el}}(\mathbf{R}(s))$. Let $\{|E_j(s)\rangle, E_j(s)\}_j$ denote the energy-ordered eigenstates and eigenvalues of $H(s)$, with unique ground state $|E_0(s)\rangle$, and spectral gap at s $\Delta(s) = E_1(s) - E_0(s) > 0$. We denote by Δ_{min} the minimum spectral gap over the reaction path.

Although the map $\mathbf{R} \mapsto H_{\text{el}}(\mathbf{R})$ is smooth in the nuclear coordinates, its second-quantized representation can exhibit apparent discontinuities if the underlying orbital gauges are chosen independently at each geometry. We therefore fix a consistent orbital gauge along the path by

a Procrustes alignment procedure described by Proposition 1 and impose smoothness conditions in that fixed gauge. We write the path Hamiltonian as a sum of M Hermitian fragments,

$$H(s) = \sum_{\ell=0}^{M-1} h_{\ell}(s), \quad (2)$$

where M scales as $O(N_o)$ for electronic structure Hamiltonian and N_o is the number of (spatial) orbitals in the system [30]. In this frame, we use a Lipschitz smoothness criteria:

Definition 2 (Lipschitz reaction path). A reaction path is said to be *Lipschitz smooth* if for all $\ell \in [M]$ and all $s, s' \in [0, 1]$, then

$$\|h_{\ell}(s) - h_{\ell}(s')\|_2 \leq L_h |s - s'|, \quad (3)$$

where $L_h > 0$ is the associated Lipschitz constant.

In particular, the smoothness condition enforces the following bound $\|H(s) - H(s')\|_2 \leq ML_h |s - s'|$. To relate this operator smoothness to the motion of the ground state along the path, we additionally assume the path is (piecewise) differentiable in the fixed orbital gauge, i.e., each fragment $h_{\ell}(s)$ is C^1 . Then

$$\|\partial_s H(s)\|_2 \leq \sum_{\ell=0}^{M-1} \|\partial_s h_{\ell}(s)\|_2. \quad (4)$$

To quantify the smoothness of a reaction path Hamiltonian, we introduce the Davis-Kahan constant:

Definition 3 (Davis-Kahan constant). Let $\{H(s)\}_s$ be a series of Hamiltonians on Lipschitz reaction path as in Definition 2. The associated geometric Davis-Kahan constant is defined as

$$C_{\text{DK}} := \int_0^1 \frac{\|\partial_s H(s)\|_2}{\Delta(s)} ds. \quad (5)$$

The Davis-Kahan constant C_{DK} informs the rate of variation of the ground-state projector $P_0(s) = |E_0(s)\rangle\langle E_0(s)|$ as a function of s . Consequently, if C_{DK} is small, the ground state does not rotate too rapidly along the path. Note that a coarse bound on C_{DK} is

$$\begin{aligned} C_{\text{DK}} &\leq \frac{1}{\Delta_{\text{min}}} \int_0^1 \sum_{\ell=0}^{M-1} \|\partial_s h_{\ell}(s)\|_2 ds \\ &\leq \frac{M}{\Delta_{\text{min}}} \max_{\ell \in [M]} \sup_{s \in [0, 1]} \|\partial_s h_{\ell}(s)\|_2. \end{aligned}$$

The Davis-Kahan constant C_{DK} is analogous to the ‘‘adiabatic condition’’ that appears in adiabatic ground state preparation [2, 31], where the ratio of the path derivative to the instantaneous ground state gap controls how rapidly the ground state can change with s .

To optimize reaction paths, we must define an appropriate notion of path smoothness, this is captured by the operator-Lipschitz constant.

Definition 4 (Operator-Lipschitz constant). Let $\mathbf{R} : [0, 1] \rightarrow \mathbb{R}^{3N}$ be a C^1 reaction path with Fréchet derivative $D_{\mathbf{R}}H_{\text{el}}(\mathbf{R}) : \mathbb{R}^{3N} \rightarrow \text{Herm}$. Define the operator-Lipschitz constant L_{max} as a scalar that bounds the operator norm of $D_{\mathbf{R}}H_{\text{el}}(\mathbf{R})$,

$$\sup_{\|v\|=1} \|D_{\mathbf{R}}H_{\text{el}}(\mathbf{R})[v]\|_2 \leq L_{\text{max}}.$$

Let ρ be a density operator. In the instantaneous energy eigenbasis $|E_i(s)\rangle_i$, it induces a population distribution

$$\mu(i) = \langle E_i(s) | \rho | E_i(s) \rangle.$$

Fix an energy-layer width $\Delta E_{\text{layer}} > 0$, and define the layer index of eigenstate j by

$$L(j) := \left\lceil \frac{E_j - E_0}{\Delta E_{\text{layer}}} \right\rceil, \quad (6)$$

which partitions the spectrum into layers of equal energy thickness, Fig. 5 shows a depiction of the layers for increasing sizes of active spaces. We say that μ is ΔE_{layer} -concentrated if there exist $L_\mu \in \mathbb{N}$ and $\eta \in (0, 1)$ such that

$$\Pr_{j \sim \mu}(L(j) > L_\mu) \leq \eta \quad (7)$$

With these definitions, the population dynamics induced by a dissipative primitive can be reduced to a classical Markov chain $(J_t)_{t \geq 0}$ on the eigenstate labels. Following [20, 32], the transition kernel is a row-stochastic matrix P mapping the pre-primitive distribution μ to the post-primitive distribution μ' , i.e., $\mu' = \mu P$. For a formal definition, see Section A. The matrix P can also be viewed as an edge-weighted directed graph (see Fig. 1a).

We assume the ground state corresponds to the target state 0, and define the hitting time of state 0 (ground state) by

$$\tau_0 = \inf\{t \in \mathbb{N} : J_t = 0\}. \quad (8)$$

This hitting time controls the number of dissipative steps required to reach the ground state up to a target failure probability ε .

Definition 5 (Dissipative Evolution Mixing time). Formally, for $0 < \varepsilon < 1$, the (warm-start) mixing time is

$$t_{\text{mix}}(\varepsilon, \mu) := \inf \left\{ t \in \mathbb{N}_0 : \Pr_{\mu}(\tau_0 > t) \leq \varepsilon \right\}, \quad (9)$$

Equivalently, t_{mix} is the smallest number of dissipative steps sufficient to reach the ground state with probability at least $1 - \varepsilon$ when initialized from the warm-start distribution μ induced by ρ . Therefore, once we can obtain a bound on $t_{\text{mix}}(\varepsilon, \mu)$ under the assumption above, we can provide a bound on the total number of dissipative steps required by the algorithm. Combined with the cost of implementing each step, this yields an overall runtime bound, which we will show in Section II B is polynomial in the problem size (i.e. N_o). In the next section we compare our approach to popular alternatives and provide logical resource estimates for implementing our dissipative state-preparation primitive.

B. Efficient Ground State Preparation at Transition Geometries

In this section, we demonstrate how dissipative evolution algorithm allows for efficient quantum state preparation, using open quantum system simulation as an algorithmic primitive [20, 21, 33]. In a chemical reaction, the ground states of Hamiltonians at the reactant or product geometries are typically well described by classical means. At the transition-state geometry, however, $H(s^*)$ is typically too strongly interacting for classical methods to provide any guarantees. Thus, our goal is to design a quantum algorithm that prepares a state ρ such that

$$|\text{tr}(H(s^*)\rho) - E_0(s^*)| \leq \epsilon_E$$

where $E_0(s^*)$ is the ground state energy of $H(s^*)$.

Theorem 1 (Reaction-path ground-state preparation; informal). *Given a Lipschitz smooth reaction path Hamiltonian $H_{\text{el}}(\mathbf{R}(s))$ with N_o spatial orbitals and a warm start at $s = 0$, the ground state at any target geometry $s \in (0, 1]$ can be prepared with an energy error $\leq \epsilon_E$ with complexity*

$$\tilde{O} \left(\frac{C_{DK}^2 N_o}{\epsilon_E} \right) \leq \tilde{O} \left(\frac{\|H\|}{\Delta_{\text{min}}^3} \cdot \frac{1}{\epsilon_E} \cdot N_o^3 \right).$$

Theorem 1 is reached by combining the scaling in terms of the cooling primitive (presented in Section B as Theorem 3), with the circuit complexity cost of implementing the cooling primitive from Theorem 2. The key structural feature we exploit is that along a physically meaningful reaction coordinate the Hamiltonian varies smoothly and the ground-state projector does not rotate arbitrarily fast.

At the algorithmic level, we approximate the potential energy surface using classical methods and then optimize a reaction pathway that meets the smoothness condition. We then proceed by continuation along the reaction path. We discretize $s \in [0, 1]$ into a sequence of geometries and, at each step, apply a dissipative cooling primitive that amplifies the ground-state population at the new geometry, using the ground-state approximation from the previous step as input (see Fig. 1b). The overall complexity is governed primarily by how rapidly the ground-state subspace varies with s and by the target energy accuracy ϵ_E .

Concretely, we first identify a chemical system of interest that comes equipped with one or more reaction pathways that smoothly connect points along the pathway(s). These reaction pathways are typically determined using a transition-state search algorithm such as nudged elastic band, synchronous transit-guided quasi-Newton, or constrained optimization [34]. Typically chemist's look for the minimum energy pathway (MEP), however, we have the freedom to select *any* smooth pathway so long as it contains the physical transition state geometry. The opens up an entire *design space* for optimizing the runtime of our algorithm for a given chemical reaction of

interest. We discuss the reaction pathway optimization via the calculus of variations in Section IID.

Once a reaction path is selected and optimized, we discretize the path in to N_H points $\{s_i\}_{i=0}^{N_H-1}$ where $s_0 = 0$ is the reactant/product equilibrium chemical geometry and $s_{N_H-1} = s^*$ is the target transition state chemical geometry. At each point along the reaction, we classically build electronic structure Hamiltonians $H_{\text{el}}(\mathbf{R}(s_i))$ then use one of many classical post-Hartree Fock methods, namely the density matrix renormalization group (DMRG), to generate *effective warm start* at the initial geometry s_0 .

Geometrically, the instantaneous ground state $|E_0(s)\rangle$ traces out a smooth curve on the state manifold as s varies from the reactants toward the transition state. For a Lipschitz-smooth reaction path, adjacent Hamiltonians differ only slightly, so the associated low-energy projectors do not rotate abruptly between s_i and s_{i+1} . As a result, the ground state at s_i has nontrivial overlap with the low-energy subspace at s_{i+1} and therefore serves as an effective warm start. Consequently, the dissipative dynamics at each step need only remove a small residual excited-state population rather than cool from a generic high-energy state. A complete description of our algorithm is provided in Section K.

Comparison to other Ground State Preparation Techniques

Ground-state preparation at transition-state geometries is known to be a computationally challenging problem for which a myriad of quantum algorithms have been designed. Notable examples include quantum phase estimation [7] (QPE), digital adiabatic simulation [2] (DAS), phase randomization [31] (PR) and dynamic cooling [35] (DC). Table I presents a comparison between the asymptotic runtime of these algorithms with dissipative evolution in terms of their shared parameters: the number of orbitals N_o , the maximum Hamiltonian norm along the reaction path $\|H\| := \max_s \|H(s)\|$, and the minimum spectral gap $\Delta_{\min} := \min_s \Delta(s)$. In terms of these parameters, dissipative evolution, using a Lindbladian-type cooling primitive has a gate complexity of

$$n_G^{\text{diss}} = \tilde{O}\left(\frac{\|H\|}{\Delta_{\min}^3} \cdot \frac{1}{\epsilon_E} \cdot N_o^3\right). \quad (10)$$

We compare this asymptotic scaling to each of the other ground state preparation algorithms below. A more detailed discussion of the comparisons made here between these ground state preparation algorithms can be found in Section C and Section D.

Quantum Phase Estimation QPE projects an input state onto approximate energy eigenstates of a Hamiltonian by coherently correlating each eigencomponent with its eigenphase and collapsing onto the measured outcome. To present a meaningful comparison to QPE, we present the algorithmic cost for applying QPE directly at the target transition-state geometry to prepare the ground

Algorithm	Gate complexity
QPE [7]	$\tilde{O}\left(\frac{\ H\ }{\Delta_{\min}} \cdot \frac{1}{\epsilon_E} \cdot \frac{1}{p_0} \cdot \text{poly}(N_o)\right)$
DAS [2]	$\tilde{O}\left(\frac{\ H\ ^3}{\Delta_{\min}^3} \cdot \frac{1}{\epsilon_E} \cdot \text{poly}(N_o)\right)$
PR [31]	$\tilde{O}\left(\frac{\ H\ }{\Delta_{\min}} \cdot \frac{1}{\epsilon_E} \cdot \frac{1}{1-p_{\text{succ}}} \cdot \text{poly}(N_o)\right)$
DC [35]	$\tilde{O}\left(\frac{\ H\ }{\Delta_{\min}} \cdot \frac{1}{\epsilon_E} \cdot \text{poly}(N_o)\right)$
This work	$\tilde{O}\left(\frac{\ H\ }{\Delta_{\min}^3} \cdot \frac{1}{\epsilon_E} \cdot N_o^3\right)$

TABLE I. Gate complexity comparison (suppressing polylogarithmic factors via \tilde{O}). Here $\|H\|$ denotes that maximum operator norm over the reaction path, and Δ_{\min} is the minimum spectral gap along the path. The target energy precision is ϵ_E . N_o is a problem-size parameter (e.g., number of spatial/spin orbitals), and $\text{poly}(N_o)$ denotes method-dependent polynomial overheads (such as basis changes, state preparation subroutines, or term-selection costs). For QPE, $p_0 := |\langle E_0(s^*)|\phi\rangle|^2$ is the initial squared overlap of the prepared state $|\phi\rangle$ with the target ground state $|E_0(s^*)\rangle$ at the hardest point s^* , giving the expected $1/p_0$ repetition overhead. For PR, p_{succ} is the per-attempt success probability of the projective/randomization step, yielding repetition overhead $1/(1-p_{\text{succ}})$. For our method, we use the estimate $C_{\text{DK}} = O(N_o/\Delta_{\min})$, which is absorbed into the displayed scaling.

state. Typically $\Delta_{\min} \sim \Delta(s^*)$, therefore we may use Δ_{\min} to directly compare QPE with dissipative evolution. The practical limitation of QPE, however, is the need for an efficiently preparable, semi-classical guiding state $|\phi\rangle$ [17–19]. The fidelity of the guiding state with the true ground state,

$$p_0 := |\langle E_0(s^*)|\phi\rangle|^2 \in (0, 1], \quad (11)$$

informs the gate complexity, therefore the comparable QPE gate complexity is

$$n_G^{\text{QPE}} = \tilde{O}\left(\frac{\|H\|}{\Delta_{\min}} \cdot \frac{1}{\epsilon_E} \cdot \frac{1}{p_0} \cdot \text{poly}(N_o)\right). \quad (12)$$

Dissipative evolution is intended for settings where constructing the guiding state $|\phi\rangle$ with large overlap with the ground-state is unavailable or unreliable. This situation commonly arises in strongly multi-reference regions [36–39]. In these regimes the ground state is no longer well described by a single determinant or low-entanglement ansatz: several near-degenerate configurations contribute with comparable weight and natural-orbital occupations deviate significantly from idempotency as the nuclear geometry approaches a symmetry-enhanced or bond-rearrangement configuration. As a result, even chemically motivated ansätze prepared at TS geometries may have extremely poor overlap, making it challenging in practice to guarantee provably non-negligible overlap without extensive active-space optimization that may be exponentially expensive. In such cases, QPE’s cost may be dominated by the $1/p_0$ factor in Eq. (12).

Instead, we assume access to a warm start at an easy geometry (Hamiltonian) and transport it along a smooth reaction coordinate by repeatedly applying a cooling primitive at intermediate geometries. This shifts the state-preparation requirement from finding a good guiding state $|\phi\rangle$ for $H(s^*)$ to starting from a good state and following the path. In practice, an approach combining our dissipative evolution approach with QPE could be employed to boost the overlap with $|E_0(s^*)\rangle$ at the target geometry before applying QPE for high-precision energy estimation.

Digital Adiabatic Simulation DAS prepares the ground state by varying a discretized Hamiltonian slowly enough to ensure that the state of system remains within the instantaneous low-energy subspace throughout the evolution. To make a comparison to DAS, we consider the algorithmic complexity of using DAS to coherently evolve the state $|E_0(s_0)\rangle$ to $|E_0(s^*)\rangle$ by digital adiabatic simulation from moving along the same reaction path from $H(s_i)$ to $H(s_{i+1})$ until we reach $|E_0(s^*)\rangle$. Using the recent improvements on large-timestep DAS [2], we can write the complexity of the improved algorithm as

$$n_G^{\text{DAS}} = \tilde{O}\left(\frac{\|H\|^3}{\Delta_{\min}^5} \cdot \frac{1}{\epsilon_E} \cdot \text{poly}(N_o)\right). \quad (13)$$

The asymptotic runtime complexity of dissipative evolution is quadratically better than DAS in terms of the Hamiltonian norm over the minimum gap $\|H\|/\Delta_{\min}$. A key distinction between DAS and dissipative evolution is how errors scale and accumulate along the path. Digital adiabatic simulation is a coherent transport method: to keep the state within the instantaneous low-energy subspace, the schedule must suppress diabatic transitions, and existing worst-case bounds therefore exhibit a strong dependence on the minimum spectral gap along the path (e.g., the Δ_{\min}^{-5} dependence in [2]). By contrast, dissipative evolution implements a *contractive* channel that relaxes toward the instantaneous low-temperature state (and, in the zero-temperature limit, toward the ground-state manifold). In the regime we target—where a warm start is available at an easy geometry and the path is sufficiently smooth—state-preparation reduces to repeatedly re-cooling at intermediate geometries. Under the uniform downward drift / mixing assumptions used in our analysis, the number of cooling steps is controlled by a mixing-time parameter (captured in our constant C_{DK} and related hitting-time bounds) rather than by an adiabatic gap condition. Accordingly, our advantage over DAS should be understood as replacing worst-case adiabatic gap dependence with a mixing-time dependence that can be substantially milder in ETH-like, locally thermalizing regions; we do not claim an unconditional improvement in $\|H\|/\Delta_{\min}$ in the worst case.

Phase Randomization In PR, at each point $H(s)$, we apply the instantaneous Hamiltonian for a *random* evolution time. Averaging over random times induces dephasing in the eigenbasis of $H(s_j)$, which approximates a projective measurement onto the instantaneous ground state (a quantum-Zeno-type stabilization), thereby al-

lowing ground-state transport along the discretized path. Under the standard Hamiltonian-simulation cost model (evolution for time t costs $\tilde{O}(t\|H\|\text{poly}(N_o))$ gates), the phase-randomization method has total gate complexity,

$$n_G^{\text{PR}} = \tilde{O}\left(\frac{\|H\|}{\Delta_{\min}^3(1-p_{\text{succ}})} \cdot \frac{1}{\epsilon_E} \cdot \text{poly}(N_o)\right), \quad (14)$$

where p_{succ} is the target probability of success of the PR algorithm in preparing the correct state. The complexity of the dissipative evolution matches that of the PR algorithm in parameters $\|H\|$ and Δ_{\min} . The complexities differ in terms of the degree of the polynomial scaling with N_o . Moreover, the PR algorithm is *probabilistic* and returns the correct ground state with probability p_{succ} . In contrast, Dissipative Evolution deterministically returns a state that has an energy within $\epsilon_E > 0$ of the ground state.

Dynamic Cooling DC achieves ground-state energy reduction via a purely unitary, closed-system procedure rather than explicit coupling to an external bath or ancilla bath degrees of freedom. In this approach, one alternates between a spectral transformation of the Hamiltonian implemented using quantum signal processing and evolution under a weak perturbation chosen to induce transitions that preferentially move populations toward lower energies in order to prepare the ground-state energy to within a target resolution ϵ_E . In this case, the asymptotic complexity of using dynamic cooling for transporting a ground state along a reaction path is

$$n_G^{\text{DC}} = \tilde{O}\left(\frac{\|H\|}{\Delta_{\min}^3} \cdot \frac{1}{\epsilon_E} \cdot \text{poly}(N_o)\right). \quad (15)$$

Much like PR, DC has a similar scaling in terms of $\|H\|$ and Δ_{\min} to dissipative evolution, with the key difference being in the order of the polynomial scaling on the number of orbitals. The overall computational cost of transporting a ground state along a reaction path using DC as the cooling subroutine scales less favorably with respect to the system size; specifically, the runtime for the algorithm is bounded from below by $\Omega(N_o^{7/2})$, which neglects the polynomial overhead from calling a Hamiltonian simulation subroutine that implements $e^{\pm iH}$, which is called $\tilde{O}(N_o^{3/2})$ times at each point along the reaction path.

C. Proof Outline and Complexity Analysis

The proof of Theorem 1 rests on three lemmas. First, Lemma 1 shows that if we discretize the reaction coordinate finely enough, then successive ground states along the grid have non-trivial overlap. Equivalently, the cumulative rotation of the ground state along the path determines how many grid points N_H are needed. Thus, the smoothness of the reaction path implies that a polynomially small number of reaction geometries are required.

Next, Lemma 2 gives a tail bound on the ground-state hitting time τ_0 for the Markov chain with kernel P , assuming the ETH-motivated uniform downward drift condition (see Section B 2 for a formal definition). The uniform downward drift condition reflects the ETH expectation that a local jump operator couples a typical excited eigenstate to a dense set of lower-energy eigenstates with broadly distributed matrix elements. In such settings, convergence does not rely on the absence of local minima but rather on local smoothness and conditioning that induce a monotonic descent direction [40]. Although the number of accessible lower-energy states grows rapidly with energy, the typical matrix elements to each state decrease accordingly, so that the summed probability of downward energy transitions remains essentially constant.

Lemma 3 then shows that for a sufficiently warm start and Lipschitz-smooth path, the required number of cooling steps scales linearly with N_o . Combined with the discretization bound Lemma 1 and the implementation scaling from Section III, these results yield the overall runtime scaling in Eq. (10).

Lemma 1 (Bounding Successive Ground-State Overlap; informal). *Let $H(s)$ be a reaction path Hamiltonian with a non-degenerate ground state $|E_0(s)\rangle$. Then, for any $0 \leq s_a < s_b \leq 1$,*

$$1 - |\langle E_0(s_a) | E_0(s_b) \rangle|^2 \leq \left(\int_{s_a}^{s_b} \frac{\|\partial_s H(s)\|_2}{\Delta(s)} ds \right)^2. \quad (16)$$

Lemma 1 formalizes the idea that the ground state cannot rotate arbitrarily fast along the reaction coordinates. In particular, the quantity $\|\partial_s H(s)\|_2 / \Delta(s)$ controls the local rate at which the ground-state can rotate. To see where Eq. (16) comes from, fix a smooth phase choice (parallel transport) so that $\langle E_0(s) | \partial_s E_0(s) \rangle = 0$. Differentiate the eigenvalue equation $H(s) |E_0(s)\rangle = E_0(s) |E_0(s)\rangle$ with respect to s and project onto the excited subspace. Using the gap $\Delta(s) = E_1(s) - E_0(s)$ gives the standard bound

$$\|\partial_s |E_0(s)\rangle\| \leq \frac{\|\partial_s H(s)\|_2}{\Delta(s)}. \quad (17)$$

Geometrically, the Fubini–Study distance between the eigenstates at s_a and s_b is at most the path length traced by $|E_0(s)\rangle$ on $[s_a, s_b]$. Hence,

$$1 - |\langle E_0(s_a) | E_0(s_b) \rangle|^2 \leq \left(\int_{s_a}^{s_b} \|\partial_s |E_0(s)\rangle\| ds \right)^2. \quad (18)$$

Combining Eq. (18) with Eq. (17) yields Eq. (16). In Section B 1, we provide a proof to a more general statement, of which Eq. (16) is a special case.

Lemma 1 can then be used to choose a discretization of the reaction coordinate. Let $\{s_i\}_{i=0}^{N_H-1}$ be an ordered grid with $s_0 = 0$ and $s_{N_H-1} = s^*$. If this grid is fine enough that the integral in Eq. (16) over each interval $[s_{i-1}, s_i]$ is $O(\sqrt{\epsilon_E})$, then successive ground states have non-trivial overlap. Thus we see that the number of grid points is $N_H = \tilde{O}(C_{DK}^2 / \epsilon_E)$ (see Section B 2 for derivation).

Once a grid is fixed [41], it remains to bound the number of cooling steps required at each point s_i . Let ρ denote an initial input state with an eigenbasis distribution μ . One application of the cooling primitive at s_i updates populations according to a Markov kernel P_i , in the sense that the population distribution is updated to

$$\mu(k) \leftarrow \sum_{j=0}^{D-1} \mu(j) (P_i)_{j \rightarrow k},$$

where we view μ as a row vector. The number of P_i applications required at configuration s_i is determined by the hitting time τ_0 defined in Eq. (8), equivalently the warm-start mixing time $t_{\text{mix}}(\epsilon, \mu)$ in Eq. (9). To bound this cost, we need an assumption on the cooling kernel P_i that prevents the population from getting stuck in the excited states.

In the transition-state regime—where the spectral structure is most crowded and naive cooling can stall—we assume that the row-normalized transition kernel P_i satisfies a *uniform downward drift* condition. Concretely, fix a layer decrement $\Delta E_{\text{layer}} > 0$ and define, for each eigenstate index j in the relevant microcanonical window, the “successful downhill” set

$$S_j := \{k : E_k \leq E_j - \Delta E_{\text{layer}}\}.$$

The drift condition asserts the existence of a constant $p_{\text{min}} > 0$ such that, uniformly over the indices j in this window,

$$\sum_{k \in S_j} P_{j \rightarrow k} \geq p_{\text{min}}. \quad (19)$$

Equivalently, conditioned on the current eigenstate label j , each cooling step has probability at least p_{min} to decrease the energy by $\geq \Delta E_{\text{layer}}$; this rules out exponentially rare “useful” downhill moves (strong bottlenecks) within the window.

At first glance, Eq. (19) seems like a very strong condition, since it is a *uniform* (worst-case-over- j) lower bound rather than a typical-case statement. Two features of our setting make it plausible and, importantly, sufficient for our analysis. First, we do not invoke Eq. (19) from an arbitrary initialization: the previous lemma provides a warm start at step i with state mass already concentrated in the low-energy sector relevant to the subsequent cooling stage. Thus the drift assumption is only required *locally*—throughout the narrow energy window actually visited during the transition-state portion of the path—rather than globally across the full spectrum. Second, in over-parameterized optimization and related dynamics, a provably close warm start often places the iterate in a regime where the effective dynamics becomes well-conditioned and admits monotone progress guarantees; see [22, 40, 42] and references therein for a full discussion of how closeness to a target region upgrades qualitative mixing/escape behavior into quantitative, uniform progress bounds. The downward-drift assumption

mirrors the warm-start gradient-descent regime of neural tangent kernel theory, where linearized dynamics induce a contractive flow toward lower loss without requiring the absence of local minima [22, 40].

Lemma 2 (ETH-motivated rapid cooling bound; informal). *Consider a Markov Chain $(J_t)_{t \geq 0}$ with associated kernel P and initial law $\mu(j) := \Pr(J_0 = j)$ that is concentrated in low energy layers for a fixed layer width $\Delta E_{\text{layer}} > 0$. If P satisfies the ETH-motivated uniform downward drift condition, Eq. (19), then for any $0 < \varepsilon < 1$, we have the following condition on the hitting time*

$$\Pr(\tau_0 > 2L_\mu + 8 \ln(1/\varepsilon)) \leq \eta + \varepsilon, \quad (20)$$

where $L_\mu \in \mathbb{N}$ and, with probability at least $1 - \eta - \varepsilon$, the hitting time is bounded from above as

$$\tau_0 \leq 2L_\mu + 8 \ln \frac{1}{\varepsilon}. \quad (21)$$

At a fixed grid point s_i , we apply Lemma 2 to the kernel $P = P_i$ governing one application of the cooling stage at s_i . In this setting, the warm-start mixing time $t_{\text{mix}}(\varepsilon, \mu)$ in Eq. (9) is the number of kernel applications required to make $\Pr_\mu(\tau_0 > t) \leq \varepsilon$. Lemma 2 bounds this cost by a term linear in the warm-start layer cutoff L_μ plus a term logarithmic in ε^{-1} . To connect L_μ to the chemistry along the path, we use the fact that a warm start at s_i comes from the previous point s_{i-1} . If the reaction path is Lipschitz smooth, then one can show that

$$\langle E_0(s_{i-1}) | H(s_i) | E_0(s_{i-1}) \rangle - E_0(s_i) \leq c_E N_o$$

for a constant $c_E > 0$. This bound shows that the warm start has only $O(N_o)$ excess energy with respect to $H(s_i)$. In particular, by Markov's inequality, for any $\eta \in (0, 1)$,

$$\Pr_\mu \left(E_{J_0}(s_i) - E_0(s_i) > \frac{c_E N_o}{\eta} \right) \leq \eta.$$

With the layer partition in Eq. (6), where the layer index grows proportionally with energy above the ground state, this implies that μ is concentrated in the first $L_\mu = O(N_o)$ layers (up to probability η), which matches the warm-start condition in Lemma 2. The next lemma summarizes the resulting linear cooling-time bound.

Lemma 3 (Linear Cooling Time; informal). *Adopt the setting of Lemma 2. Suppose the warm start is concentrated over an extensive energy window above the ground state, i.e., there exists $c_E > 0$ such that*

$$\Pr_\mu(E_{J_0} - E_0 \leq c_E N_o) \geq 1 - \eta,$$

then for any $0 < \varepsilon < 1$, the cooling time required at each fixed s_i is

$$t = O \left(N_o + \ln \frac{1}{\varepsilon} \right).$$

Combining Lemma 1, which sets the required grid size, with Lemma 3, we obtain an upper bound on the total number of cooling steps required along the path:

$$\sum_{i=1}^{N_H} t_i = \tilde{O} \left(\frac{C_{\text{DK}}^2 N_o}{\varepsilon_E} \right),$$

where t_i denotes the number of kernel applications used at grid point s_i . In Section III, we provide a concrete quantum procedure that implements a cooling step realizing such a Markov kernel, together with the corresponding quantum circuit cost. Combining that implementation cost with the step count above yields the overall gate complexity cost, Eq. (10).

D. Reaction Path Optimization

In quantum chemistry, the term reaction path most commonly refers to a minimum-energy path (MEP) on the potential-energy surface, typically computed by standard path-finding routines such as the nudged elastic band (NEB) method [44–47]. In contrast, our algorithm does not require the path to be an MEP; we are free to prescribe any continuous path connecting the chosen endpoint geometries. This freedom allows us to optimize the transport path itself, i.e., the curve along which we carry the ground state via dissipative evolution, rather than accepting the MEP by default. The quality of a candidate path is captured by the Davis-Kahan constant C_{DK} , which controls the stability of the ground-state subspace under motion along the path and therefore directly sets the runtime of our algorithm. In order to optimize reaction paths for efficient dissipative evolution, we make use of the Operator-Lipschitz constant, that allows us to utilize the calculus of variations.

Lemma 4 (Chain-rule bound for the Davis-Kahan constant C_{DK} ; informal). *Assume $H_{\text{el}}(\mathbf{R})$ is Fréchet differentiable in \mathbf{R} along the image of the path, with operator-Lipschitz constant L_{max} . Then,*

$$C_{\text{DK}} \leq \frac{L_{\text{max}}}{\Delta_{\text{min}}} \int_0^1 \|\mathbf{R}'(s)\| ds. \quad (22)$$

Proof of Lemma 4 can be found in Section J. It follows that we can minimize C_{DK} by minimizing the length of the reaction path $\int_0^1 \|\mathbf{R}'(s)\| ds$. Lemma 4 motivates a smoothness-regularized reaction path optimization functional,

$$\begin{aligned} J(\mathbf{R}) := & \lambda_{\text{len}} \int_0^1 \|\mathbf{R}'(s)\| ds \\ & + \lambda_{\text{curv}} \int_0^1 \|\mathbf{R}''(s)\|^2 ds \\ & + \lambda_{\text{CI}} \int_0^1 \Phi_{\text{CI}}(\mathbf{R}(s)) ds, \end{aligned} \quad (23)$$

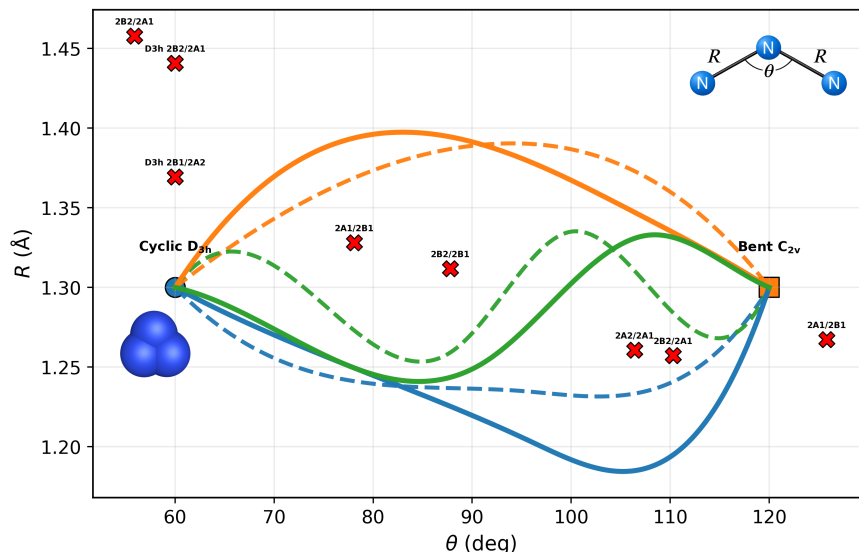


FIG. 2. Reaction-path optimization for N_3 in the (θ, R) internal-coordinate plane, demonstrating that our dissipative ground-state transport need not follow a minimum-energy path. Dashed curves show initial guess paths and solid curves show the optimized trajectories obtained by minimizing the path functional $J(\mathbf{R})$, which trades off geometric length, smoothness, and avoidance of conical-intersection (CI) neighborhoods. All paths connect the cyclic D_{3h} endpoint ($\theta \approx 60^\circ$, $R \approx 1.30$ Å) to the bent C_{2v} endpoint ($\theta \approx 120^\circ$, $R \approx 1.30$ Å). Red \times markers indicate surface-crossing / CI-type structures reported by Kerkinis *et al.* [43], which the optimized paths detour around to improve clearance from small-gap regions.

where Φ_{CI} is a smooth penalty that is large near a conical intersection (CI) and small away from it. Scalar values $\lambda_{len}, \lambda_{curv}, \lambda_{CI} > 0$ control the importance of reaction path length, curvature and avoidance of conical intersections, respectively. This approach allows us to control how rapidly the ground state changes along the selected reaction path while avoiding chemical geometries for which the spectral gap closes.

The length term is the leading-order control knob for C_{DK} through Corollary 1. The curvature term suppresses kinks and high-frequency parameterization artifacts, which in practice prevents localized spikes in $\|\mathbf{R}'(s)\|$ on the discrete mesh and stabilizes the minimization. The CP term enforces the intended homotopy class by repelling the curve away from the CP neighborhood, which is the regime where $\Delta(s)$ is expected to be smallest.

The N_3 molecule provides a concrete example where this reaction-path freedom matters. As shown by the high-level multireference study of Kerkinis *et al.* [43], the low-lying doublet manifold of N_3 contains many surface crossings and conical-intersection-type features as the NNN angle bends from the linear region toward cyclic geometries. This implies that a naive path (e.g., a minimum-energy path or a simple linear interpolation in internal coordinates) can easily encounter geometries where the electronic gap to a nearby excited state becomes small, precisely the regime that worsens adiabatic sensitivity and inflates the Davis–Kahan constant [43].

Operationally, we use the catalog of crossing structures and the qualitative location of intersection regions re-

ported for N_3 as targets to avoid during optimization. This yields a simple, reproducible workflow: compute or import a coarse map of “problematic” regions (small-gap or intersection neighborhoods), set λ_{CI} to enforce clearance from those regions, and tune $\lambda_{len}, \lambda_{curv}$ to maintain a short, smooth path.

In Fig. 2, we visualize the effect of optimizing the path functional $J(\mathbf{R})$ on N_3 . All three candidate paths connect the cyclic D_{3h} region ($\theta \approx 60^\circ$, $R \approx 1.30$ Å) to the bent C_{2v} region ($\theta \approx 120^\circ$, $R \approx 1.30$ Å), but the optimized trajectories (solid curves) systematically deform away from the intersection “hot spots.” Compared to their initial guesses (dashed curves), the optimized paths remain smooth and avoid sharp turns while making deliberate detours that increase clearance from the labeled crossing regions (notably the cluster near $\theta \sim 106$ – 112° and the interior crossings around $\theta \sim 80$ – 90°). This behavior is consistent with the intended role of the CI penalty term in $J(\mathbf{R})$, trading a modest increase in geometric distance for a more favorable gap profile along the route, thereby reducing adiabatic sensitivity (and hence C_{DK}) for subsequent ground-state transport.

III. IMPLEMENTATION AND RESOURCE ANALYSIS

In this section, we present a practical quantum-circuit that implements the cooling primitive from the dissipative evolution algorithm. We begin by analyzing the complexity associated with a single application of the

cooling primitive for a Hamiltonian at a fixed point along the reaction pathway $H(s_i)$. We then show a numerical demonstration of dissipative evolution looking at a chemical reaction in H_4 , for increasing applications of the cooling primitive, providing some evidence that the algorithm is effective (in terms of preparing a state with high overlap with the ground state), even for a low number of applications or the cooling primitive. Finally, we perform a cost analysis of the full algorithm, and present the gate complexity for a number of chemical systems of interest.

A standard mathematical starting point for *engineering* Lindbladian dynamics that drive a system into low-energy states is the Davies weak-coupling construction [48, 49]. In this framework one obtains a GKLS generator whose stationary state is the Gibbs state of the target Hamiltonian H . Modern dissipative ground-state preparation generalizes this approach to tailor jump operators such that the resulting Lindbladian has the ground state as its steady state. A particularly efficient method for doing so was introduced in Ref. [20] which uses *filtered* jump operators to construct such a Lindbladian.

Formally, we define the purely dissipative Lindbladian

$$\mathcal{L}[\cdot] = \sum_{a \in \mathcal{A}} K_a \cdot K_a^\dagger - \frac{1}{2} \{K_a^\dagger K_a, \cdot\}, \quad (24)$$

over a finite set of unfiltered jump operators $a \in \mathcal{A}$. In the chemical setting, there are several choices for jump operators that lead to efficient mixing [29], e.g., $\mathcal{A} = \{a_i^\dagger a_j\}_{i,j=1}^{N_o}$, where a_i^\dagger (a_j) are the second quantized fermion creation (annihilation) operators.

Once a suitable set of jump operators is selected, we obtain the filtered jump operators K_a by integrating out the Bohr frequencies ($\omega \in \{E_i - E_j : E_i, E_j \in \text{Spec}(H)\}$) that correspond to heating the system, leaving only cooling transitions.

Definition 6. For each *unfiltered* jump operator $A_a \in \mathcal{A}$, define the corresponding filtered jump operator K_a as

$$K_a := \int_{\mathbb{R}} f(t) e^{iHt} A_a e^{-iHt} dt, \quad (25)$$

where the associated $f(t)$ is the time-domain kernel of a filter function $\hat{f}(\omega)$ that filters out positive Bohr frequencies $\hat{f}(\omega) = 0, \forall \omega > 0$.

In Definition 6, the filtered jump operator K_a is written as a continuous superposition of Heisenberg-evolved operators $e^{iHt} A_a e^{-iHt}$, weighted by a kernel $f(t)$. In practice, however, this integral must be *truncated* to a finite time window and *discretized* to a finite set of times:

$$K_a \approx \sum_{m=-M}^M c_m e^{iHt_m} A_a e^{-iHt_m}, \quad t_m = m\Delta t, \quad (26)$$

where the coefficients c_m arise from the choice of the filter function and the associated numerical integration scheme, e.g., quadrature. The largest queried evolution

time $T := M\Delta t$ controls how sharply the frequency-domain filter $\hat{f}(\omega)$ can approximate the ideal projector onto negative Bohr frequencies: increasing T narrows the effective transition band of the filter and reduces residual “heating” leakage, while smaller T yields a broader filter and larger leakage. Motivated by this tradeoff, we define the *time support* $S(\varepsilon_{\text{leak}})$ as the maximum real time magnitude that must be queried by the (truncated and discretized) implementation in order to guarantee the target leakage level $\varepsilon_{\text{leak}}$. Operationally, when sampling on a uniform grid, the number of distinct real-time evolution primitives $e^{iHt}(\cdot)e^{-iHt}$ required is proportional to the number of grid points in $[-S(\varepsilon_{\text{leak}}), S(\varepsilon_{\text{leak}})]$, i.e. $\#\text{calls} = \Theta(S(\varepsilon_{\text{leak}})/\Delta t)$.

A. Time support scaling

Theorem 2 identifies and compares two classes of filter functions that each carry their own distinct asymptotic scaling. In both constructions, the filtered jump operator is realized by a time-domain representation (an integral, approximated by a finite sum) in which copies of the bare jump operator are conjugated by real-time evolution under H and weighted by the chosen filter kernel. The decisive implementation parameter is therefore the kernel’s *time support* $S(\varepsilon_{\text{leak}})$, i.e., the effective time window over which the kernel has non-negligible weight. This window determines the largest evolution time that must be synthesized and, after choosing a discretization step, the number of distinct time samples appearing in the approximation of $e^{\tau\mathcal{L}}$ for a small time step $\tau > 0$ [20].

Theorem 2 (Time support scaling for Gevrey vs. periodic square-wave filters; informal). *Let H be a Hamiltonian with nondegenerate ground state $|E_0\rangle$, spectral gap $\Delta > 0$, and let A be a bounded jump operator with $\|A\| \leq 1$. For any target leakage $0 < \varepsilon_{\text{leak}} < 1$ there exist two families of filtered jump operators $K_{\varepsilon_{\text{leak}}}^G$ and $K_{\varepsilon_{\text{leak}}}^{\text{SW}}$ with the following time-support:*

1. *There exists a Gevrey-class filter with time-domain kernel $f_{\varepsilon_{\text{leak}}}^G(t)$ essentially supported on an interval of length*

$$S_G(\varepsilon_{\text{leak}}) = O\left(\frac{\|H\|}{\Delta} [\log(1/\varepsilon_{\text{leak}})]^\alpha\right), \quad (27)$$

for some $\alpha > 1$ depending only on the Gevrey class [20].

2. *There exists a truncated periodic square-wave filter with discrete-time kernel $f_{\varepsilon_{\text{leak}}}^{\text{SW}}(t)$ supported on*

$$S_{\text{SW}}(\varepsilon_{\text{leak}}) = O\left(\frac{\|H\|}{\Delta} \frac{1}{\varepsilon_{\text{leak}}}\right), \quad (28)$$

up to bounded oscillatory factors in the leakage.

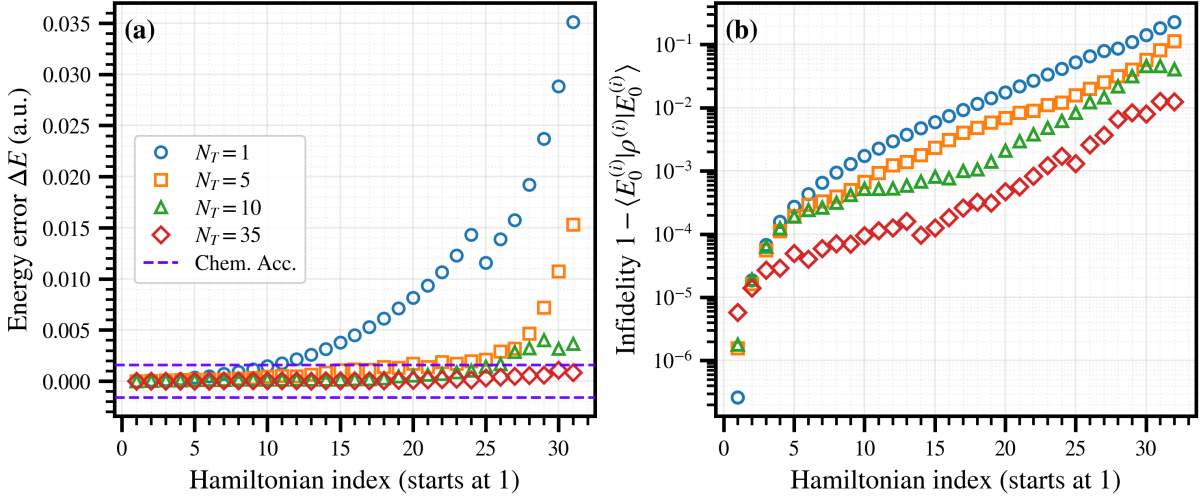


FIG. 3. (a) Energy error $\Delta E(N_T) = \left| \text{tr} \left(H(e^{\tau \mathcal{L}})^{N_T} [\rho^{(0)}] \right) - E_0 \right|$ (a.u.) after N_T application of the dissipative time step at each successive Hamiltonian along a discretized path, beginning from the ground state of $H(0)$, $\rho^{(0)} = |E_0^{(0)}\rangle\langle E_0^{(0)}|$, on the H_4 potential energy surface (STO-3G) where we take $\tau = 0.01$ in these numerical simulations; the final chemical geometry is the transition state (square H_4 molecule) corresponding to $s = 0.5$ and the 32nd Hamiltonian along the reaction path. Each marker shows the final energy estimate after N_T dissipative time steps per Hamiltonian along the reaction path, with $N_T \in \{1, 5, 10, 35\}$ and Hamiltonian indices starting at $H(s_1)$. Chem. Acc. indicates where the threshold for *chemical accuracy* is: 1.6 mHa. (b) Corresponding infidelity $1 - \langle E_0^{(i)} | \rho^{(i)} | E_0^{(i)} \rangle$ on a logarithmic scale for the same runs, showing that larger N_T improves preparation fidelity across the path where $|E_0^{(i)}\rangle$ is the ground state of the i -th reaction path Hamiltonian $H(s_i)$ and $\rho^{(i)}$ is the approximate ground state prepared via dissipative evolution.

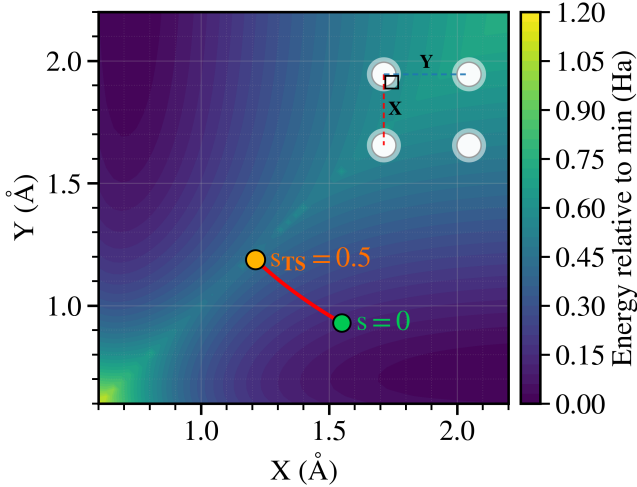


FIG. 4. H_4 potential energy surface (STO-3G) over rectangular geometries parameterized by (X, Y) , with the reaction-path segment connecting $s = 0$ weakly correlated starting point to the target transition state (TS) point $s = 0.5$. The path follows a rectangle distortion of H_4 at fixed area $XY = a^2$, with atoms at $(\pm X/2, \pm Y/2, 0)$ and aspect ratio swept as $\lambda(s) = \lambda_{\min}^{1-s} \lambda_{\max}^s$ with $\lambda_{\min} = 0.6$, $\lambda_{\max} = 1.6$, and $X = a/\sqrt{\lambda}$, $Y = a\sqrt{\lambda}$ for $s \in [0, 0.5]$; the square geometry with side length $a = 1.2$ Å occurs at $s = 0.5$ and exhibits strong multi-reference character.

Up to constants from the discretization step, the number of distinct real-time evolution calls (the number of sample points in the time integral) is proportional to the time support length $\Theta(S(\varepsilon_{\text{leak}}))$.

A more detailed statement of Theorem 2 and its proof are provided in the Section F as Theorem 4.

For Gevrey filters, the dominant accuracy parameter is M_s the number of quadrature points [20]. For Fourier filters, this parameter is the number of Fourier modes N_ω ; see Section F. The values of these parameters are set by the target ground-state leakage $\varepsilon_{\text{leak}}$. In practice, the conversion between target leakage $\varepsilon_{\text{leak}}$ and the accuracy parameter value is straightforward in the case of the Fourier filter e.g., $N_\omega \sim 1000$ Fourier modes can tackle spectral gaps in the milliHartrees. In contrast, a Gevrey filter's optimal parameters are more difficult to determine a priori [20].

B. Numerical Demonstrations

H_4 Molecule at the Multi-reference Square Geometry

We consider a one-dimensional path on the Born–Oppenheimer potential energy surface (PES) of planar H_4 . To reduce complexity, we consider a path along which the nuclei remain in a rectangular configuration (i.e., the angle between the axes of the pairs

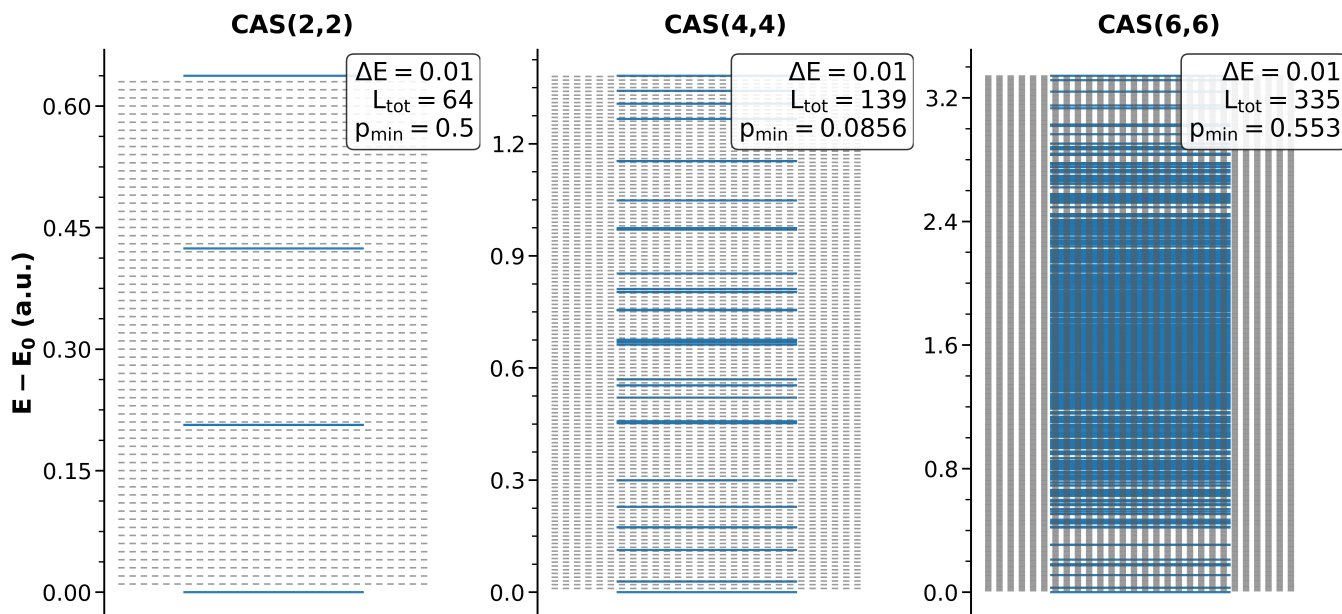


FIG. 5. Energy spectra at the cyclobutadiene automerization transition-state geometry (the square C_4H_4 molecule) for increasing active spaces CAS(2,2), CAS(4,4), and CAS(6,6). In each panel, CASSCF eigenenergies are plotted relative to the ground state, $E_j - E_0$, as horizontal ticks. Gray dashed guides indicate a uniform discretization into energy “layers” of width $\Delta E = 0.01$ (a.u.), used to define the layer index $L(j) = \lfloor (E_j - E_0)/\Delta E \rfloor$ and the total number of layers $L_{\text{tot}} = \lceil (E_{\text{max}} - E_0)/\Delta E \rceil$. Insets report L_{tot} and the measured downhill-drift statistic p_{min} which is independent of system size leading to ETH-like behavior in the chemical system.

is fixed), reducing the dimension of the energy manifold to a two-dimensional surface, with the aspect ratio between the separation of the pairs varied smoothly as a function of the reaction coordinate $s \in [0, 1]$; see Fig. 4. The path is chosen to pass through the configuration in which the nuclei sit in a perfect square (that is, the rectangular configuration has equal length sides).

This square geometry of the H_4 molecule is non-trivial from both chemical and algorithmic perspectives: in the STO-3G basis near a side length of ~ 1.2 Å, the increased symmetry induces near-degeneracies among competing bonding patterns, producing a strongly multi-reference ground state and a compressed low-energy spectrum [50]. Thus, the rectangular-to-square deformation provides a minimal proxy for a reaction coordinate that crosses a strongly correlated “bottleneck” region, while remaining small enough FCI dimension to allow us to classically simulate the performance of our algorithm. Additionally, we ran our Procrustes alignment procedure described by Proposition 1 in order to establish a consistent orbital gauge along the path. The alignment procedure begins at the end of the reaction path, aligning the basis of $H(s_{N_H-2})$ to the “products” geometry $H(s_{N_H-1} = 1)$, then $H(s_{N_H-3})$ is aligned with $H(s_{N_H-2})$ and so on until the “reactant” geometry is reached $H(s_0 = 0)$.

We employ quadratic, number-conserving jump operators $A_{ij}^{(1)} = c_i^\dagger c_j + c_j^\dagger c_i$ and $A_{ij}^{(2)} = i(c_i^\dagger c_j - c_j^\dagger c_i)$ for $i < j$, allowing for spin mixing between, for example, α and β orbitals. With this selected dissipative ansatz, we

observe the desired ETH-like behavior in the H_4 molecule by visualizing the graph $G = (V, E)$ associated with the Markov process induced by dissipative cooling, which lends credibility to the assumption being made in this regime. The vertices of G are the eigenstates in the FCI subspace $V = \{|E_i\rangle\}_{i=0}^{D-1}$ and two eigenstates are connected by an edge $(|E_i\rangle, |E_j\rangle) \in E$ if the probability of a transition between the two is non-zero $P_{i \rightarrow j} > 0$. Fig. 1a depicts a visualization of the graph G with the energy-ordered vertices arranged on a circle, where edges are only drawn if their transition probability is bound below by $P_{j \rightarrow k} \geq 0.01$. We can observe that H_4 is consistent with ETH at the square multi-reference geometry, as it satisfies the uniform drift condition of Eq. (19).

Fig. 3a demonstrates that increasing the number of dissipative steps per geometry leads to convergence to the true ground state at all points along the reaction path for this example. Indeed, as shown, $N_T = 35$ dissipative steps are sufficient to achieve chemical accuracy, $\epsilon_E \leq 1.6$ mHa, across all N_H geometries. Fig. 3b shows the infidelity of the prepared state with the true ground state. As we can see, even one application of the dissipative step per geometry allows for a reasonable overlap with the true ground state at the transition-state geometry. Increasing the number of applications only improves the simulation. These numerical simulations show rapid convergence, corresponding to short mixing times, at each geometry along the path. One could imagine a scenario where the number of dissipative steps is tuned along the path (increasing

with the proximity to the TS) to minimize cost, while maximizing accuracy.

ETH-like Behavior in Small Active Spaces

In this work, our foundational posit is that the probability of successfully lowering the energy during the execution of dissipative dynamics is independent of system size; specifically at chemical transition states. Remarkably, we can observe this ETH-like behavior in small chemical systems. Here we consider the cyclobutadiene automerization transition-state geometry, the square C_4H_4 molecule, in increasing active spaces CAS(2,2), CAS(4,4), and CAS(6,6). In Fig. 5, we show, for a fixed choice of microcanonical window width $\Delta E = 0.01$, the distribution of the spectrum over these microcanonical windows. We observe that p_{\min} is independent of system size as we increase the size of the active space. This observation suggests that ETH-like behavior is abundant in the world of chemical systems from nature that satisfy generic symmetries, namely particle conservation.

C. Cost Analysis

To assess the practical prospects for efficient dissipative ground-state preparation along reaction paths, we estimate the logical quantum resources required to prepare ground states for strongly correlated chemical systems along such paths, using optimized quantum circuit encodings [51].

Several quantum algorithms can be used to implement time steps that approximate the purely cooling dynamics generated by $\{K_a\}_{a \in \mathcal{A}}$. Broadly, these approaches fall into two classes: collision-based schemes, in which interactions with one or more ancilla qubits induce dissipative kicks that drive the system’s energy downward [20, 21]; and quantum operator Fourier transform–based circuits, which realize the desired filter function using coherent ancilla states of the form $\sum_i \sqrt{f(t_i)}|i\rangle$ together with controlled time evolution [22, 53].

Dissipative kicks are considered to be the most viable near-term approach for implementing dissipative dynamics on quantum computers [21]. For this class of methods, the circuit depth required to implement a short-time dissipative evolution is determined by the leakage properties of the chosen filter function.

For the purpose of resource estimation, we select a periodic square-wave filter consisting of N_ω Fourier modes and perform time evolution $\exp(\pm iHt)$ using the QSP/QSVT framework [54–58]. Then, the cost of implementing a single time step via the $W(\sqrt{\tau})$ operator can be quantified by the total number of calls N_{U_H} to the block encoding U_H of the electronic Hamiltonian of interest

$$N_{U_H} = \Theta(2N_\omega(\pi\|H\|/2 + \log 1/\epsilon)). \quad (29)$$

In this expression, $\Theta(\pi\|H\|/2 + \log 1/\epsilon)$ is the optimal runtime complexity of the quantum simulating using the QSVT where $t = \pi/2$ when using a periodic square wave filter. Therefore, we can approximate the total logical gate complexity as

$$N_H \times N_T \times N_{U_H} \times \text{Cost}(U_H), \quad (30)$$

up to variation in the cost of the block-encoding along the reaction path and the cost of implementing the jump operator kicks. Here, N_T is the number of discrete time steps $W(\sqrt{\tau})$ applied to implement sufficient dissipative cooling to converge to the ground state at each point along the reaction path.

Reducing the cost of implementing block encodings of electronic structure Hamiltonians $\text{Cost}(U_H)$ has been a pervasive subject of recent quantum algorithms research. There are now many schemes for compressing and encoding electronic structure Hamiltonians into quantum circuits [30, 51]. At present, the state-of-the-art is achieved by using a combination of several compression protocols resulting in the “DFTHC-BLISS-SA” block encoding [51]. These optimized block encodings have established the lowest quantum resource cost for investigating chemical reactions, enabling quantum solutions to several application areas that carry significant scientific utility.

Fig. 6 summarizes our logical resource estimates for a single dissipative time step $W(\sqrt{\tau})$ along with the cost for quantum phase estimation (QPE) with chemical accuracy $\sigma_{\text{PEA}} = 1$ mHa for representative systems for each of these application areas. In the strongly correlated regimes in which these systems live, we report resource estimates for $N_\omega = 1000$ Fourier modes for the filter function $f(t)$ given that spectral gaps on the order of 1 mHa are common when studying transition states. Note that the QPE costs presented are single-shot QPE, and do not account for infidelity of the initial state. There is no way to guarantee (even an inverse polynomial) overlap of the initial ansatz state at the TS configuration, resulting in many repetitions that increase the cost of the QPE, potentially by orders of magnitude that will dwarf the apparent mismatch.

We observe that the cost of implementing the dissipative cooling operator W is more than an order of magnitude greater than that of QPE. This motivates the exploration of methods to decrease the total number of W operators that need to be applied at once during any single coherent run of a quantum circuit during the execution of our algorithm. We can employ techniques developed in [59]. The authors demonstrate how machine learning can be used to learn a function $\nu(\mathbf{R}; \gamma)$, where γ are the neural network parameters and \mathbf{R} are the chemical geometries along the reaction path. This function determines the parameterization of a variational circuit $U(\nu(\mathbf{R}; \gamma))|\psi_0(\mathbf{R})\rangle$, where $|\psi_0(\mathbf{R})\rangle$ is some geometry dependent initial state that gets us into the right region of Hilbert space in order to find a low-depth circuit representation U of the ground state at each point along the reaction path. Using this approach to obtain ground states along a reaction path,

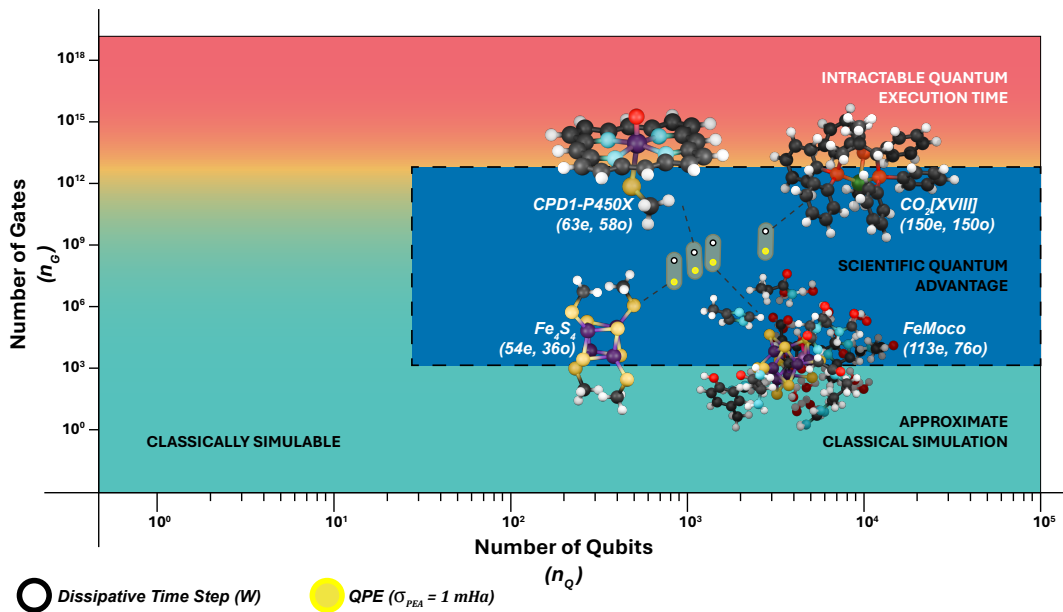


FIG. 6. Quantum logical resource estimates for a single dissipative time step operator $W(\sqrt{\tau}) \approx e^{\tau\mathcal{L}}$ along with the cost of doing QPE across benchmark chemical systems [51]. The resource estimates are calculated from resource estimates provided in [51] for QPE and the block encoding U_H using the “DFTHC-BLISS-SA” SOTA electronic structure compression method to minimize T /Toffoli gate counts. Each point corresponds to a row in Table II, with Toffoli count on the vertical axis and logical qubits on the horizontal axis. Regions of current and projected hardware capabilities are shaded to illustrate which systems and algorithms may be accessible on near- or medium-term fault-tolerant devices [52].

we could manage with as few as just a single W . Our numerical study of the H_4 near its square geometry shows that in regions further from the transition state (emulated by the square geometry of H_4), only a single W is required to maintain overlap.

IV. DISCUSSION

A large part of the inspiration for this work comes from how tensor-network solvers such as DMRG are used in practice to map the boundary between classically tractable and classically hard regions of chemical reaction paths: in many systems, tensor-network methods provide chemically accurate reference energies and high-quality guiding states over large portions of the path, yet they can degrade near strongly correlated transition-state geometries where the wavefunction becomes highly entangled. We therefore use tensor-network performance as a practical indicator of where to deploy our dissipative state-preparation subroutine: the overall strategy is to exploit classical structure where available (to obtain warm starts and reliable energies) while reserving the quantum overhead of the engineered cooling primitive W for the narrow multi-reference window near the transition state, where the mixing time can be large and classical ansätze lose accuracy.

In this work, we develop an efficient quantum algorithm—*dissipative evolution*—that transports approximate ground

states along reaction paths starting from equilibrium chemical geometries (products and reactants) and ending in the classically difficult regime near transition state chemical geometries where we find quantum advantage. Our algorithm incurs a polynomial overhead bounded by $\tilde{O}(N_o^3)$. If our reaction pathway is sufficiently smooth (smaller values for the Davis-Kahan constant C_{DK} then we can expect nearly linear polynomial overhead introduced by our algorithm i.e., $\tilde{O}(C_{DK}^2 N_o / \epsilon_E)$ Theorem 3. Furthermore, a path can be optimized to maintain smoothness and the gap. This runtime improves upon several other quantum algorithms capable of preparing ground states along reaction pathways, including digital adiabatic evolution and phase randomization [2, 31]. Additionally, we validate our algorithm by numerically preparing the ground state of the square H_4 molecule whose geometry introduces strong correlation and therefore is a popular benchmark for dissipative ground state preparation algorithms [20, 29]. We conclude with resource estimates for chemical systems that carry significant scientific utility [51]; our resource estimates are largely derived from the analysis of the cooling primitives introduced in [20] with modifications to the filter function and physical regime.

Our results build on recent progress in quantum algorithms for simulating dissipative dynamics, and we provide an end-to-end complexity guarantee under an ETH-motivated rapid-mixing condition for the engineered cooling primitive, implying that even classically hard

transition-state instances can be refined efficiently toward the ground state by dissipative evolution. Strongly correlated, classically hard instances of this type are ubiquitous in nature [26, 36, 60, 61]. FeMoco, for example, has long served as a canonical strongly correlated target for quantum chemistry; recent work has demonstrated an equilibrium-geometry classical ansatz with very high overlap for FeMoco, rendering QPE efficient at or near equilibrium [4] and strengthening the case for concentrating quantum resources on out-of-equilibrium regimes where classical tensor-network methods remain most challenged. In our setting, equilibrium-quality classical solutions provide warm starts near reactant or intermediate geometries, while the quantum dissipative step is used to propagate through the transition-state window where classical methods fail, enabling chemical-accuracy barrier heights relevant for screening and design of FeMoco-inspired synthetic analogues [62].

Looking ahead, several complementary directions could further reduce costs and broaden applicability. First, trajectory-style approaches suggest that even faster mixing may be achievable by interleaving dissipative evolution with QPE-based primitives [63]; consistent with this, our logical resource estimates (Fig. 6) indicate that QPE can be substantially cheaper than a single application of W , suggesting that QPE interleaving could reduce the required number of W applications. Second, approximate ground-state generation methods such as that of Ceroni *et al.* [59] may further reduce the total W budget over an entire pathway. Third, it is useful to distinguish *basis-set error* from *algorithmic hardness*: O’Gorman *et al.* [23] prove that approximating the ground-state energy of the electronic-structure Hamiltonian can remain QMA-complete even when restricted to a fixed single-particle basis and fixed particle number, by encoding hardness in the choice of orbitals used to discretize the problem, and they further show NP-completeness of determining the lowest-energy Slater determinant (Hartree–Fock) within such a fixed basis. They also explicitly pose as open directions whether the problem becomes easier when one *promises* a bounded basis-set error (i.e., that the chosen basis contains a state sufficiently close to the true ground state) and, separately, how complexity changes when the basis is drawn from a parameterized family and must be selected as part of the instance.

From the perspective of reaction-path algorithms, this suggests a principled interface between representation and dynamics: rather than viewing basis selection as a purely classical preprocessing step, one can treat it as a controllable design degree of freedom coupled to the cooling dynamics, with the aim of compressing entanglement growth and shrinking the width of the hard transition-state window before invoking expensive dissipative refinement. More broadly, the nuclear geometry $\mathbf{R}(s)$ should be viewed as an additional design space rather than a fixed linear interpolation: one can adaptively choose the path discretization and even deform the path in \mathbf{R} -space

to reduce the onset of strong correlation and minimize the total number of costly refinement steps. Finally, since coherent transport, QPE refinement, and dissipative evolution are not mutually exclusive, a unified theory of when coherent transport suffices and when it is optimal to switch to dissipative refinement would be valuable; in this direction, quantum speed-limit results for adiabatic algorithms at zero and finite temperature [64] may provide principled criteria for strategy switching, including variants that transport a Gibbs state and cool only near the end, or that learn finite temperature reaction rates and extrapolate toward the near-room-temperature regime rather than strictly preparing the ground state directly.

Another promising direction for future work is to incorporate into our algorithm the *Dissipative Quantum Eigensolver* (DQE) framework of Cubitt [65], which formalizes ground-state preparation as an iterated *quantum instrument*: the algorithm repeatedly applies weak, local generalized measurements (realizing an AGSP as one Kraus branch) and uses an explicit *stopping rule* that depends only on the observed measurement record, thereby providing an intrinsic operational “success certificate” without requiring coherent phase estimation or deep reversible arithmetic. Notably, Cubitt emphasizes that a large portion of the DQE circuit can be implemented with Clifford operations, with only a single non-Clifford single-qubit rotation applied on a fixed ancilla line in a representative construction—an architectural feature that directly aligns with our emphasis on low- T overhead primitives and mid-circuit measurement as an algorithmic resource. Building on this, Purcell, Rajput, and Cubitt [66] prove that for *stabilizer-encoded* (geometrically local) Hamiltonians of the type that naturally arise in fermion-to-qubit encodings, a modified DQE procedure under circuit-level depolarizing noise can suppress the additive error in the final ground-space overlap *exponentially in the code distance*, moving toward fault-tolerant-quality state preparation *without* the full overhead of universal fault tolerance; in contrast, they show that dissipative quantum computation (as a model for general computation) does not enjoy such an intrinsic robustness advantage over the standard circuit model.

ACKNOWLEDGMENTS

The authors thank Ryan Mann, Gabriel Waite, Mauro E. S. Morales, Saurabh Totey and Adam Holmes for helpful discussions. S.J.E, T.W.W and N.N would also like to thank the attendees of the IPAM: Frontiers for Open Systems Workshop of whom there are too many to name. M.J.B., S.S., D. C., and S.J.E. acknowledge the support of the ARC Centre of Excellence for Quantum Computation and Communication Technology (CQC2T), project number CE17010001. Finally, we owe a debt of gratitude to Itay Hen for organizing a collaboration venue at USC.

- [1] V. von Burg, G. H. Low, T. Häner, D. S. Steiger, M. Reiher, M. Roetteler, and M. Troyer, *Physical Review Research* **3**, 033055 (2021).
- [2] D. An, P. C. S. Costa, and D. W. Berry, *Large time-step discretisation of adiabatic quantum dynamics* (2025), arXiv:2509.00171.
- [3] N. Nguyen, T. W. Watts, B. Link, K. S. Williams, Y. R. Sanders, S. J. Elman, M. Kieferova, M. J. Bremner, K. J. Morrell, J. Elenewski, E. B. Isaacs, S. D. Johnson, L. Mathieson, K. M. Obenland, M. Otten, R. Sundareswara, and A. Holmes, *npj Quantum Information* **12**, 27 (2026).
- [4] H. Zhai, C. Li, X. Zhang, Z. Li, S. Lee, and G. K.-L. Chan, *Classical solution of the femo-cofactor model to chemical accuracy and its implications* (2026), arXiv:2601.04621.
- [5] J. J. Goings, A. White, J. Lee, C. S. Tautermann, M. Degroote, C. Gidney, T. Shiozaki, R. Babbush, and N. C. Rubin, *Proceedings of the National Academy of Sciences* **119**, e2203533119 (2022).
- [6] S. Lee, J. Lee, H. Zhai, Y. Tong, A. M. Dalzell, A. Kumar, P. Helms, J. Gray, Z.-H. Cui, W. Liu, M. Kastoryano, R. Babbush, J. Preskill, D. R. Reichman, E. T. Campbell, E. F. Valeev, L. Lin, and G. K.-L. Chan, *Nature Communications* **14**, 1952 (2023).
- [7] A. Y. Kitaev, *Quantum measurements and the Abelian stabilizer problem* (1995), arXiv:quant-ph/9511026.
- [8] Y. Ge, J. Tura, and J. I. Cirac, *Journal of Mathematical Physics* **60**, 022202 (2019).
- [9] N. S. Mande and R. de Wolf, *LIPICs, ESA 2023* **274**, 81:1 (2023).
- [10] A. Aspuru-Guzik, A. D. Dutoi, P. J. Love, and M. Head-Gordon, *Science* **309**, 1704 (2005).
- [11] J. D. Whitfield, J. Biamonte, and A. Aspuru-Guzik, *Molecular Physics* **109**, 735 (2011).
- [12] P. J. J. O'Malley, R. Babbush, I. D. Kivlichan, J. Romero, J. R. McClean, R. Barends, J. Kelly, P. Roushan, A. Tranter, N. Ding, B. Campbell, Y. Chen, Z. Chen, B. Chiaro, A. Dunsworth, A. G. Fowler, E. Jeffrey, A. Megrant, J. Y. Mutus, C. Neill, C. Quintana, D. Sank, A. Vainsencher, J. Wenner, T. C. White, P. V. Coveney, P. J. Love, H. Neven, A. Aspuru-Guzik, and J. M. Martinis, *Physical Review X* **6**, 031007 (2016).
- [13] I. Kassal and A. Aspuru-Guzik, *The Journal of Chemical Physics* **131**, 224102 (2009).
- [14] I. Kassal, S. P. Jordan, P. J. Love, M. Mohseni, and A. Aspuru-Guzik, *Proceedings of the National Academy of Sciences* **105**, 18681 (2008).
- [15] B. P. Lanyon, J. D. Whitfield, G. G. Gillet, M. E. Goggin, M. P. Almeida, I. Kassal, J. D. Biamonte, M. Mohseni, B. J. Powell, M. Barbieri, A. Aspuru-Guzik, and A. G. White, *Nature Chemistry* **2**, 106 (2010).
- [16] M. Motta, C. Sun, A. T. K. Tan, M. J. O'Rourke, E. Ye, A. J. Minnich, F. G. S. L. Brandão, and G. K.-L. Chan, *Nature Physics* **16**, 205 (2020).
- [17] C. Cade, M. Folkertsma, S. Gharibian, R. Hayakawa, F. Le Gall, T. Morimae, and J. Weggemans, *LIPICs, 50th ICALP 2023*, 32:1 (2023), arXiv:2207.10250.
- [18] S. Gharibian and F. Le Gall, *SIAM Journal on Computing* **52**, 1009 (2023).
- [19] G. Waite, K. Lin, S. J. Elman, and M. J. Bremner, *Physically-motivated guiding states for local Hamiltonians* (2025), arXiv:2509.25815.
- [20] Z. Ding, C.-F. Chen, and L. Lin, *Physical Review Research* **6**, 033147 (2024).
- [21] Z. Ding, Y. Zhan, J. Preskill, and L. Lin, *End-to-end efficient quantum thermal and ground state preparation made simple* (2025), arXiv:2508.05703.
- [22] C.-F. Chen, H.-Y. Huang, J. Preskill, and L. Zhou, *Nature Physics* **21**, 654 (2025), arXiv:2309.16596.
- [23] B. O'Gorman, S. Irani, J. Whitfield, and B. Fefferman, *PRX Quantum* **3**, 020322 (2022).
- [24] N. Schuch and F. Verstraete, *Nature Physics* **5**, 732–735 (2009).
- [25] J. D. Whitfield, P. J. Love, and A. Aspuru-Guzik, *Phys. Chem. Chem. Phys.* **15**, 397–411 (2013).
- [26] M. Reiher, N. Wiebe, K. M. Svore, D. Wecker, and M. Troyer, *Proceedings of the National Academy of Sciences* **114**, 7555 (2017).
- [27] R. Puig, B. Casas, A. Cervera-Lierta, Z. Holmes, and A. Pérez-Salinas, *Warm starts, cold states: Exploiting adiabaticity for variational ground-states* (2026), arXiv:2602.06137 [quant-ph].
- [28] H.-E. Li and L. Lin, *Dissipative quantum algorithms for excited-state quantum chemistry* (2025), arXiv:2512.19870.
- [29] H.-E. Li, Y. Zhan, and L. Lin, *npj Quantum Information* **11**, 183 (2025).
- [30] M. Motta, E. Ye, J. R. McClean, Z. Li, A. J. Minnich, R. Babbush, and G. K.-L. Chan, *npj Quantum Information* **7**, 83 (2021).
- [31] S. Boixo, E. Knill, and R. D. Somma, *Eigenpath traversal by phase randomization* (2009), arXiv:0903.1652.
- [32] D. A. Levin, Y. Peres, and E. L. Wilmer, *Markov Chains and Mixing Times*, American Mathematical Society, Student Mathematical Library (American Mathematical Society, Providence, RI, 2009).
- [33] M. J. Kastoryano and F. G. Brandao, *Communications in Mathematical Physics* **344**, 915 (2016).
- [34] K. S. Williams, V. Rodriguez-Santiago, and J. W. Andzelm, *Electrochim. Acta* **210**, 261 (2016).
- [35] D. Motlagh, M. S. Zini, J. M. Arrazola, and N. Wiebe, *Ground state preparation via dynamical cooling* (2024), arXiv:2404.05810 [quant-ph].
- [36] J. J. Wardzala, D. S. King, L. Ogunfowora, B. Savoie, and L. Gagliardi, *ACS Central Science* **10**, 833 (2024).
- [37] P. G. Szalay, T. Müller, G. Gidofalvi, H. Lischka, and R. Shepard, *Chemical Reviews* **112**, 108 (2012).
- [38] W. Jiang, N. J. DeYonker, and A. K. Wilson, *Journal of Chemical Theory and Computation* **8**, 460 (2012).
- [39] P. Sharma, J. J. Bao, D. G. Truhlar, and L. Gagliardi, *Annual Review of Physical Chemistry* **72**, 541 (2021).
- [40] A. Jacot, F. Gabriel, and C. Hongler, *Advances in neural information processing systems* **31**, 10.1145/3406325.3465355 (2018).
- [41] A grid is fixed by calculating N_H and distributing accordingly to the magnitude of gradient.
- [42] T. Nguyen and M. Kieferová, *Theoretical guarantees of variational quantum algorithm with guiding states* (2025), arXiv:2510.06764.

- [43] I. S. K. Kerkin, Z. Wang, P. Zhang, and K. Morokuma, *Mol. Phys.* **107**, 1017 (2009).
- [44] D. Sheppard, R. Terrell, and G. Henkelman, *The Journal of Chemical Physics* **128**, 134106 (2008).
- [45] G. Henkelman and H. Jónsson, *The Journal of Chemical Physics* **113**, 9978 (2000).
- [46] G. Henkelman, B. P. Uberuaga, and H. Jónsson, *The Journal of Chemical Physics* **113**, 9901 (2000).
- [47] H. Jónsson, G. Mills, and K. W. Jacobsen, in *Classical and Quantum Dynamics in Condensed Phase Simulations*, edited by B. J. Berne, G. Ciccotti, and D. F. Coker (World Scientific, Singapore, 1998) pp. 385–404.
- [48] E. B. Davies, *Communications in Mathematical Physics* **39**, 91 (1974).
- [49] E. B. Davies, *Mathematische Annalen* **219**, 147 (1976).
- [50] Y. Liu, P. G. Jambrina, J. F. E. Croft, N. Balakrishnan, F. J. Aoiz, and H. Guo, *J. Chem. Theory Comput.* **20**, 1829 (2024).
- [51] G. H. Low, R. King, D. W. Berry, Q. Han, A. E. DePrince, A. F. White, R. Babbush, R. D. Somma, and N. C. Rubin, *Physical Review X* **15**, 041016 (2025).
- [52] D. Camps, E. Rrapaj, K. Klymko, H. Kim, K. Gott, S. Darbha, J. Balewski, B. Austin, and N. J. Wright, *Quantum computing technology roadmaps and capability assessment for scientific computing – an analysis of use cases from the NERSC workload* (2025), arXiv:2509.09882.
- [53] C.-F. Chen, M. J. Kastoryano, F. G. Brandão, and A. Gilyén, *Quantum thermal state preparation* (2023), arXiv:2303.18224.
- [54] A. Gilyén, Y. Su, G. H. Low, and N. Wiebe, in *Proceedings of the 51st annual ACM SIGACT symposium on theory of computing* (2019) pp. 193–204.
- [55] G. H. Low and I. L. Chuang, *Physical Review Letters* **118**, 010501 (2017).
- [56] G. H. Low and I. L. Chuang, *Quantum* **3**, 163 (2019), arXiv:1610.06546 [quant-ph].
- [57] G. H. Low, T. J. Yoder, and I. L. Chuang, *Physical Review X* **6**, 041067 (2016), arXiv:1603.03996 [quant-ph].
- [58] J. Haah, *Quantum* **3**, 190 (2019).
- [59] J. Ceroni, T. F. Stetina, M. Kieferova, C. Ortiz Marrero, J. M. Arrazola, and N. Wiebe, *Generating approximate ground states of molecules using quantum machine learning* (2023), arXiv:2210.05489.
- [60] B. Rudsteyn, D. Coskun, J. L. Weber, E. J. Arthur, S. Zhang, D. R. Reichman, R. A. Friesner, and J. Shee, *Journal of Chemical Theory and Computation* **16**, 3041 (2020).
- [61] M. Otten, T. W. Watts, S. D. Johnson, R. Sundareswara, Z. Wang, T. S. Hardikar, K. Heitritter, J. Brown, K. Setia, and A. Holmes, *Quantum resources required for binding affinity calculations of amyloid beta* (2024), arXiv:2406.18744 [quant-ph].
- [62] Y.-Y. Xu, X.-L. Jiang, J.-L. Chai, S.-J. Qiu, J. He, G. Xu, J. Wei, Q.-X. Yu, H.-Y. Zhang, Y. Li, X.-W. Zhang, G.-L. Cao, Y. Li, Y.-S. Cui, C.-Q. Xu, J. Li, and X.-D. Chen, *Proc. Natl. Acad. Sci. U. S. A.* **122**, e2419655122 (2025).
- [63] J. Jiang, *Predicting properties of quantum thermal states from a single trajectory* (2026), talk at the IPAM workshop “New Frontiers in Quantum Algorithms for Open Quantum Systems”, scheduled Jan 13, 2026, 11:30–12:20 PT.
- [64] L.-Y. Chou and J.-H. Chen, *Universal scaling of finite-temperature quantum adiabaticity in driven many-body systems* (2026), arXiv:2602.01943 [quant-ph].
- [65] T. S. Cubitt, *Dissipative ground state preparation and the dissipative quantum eigensolver* (2023), arXiv:2303.11962 [quant-ph].
- [66] J. Purcell, A. Rajput, and T. Cubitt, *Fault-resilience of dissipative processes for quantum computing* (2025), arXiv:2502.20374 [quant-ph].
- [67] J. M. Deutsch, *Reports on Progress in Physics* **81**, 082001 (2018).
- [68] L. D’Alessio, Y. Kafri, A. Polkovnikov, and M. Rigol, *Advances in Physics* **65**, 239 (2016).
- [69] E. Campbell, *Physical Review Letters* **123**, 070503 (2019).
- [70] Z. Ding, X. Li, and L. Lin, *PRX Quantum* **5**, 020332 (2024).

Appendix A: Preliminaries

This appendix collects the mathematical objects, norms, and conventions used throughout the proofs. Unless stated otherwise, all operators act on a finite-dimensional Hilbert space \mathcal{H} of dimension D (e.g., the FCI space in a fixed symmetry sector at a fixed geometry).

Quantum channels and continuous-time dynamics

A quantum channel is a completely positive trace-preserving (CPTP) map $\mathcal{E} : \mathcal{B}(\mathcal{H}) \rightarrow \mathcal{B}(\mathcal{H})$. A (time-homogeneous) Markovian open-system evolution is described by a one-parameter semigroup $\{e^{t\mathcal{L}}\}_{t \geq 0}$ of CPTP maps with generator \mathcal{L} (the *Lindbladian*).

Definition 7 (GKLS (Lindblad) generator). A linear map $\mathcal{L} : \mathcal{B}(\mathcal{H}) \rightarrow \mathcal{B}(\mathcal{H})$ is a Lindbladian (GKLS generator) if it can be written as

$$\mathcal{L}(\rho) = -i[H, \rho] + \sum_{a \in \mathcal{A}} \left(K_a \rho K_a^\dagger - \frac{1}{2} \{K_a^\dagger K_a, \rho\} \right), \quad (\text{A1})$$

where $H = H^\dagger$ is Hermitian and $\{K_a\}_{a \in \mathcal{A}}$ are jump operators.

In the main text and appendices we often focus on the *purely dissipative* case (drop the Hamiltonian commutator term) because the cooling analysis concerns population flow to low energy.

Energy basis, dephasing, and induced population dynamics

Fix a geometry s and let $H(s) = \sum_{j=0}^{D-1} E_j(s) |E_j(s)\rangle\langle E_j(s)|$ be the electronic Hamiltonian (diagonal in its eigenbasis). For a state ρ , define the associated *energy populations*

$$p_j := \langle E_j(s) | \rho | E_j(s) \rangle, \quad p = (p_0, \dots, p_{D-1}) \in \Delta^{D-1}.$$

We write $\mathcal{D}_s(\rho) := \sum_j \langle E_j(s) | \rho | E_j(s) \rangle |E_j(s)\rangle\langle E_j(s)|$ for the dephasing channel in the energy basis at s .

Many dissipative constructions (including filtered-jump implementations used here) admit a convenient *population picture*: after each short-time dissipative step, one may track the evolution of the diagonal of ρ in the energy basis. This motivates the following induced Markov kernel.

Definition 8 (Markov kernel induced by jump operators). Fix an orthonormal basis $\{|j\rangle\}_{j=0}^{D-1}$ (we will take $|j\rangle = |E_j(s)\rangle$). Given jump operators $\{K_a\}_{a \in \mathcal{A}}$, define unnormalized transition weights

$$\Gamma_{j \rightarrow k} := \sum_{a \in \mathcal{A}} |\langle k | K_a | j \rangle|^2, \quad (\text{A2})$$

and the associated row-stochastic kernel

$$P_{j \rightarrow k} := \frac{\Gamma_{j \rightarrow k}}{\sum_{\ell=0}^{D-1} \Gamma_{j \rightarrow \ell}}. \quad (\text{A3})$$

Then a population vector p updates as $p'_k = \sum_j p_j P_{j \rightarrow k}$.

The eigenstate thermalization hypothesis (ETH) posits that, in generic nonintegrable quantum many-body systems, individual energy eigenstates reproduce thermal expectation values for local observables; in our case, quasi-local filtered jump operators. This property motivates a *uniform drift* condition that formalizes the resulting behavior of the Markov process with kernel P associated with the dissipative dynamics.

Definition 9 (Uniform drift). If dissipative dynamics are perfectly downhill, i.e. $P_{j \rightarrow k} = 0$, whenever $E_k > E_j$, then the chain has a *uniform downward drift*. That is, for every state $j \neq 0$,

$$\sum_{k: E_k \leq E_j - \Delta E_{\text{layer}}} P_{j \rightarrow k} \geq p_{\min} \quad \text{for some } p_{\min} > 0. \quad (\text{A4})$$

See Section B 2 for further details behind the connection between uniform drift and the ETH.

Reaction-path Hamiltonians and discretization

A reaction path is a smooth map $\mathbf{R} : [0, 1] \rightarrow \mathbb{R}^{3N}$ and $H(s) := H_{\text{el}}(\mathbf{R}(s))$. We discretize $[0, 1]$ by $0 = s_0 < s_1 < \dots < s_{N_H} = 1$. A central quantity controlling drift of low-energy projectors is the Davis–Kahan-type integral

$$C_{\text{DK}} := \int_0^1 \frac{\|\partial_s H(s)\|_2}{\Delta(s)} ds,$$

defined in the main text (Definition 3).

Filtered jump operators and leakage

Given an unfiltered operator A_a and a (time-domain) kernel f , we define the filtered operator

$$K_a := \int_{\mathbb{R}} f(t) e^{itH} A_a e^{-itH} dt, \quad (\text{A5})$$

with Fourier transform $\hat{f}(\omega) = \int_{\mathbb{R}} f(t) e^{it\omega} dt$. In the eigenbasis of H , this yields $\langle E_j | K_a | E_k \rangle = \hat{f}(E_j - E_k) \langle E_j | A_a | E_k \rangle$. A *cooling* filter is chosen so that $\hat{f}(\omega)$ suppresses or removes contributions from heating Bohr frequencies (typically $\omega > 0$), leading to small *ground-state leakage* $\|K_f | E_0 \rangle\| \leq \varepsilon_{\text{leak}}$.

Resolved spectral gap

We define the resolved spectral gap as below

$$\Delta_{\text{res}}(s) := \inf(\text{spec}(H(s)) \cap (E_0(s) + \varepsilon_{\text{res}}, \infty)) - (E_0(s) + \varepsilon_{\text{res}}),$$

More intuitively, let the eigenvalues of $H(s)$ be ordered $E_0 \leq E_1(s) \leq \dots$. Let $k(s) := \max\{j : E_j(s) \leq E_0(s) + \varepsilon_{\text{res}}\}$. Then,

$$\Delta_{\text{res}}(s) = E_{k(s)+1}(s) - (E_0(s) + \varepsilon_{\text{res}}).$$

So, the resolved spectral gap is the energy difference between the top of the lower-energy band $E_0(s) + \varepsilon_{\text{res}}$ and the next eigenvalue above the cutoff separating the chosen low-energy band from the rest of the spectrum. If $\varepsilon_{\text{res}} = 0$, Δ_{res} reduces to instantaneous spectral gap $\Delta(s) = E_1(s) - E_0(s)$.

Hitting time, layers, and warm starts

We will use a layer discretization of energy. Fix $\Delta E_{\text{layer}} > 0$ and define the layer index

$$L(j) := \left\lceil \frac{E_j - E_0}{\Delta E_{\text{layer}}} \right\rceil \in \mathbb{N}_0, \quad (\text{A6})$$

so $L(0) = 0$. For the Markov chain $(J_t)_{t \geq 0}$ with kernel P , define the ground-state hitting time

$$\tau_0 := \inf\{t \in \mathbb{N}_0 : J_t = 0\}.$$

A *warm start* is an initial law μ such that most mass lies in low layers, e.g., $\Pr_{J_0 \sim \mu}(L(J_0) > L_\mu) \leq \eta$ for some L_μ and small η .

Appendix B: Efficient ground-state preparation along reaction paths

Theorem 3 establishes sufficient conditions for efficient ground state preparation along reaction paths, particularly in the strongly correlated regime near transition states. The proof relies on decomposing the problem into three lemmas that collectively demonstrate a total runtime linear in the number of orbitals N_o (up to polylogarithmic factors). In this section, we first formalize the main complexity result in Theorem 3 then provide proofs for all theorems and the supporting lemmas.

Theorem 3 (Efficient ground-state preparation along reaction paths). *Consider a Lipschitz smooth reaction path (Definition 2) discretized into N_H steps. Under the conditions of Lemma 2 and Lemma 3, for any target error $\epsilon_E > 0$, the reaction-path algorithm prepares a final state ρ_{N_H} satisfying*

$$|\mathrm{tr}(H(1)\rho_{N_H}) - E_0(1)| \leq \epsilon_E$$

with a total gate complexity of

$$\tilde{O}\left(\frac{C_{\mathrm{DK}}^2 N_o}{\epsilon_E}\right) \leq \tilde{O}\left(\frac{\|H\|}{\Delta_{\min}^3} \cdot \frac{1}{\epsilon_E} \cdot N_o^3\right). \quad (\mathrm{B1})$$

Here C_{DK} is the geometric Davis-Kahan constant defined in Definition 3.

1. Lemma 1 (Formal): Overlap between adjacent points on reaction paths

Lemma 5 (Lemma 1 (Formal)). *Let $H(s)$ be a Lipschitz-smooth reaction-path Hamiltonian as in Definition 2. Fix an energy resolution $\epsilon_{\mathrm{res}} > 0$ and define the low-energy spectral projector*

$$P_{\leq}(s) := \mathbf{1}\{H(s) \leq E_0(s) + \epsilon_{\mathrm{res}}\}.$$

Then, for any $0 \leq s_a < s_b \leq 1$,

$$\|P_{\leq}(s_a) - P_{\leq}(s_b)\|_2 \leq 2 \int_{s_a}^{s_b} \frac{\|\partial_s H(s)\|_2}{\Delta_{\mathrm{res}}(s)} ds. \quad (\mathrm{B2})$$

In the special case $P_{\leq}(s) = |E_0(s)\rangle\langle E_0(s)|$ (rank one), this implies

$$1 - |\langle E_0(s_a) | E_0(s_b) \rangle|^2 \leq \left(2 \int_{s_a}^{s_b} \frac{\|\partial_s H(s)\|_2}{\Delta(s)} ds\right)^2, \quad (\mathrm{B3})$$

where $\Delta(s) = E_1(s) - E_0(s)$ (equivalently $\Delta_{\mathrm{res}}(s) = \Delta(s)$ when $\epsilon_{\mathrm{res}} = 0$).

Proof. We treat $P_{\leq}(s)$ as a spectral projector onto the low-energy band $(-\infty, E_0(s) + \epsilon_{\mathrm{res}}]$ and proceed in three steps: (i) represent the projector as a contour (Riesz) integral of the resolvent, (ii) differentiate that representation to express $\partial_s P_{\leq}(s)$ in terms of $\partial_s H(s)$, and (iii) bound the resulting integral using the resolved gap, then integrate along the path in s .

The condition $\Delta_{\mathrm{res}}(s) > 0$ means that the threshold energy $E_0(s) + \epsilon_{\mathrm{res}}$ is separated from the rest of the spectrum above it by a buffer of size $\Delta_{\mathrm{res}}(s)$: the part of the spectrum in $(-\infty, E_0(s) + \epsilon_{\mathrm{res}}]$ is spectrally isolated. Fix s and set

$$r(s) := \Delta_{\mathrm{res}}(s)/2.$$

Choose a positively oriented simple closed contour $\Gamma(s)$ in the complex plane that encloses exactly the spectral subset

$$\mathrm{spec}(H(s)) \cap (-\infty, E_0(s) + \epsilon_{\mathrm{res}}]$$

and stays at least distance $r(s)$ away from the remaining spectrum $\mathrm{spec}(H(s)) \cap (E_0(s) + \epsilon_{\mathrm{res}}, \infty)$. Concretely, one can take $\Gamma(s)$ to lie inside the spectral gap region at distance $r(s)$ from the spectrum (for example, a circle of radius $r(s)$ placed in the gap; the precise shape does not matter, only the distance to the spectrum and the fact that it encloses the desired band).

Because $\Gamma(s)$ encloses a spectrally separated portion of $\mathrm{spec}(H(s))$, the corresponding spectral projector is given by the Riesz (Dunford–Taylor) integral

$$P_{\leq}(s) = \frac{1}{2\pi i} \oint_{\Gamma(s)} (zI - H(s))^{-1} dz. \quad (\mathrm{B4})$$

This is a standard consequence of the holomorphic functional calculus (or, equivalently, the spectral theorem): the resolvent has simple poles at eigenvalues, and the contour integral picks out exactly the eigenprojections associated with the eigenvalues inside $\Gamma(s)$.

Write $R(z, s) := (zI - H(s))^{-1}$. For $z \notin \mathrm{spec}(H(s))$, $R(z, s)$ is well-defined, and differentiating the identity

$$(zI - H(s))R(z, s) = I$$

with respect to s yields the resolvent derivative identity

$$\partial_s R(z, s) = R(z, s)(\partial_s H(s))R(z, s). \quad (\text{B5})$$

Since $H(s)$ is Lipschitz-smooth and $\Gamma(s)$ remains a positive distance from the spectrum, the integrand in Eq. (B4) is uniformly bounded on $\Gamma(s)$ and varies smoothly with s , so we may differentiate under the integral sign:

$$\begin{aligned} \partial_s P_{\leq}(s) &= \frac{1}{2\pi i} \oint_{\Gamma(s)} \partial_s (zI - H(s))^{-1} dz \\ &= \frac{1}{2\pi i} \oint_{\Gamma(s)} (zI - H(s))^{-1} (\partial_s H(s)) (zI - H(s))^{-1} dz. \end{aligned} \quad (\text{B6})$$

For any $z \in \Gamma(s)$, by construction

$$\text{dist}(z, \text{spec}(H(s))) \geq r(s) = \Delta_{\text{res}}(s)/2.$$

For a self-adjoint operator $H(s)$, the resolvent norm satisfies

$$\|(zI - H(s))^{-1}\|_2 = \frac{1}{\text{dist}(z, \text{spec}(H(s)))} \leq \frac{2}{\Delta_{\text{res}}(s)}.$$

Using submultiplicativity of the operator norm in Eq. (B6) gives

$$\begin{aligned} \|\partial_s P_{\leq}(s)\|_2 &\leq \frac{1}{2\pi} \oint_{\Gamma(s)} \|(zI - H(s))^{-1}\|_2^2 \|\partial_s H(s)\|_2 |dz| \\ &\leq \frac{1}{2\pi} \text{len}(\Gamma(s)) \left(\frac{2}{\Delta_{\text{res}}(s)} \right)^2 \|\partial_s H(s)\|_2. \end{aligned} \quad (\text{B7})$$

At this point, it can look like a $\Delta_{\text{res}}(s)^{-2}$ dependence. The key is that we may choose $\Gamma(s)$ to lie in the gap with radius proportional to $\Delta_{\text{res}}(s)$, so its length is $O(\Delta_{\text{res}}(s))$. For example, taking $\Gamma(s)$ to be a circle of radius $r(s) = \Delta_{\text{res}}(s)/2$ yields $\text{len}(\Gamma(s)) = 2\pi r(s) = \pi \Delta_{\text{res}}(s)$, and hence

$$\|\partial_s P_{\leq}(s)\|_2 \leq \frac{1}{2\pi} \cdot \pi \Delta_{\text{res}}(s) \cdot \frac{4}{\Delta_{\text{res}}(s)^2} \|\partial_s H(s)\|_2 = \frac{2\|\partial_s H(s)\|_2}{\Delta_{\text{res}}(s)}.$$

By the fundamental theorem of calculus (in operator norm),

$$P_{\leq}(s_b) - P_{\leq}(s_a) = \int_{s_a}^{s_b} \partial_s P_{\leq}(s) ds,$$

so

$$\|P_{\leq}(s_b) - P_{\leq}(s_a)\|_2 \leq \int_{s_a}^{s_b} \|\partial_s P_{\leq}(s)\|_2 ds \leq 2 \int_{s_a}^{s_b} \frac{\|\partial_s H(s)\|_2}{\Delta_{\text{res}}(s)} ds,$$

which is Eq. (B2).

The rank-1 variation of this bound corresponds to $P_{\leq}(s) = |E_0(s)\rangle\langle E_0(s)|$, and thereby

$$\|P_{\leq}(s_a) - P_{\leq}(s_b)\|_2^2 = 1 - |\langle E_0(s_a) | E_0(s_b) \rangle|^2,$$

and squaring Eq. (B2) gives the stated overlap inequality. Setting $\varepsilon_{\text{res}} = 0$ recovers $\Delta_{\text{res}}(s) = \Delta(s)$. ■

2. Lemma 2 & Lemma 3 (Formal): Rapid cooling via Eigenstate Thermalization Hypothesis (ETH)

Large multi-reference eigenstates in huge Full Configuration Interaction (FCI) spaces can be *consistent* with ETH but do not *imply* it. Let $|E_n\rangle = \sum_i C_i^{(n)} |D_i\rangle$ be the n -th energy eigenstate in a Slater-determinant basis $\{|D_i\rangle\}$. Then, a convenient proxy for eigenstate complexity is the inverse participation ratio (IPR),

$$\text{IPR}_n := \sum_i |C_i^{(n)}|^4, \quad N_{\text{eff}} := \text{IPR}_n^{-1}. \quad (\text{B8})$$

Thus, $N_{\text{eff}} \gg 1$ indicates support over many determinants. We emphasize that IPR_n is basis-dependent and is *not* an ETH diagnostic; we use large N_{eff} only as a heuristic indicator of “Fock-space delocalization” in the chosen determinant basis, i.e., that no small subset of determinants dominates the weight within the energetically accessible subspace. Heuristically, such random-like spreading provides an intuitive bridge to ETH: if eigenvectors behave as typical (weakly correlated) superpositions over microcanonically available configurations, then few-body observables tend to self-average on the diagonal and exhibit suppressed, noisy-looking off-diagonals, consistent with ETH.

For our dissipative cooling protocol, the relevant mechanism is that the chosen few-body jump operators $\{K_a\}$ induce a transition graph $G = (V, E)$ on the eigenstates $V = \{|E_i\rangle\}$, with an edge $(i, j) \in E$ whenever $\langle E_i | K_a | E_j \rangle \neq 0$ for some a (See Fig. 1a for an example transition graph visualized). In the multi-reference transition-state (TS) regime, the state support spans a vast subset of this graph. Provided the jump set avoids symmetry-protected bottlenecks (e.g., approximate conserved quantities, weakly coupled fragments, or selection-rule dead ends), the resulting Lindblad dynamics is expected to be *rapidly mixing* within a narrow energy window, while simultaneously opening many *energy-lowering* paths between adjacent shells. This expectation is most justified when the engineered jumps are explicitly energy-biased (e.g., approximately satisfy a detailed-balance/Davies condition, or otherwise preferentially induce downward transitions in energy).

We analyze one application of the dissipative primitive $e^{\tau\mathcal{L}}$ at a fixed geometry for a short time step $\tau > 0$. The induced population update defines a Markov kernel P on energy-eigenstate indices $\{0, 1, \dots, D-1\}$ via $p'_k = \sum_j p_j P_{j \rightarrow k}$, and we take the ground state to be absorbing. The analysis is phrased in terms of (i) a layer size $\Delta E_{\text{layer}} = O(1)$ and (ii) a one-step downhill drift probability p_{min} , defined below, which lower-bounds the chance of decreasing energy by at least one layer while the chain remains inside a microcanonical window \mathcal{J} . Fix a microcanonical window centered at energy E_* with width ΔE , i.e.,

$$\mathcal{J} := \{j : E_j \in [E_* - \frac{\Delta E}{2}, E_* + \frac{\Delta E}{2}]\}, \quad D_{\text{shell}} := |\mathcal{J}|,$$

where for each $j, k \in \mathcal{J}$, write $E := \frac{1}{2}(E_j + E_k)$ and $\omega := E_k - E_j$.

For practical applications, we consider the jump set consisting of fermionic bilinears $A_{ij}^{(1)} = c_i^\dagger c_j + c_j^\dagger c_i$ and $A_{ij}^{(2)} = i(c_i^\dagger c_j - c_j^\dagger c_i)$ for $i < j$. ETH suggests that within such a shell the matrix elements of any few-body operator A (in particular $A \in \{A_{ij}^{(1)}, A_{ij}^{(2)}\}$) take the form

$$\langle E_k | A | E_j \rangle = \bar{A}(E) \delta_{jk} + e^{-S(E)/2} f_A(E, \omega) R_{jk}, \quad (\text{B9})$$

where $E = (E_i + E_j)/2$, $\bar{A}(E)$ is a smooth microcanonical (diagonal) expectation, $S(E)$ is the microcanonical entropy, $f_A(E, \omega)$ is a smooth envelope that varies only on $O(1)$ energy scales, and R_{jk} is an $O(1)$ zero-mean random variable encoding state-to-state fluctuations [67]. Since $e^{S(E_*)} \sim D_{\text{shell}}$ (up to subextensive constants set by ΔE [68]), for $j \neq k$ in the shell and for ω restricted to a bounded interval one has the scaling

$$|\langle E_k | A | E_j \rangle|^2 \sim e^{-S(E)} \sim \frac{1}{D_{\text{shell}}}.$$

Thus, after row-normalization, the induced transition probabilities $P_{j \rightarrow k}$ have no parametrically preferred targets within the energetically allowed set: for a fixed source state $j \in \mathcal{J}$, the probability mass is spread over $\Theta(D_{\text{shell}})$ accessible states k , up to the smooth dependence encoded by $f_A(E, \omega)$.

Now suppose the filter function $f(t)$ that we employ to construct filtered versions of local jump operators is (approximately) one-sided, so that only downhill energy differences $\omega < 0$ contribute appreciably. After row-normalization, this implies that conditioned on being in an eigenstate j in the shell, the induced transition probabilities $P_{j \rightarrow k}$ are roughly comparable across energetically allowed downhill targets k (no strong bottlenecks), so the probability of a “layer-success” event

$$E_k \leq E_j - \Delta E_{\text{layer}}$$

is controlled primarily by how many downhill targets satisfy this inequality. Equivalently, define the success set $S_j = \{k : E_k \leq E_j - \Delta E_{\text{layer}}\}$. ETH suggests the approximation [68]

$$\sum_{k \in S_j} P_{j \rightarrow k} \approx \frac{\#\{k \text{ accessible} : E_k \leq E_j - \Delta E_{\text{layer}}\}}{\#\{k \text{ accessible} : E_k < E_j\}} \approx \frac{\int_{-\infty}^{E_j - \Delta E_{\text{layer}}} \rho(E) dE}{\int_{-\infty}^{E_j} \rho(E) dE},$$

where $\rho(E)$ is the many-body density of states (restricted to the relevant symmetry sector). To estimate this ratio, write $\rho(E) = e^{S(E)}$ with entropy $S(E)$ and microcanonical inverse temperature $\beta(E) = \partial_E S(E)$. For a fixed $O(1)$ energy decrement $\Delta E \equiv \Delta E_{\text{layer}}$, expand

$$S(E_j - \Delta E) = S(E_j) - \beta(E_j) \Delta E + O(\Delta E^2 |S''(E_j)|).$$

If $\beta(E)$ varies slowly across the microcanonical window (and $\Delta E = O(1)$), the quadratic correction is subleading and one obtains the standard density-of-states estimate

$$\frac{\rho(E_j - \Delta E)}{\rho(E_j)} \approx e^{-\beta(E_j)\Delta E}.$$

Moreover, because the integrals above are dominated by their upper limits when $\rho(E)$ grows rapidly, the same scaling carries over (up to constant prefactors) to the cumulative ratio:

$$\frac{\int_{-\infty}^{E_j - \Delta E} \rho(E) dE}{\int_{-\infty}^{E_j} \rho(E) dE} = \Omega(e^{-\beta(E_j)\Delta E}).$$

Putting these steps together yields the heuristic constant-order uniform drift bound (condition),

$$\sum_{k: E_k \leq E_j - \Delta E_{\text{layer}}} P_{j \rightarrow k} \geq p_{\min} = \Omega(e^{-\beta \Delta E_{\text{layer}}}), \quad (\text{B10})$$

throughout a microcanonical window in which $\beta(E)$ is approximately constant. The lemmas below take the existence of such a drift parameter p_{\min} as an explicit assumption and convert it into a quantitative cooling-time bound.

Lemma 6 (Lemma 2 (Formal)). *Consider a Markov Chain $(J_t)_{t \geq 0}$ with associated kernel P , hitting time τ_0 , and initial law μ that is concentrated in low energy layers for a fixed layer width $\Delta E_{\text{layer}} > 0$. That is, let E_j be an energy assigned to state j , with a unique ground state 0 in the sense that $E_j > E_0$ for all $j \neq 0$, and define the layer index as in Eq. (A6), so that initial law (warm-start) satisfies the layer-radius condition $\Pr_{J_0 \sim \mu}(L(J_0) > L_\mu) \leq \eta$ for some $\eta \in (0, 1)$ and $L_\mu \in \mathbb{N}$. If P satisfies the ETH-motivated uniform downward drift condition, Eq. (A4), then, for any $0 < \varepsilon < 1$, if*

$$t \geq \frac{2L_\mu}{p_{\min}} + \frac{8}{p_{\min}} \ln \frac{1}{\varepsilon}, \quad (\text{B11})$$

one has $\Pr(\tau_0 > t) \leq \eta + \varepsilon$. More precisely, for all $t \geq 2L_\mu/p_{\min}$,

$$\Pr(\tau_0 > t) \leq \eta + \exp\left(-\frac{p_{\min}}{8}t\right). \quad (\text{B12})$$

Proof. With the layer index defined above, define the one-step success set

$$S_j := \{k : E_k \leq E_j - \Delta E_{\text{layer}}\} \quad (\text{B13})$$

for each state j , and the corresponding one-step success indicator

$$X_s := \mathbf{1}\{J_{s+1} \in S_{J_s}\}, \quad s \geq 0. \quad (\text{B14})$$

If $J_{s+1} \in S_{J_s}$, then $E_{J_{s+1}} \leq E_{J_s} - \Delta E_{\text{layer}}$, hence

$$L(J_{s+1}) \leq L(J_s) - X_s. \quad (\text{B15})$$

Under perfectly downhill dynamics, $L(J_s)$ is non-increasing in s . Define the one-step success probability

$$p(j) := \Pr(J_{s+1} \in S_j \mid J_s = j) = \sum_{k \in S_j} P_{j \rightarrow k}. \quad (\text{B16})$$

By Eq. (A4), $p(j) \geq p_{\min}$ for every $j \neq 0$.

Let $(U_s)_{s \geq 0}$ be i.i.d. uniform random variables on $[0, 1]$. By the standard inverse-transform construction, we may realize each transition as a measurable function of U_s as follows: conditional on $J_s = j$, partition $[0, 1]$ into intervals of lengths $\{P_{j \rightarrow k}\}_k$, placing the outcomes $k \in S_j$ first. Then Eq. (B16) ensures

$$\{U_s \leq p(j)\} \iff \{J_{s+1} \in S_j\}.$$

Define the Bernoulli benchmark

$$X'_s := \mathbf{1}\{U_s \leq p_{\min}\}. \quad (\text{B17})$$

Since $p(J_s) \geq p_{\min}$ for all $J_s \neq 0$, we have the pathwise domination

$$X_s \geq X'_s \quad \text{for all } s \text{ with } J_s \neq 0. \quad (\text{B18})$$

(After absorption at 0 the event $\{\tau_0 > t\}$ is false, so only times $s < \tau_0$ matter.) Moreover, $(X'_s)_{s \geq 0}$ are i.i.d. Bernoulli(p_{\min}), so $\sum_{s=0}^{t-1} X'_s \sim \text{Binomial}(t, p_{\min})$. Therefore, for any $t \in \mathbb{N}$,

$$\Pr\left(\sum_{s=0}^{t-1} X_s < L_\mu\right) \leq \Pr\left(\sum_{s=0}^{t-1} X'_s < L_\mu\right) = \Pr(\text{Bin}(t, p_{\min}) < L_\mu). \quad (\text{B19})$$

Iterating Eq. (B15) along a sample path gives

$$L(J_t) \leq L(J_0) - \sum_{s=0}^{t-1} X_s. \quad (\text{B20})$$

If $\sum_{s=0}^{t-1} X_s \geq L(J_0)$ then $L(J_t) \leq 0$. Since $L(\cdot) \geq 0$, it follows that $L(J_t) = 0$. By uniqueness of the ground state (i.e. $L(j) = 0 \iff j = 0$), this implies $J_t = 0$, so the process must have hit the ground state by time t , i.e. $\tau_0 \leq t$. Equivalently,

$$\{\tau_0 > t\} \subseteq \left\{ \sum_{s=0}^{t-1} X_s < L(J_0) \right\}. \quad (\text{B21})$$

By the warm-start layer-radius condition,

$$\begin{aligned} \Pr(\tau_0 > t) &\leq \Pr(L(J_0) > L_\mu) + \Pr(\tau_0 > t, L(J_0) \leq L_\mu) \\ &\leq \eta + \Pr\left(\sum_{s=0}^{t-1} X_s < L(J_0), L(J_0) \leq L_\mu\right) \\ &\leq \eta + \Pr\left(\sum_{s=0}^{t-1} X_s < L_\mu\right) \\ &\leq \eta + \Pr(\text{Bin}(t, p_{\min}) < L_\mu), \end{aligned} \quad (\text{B22})$$

where the last step uses Eq. (B19). If $t \geq 2L_\mu/p_{\min}$ then $L_\mu \leq \frac{1}{2}p_{\min}t$, and by a standard Chernoff bound,

$$\Pr(\text{Bin}(t, p_{\min}) \leq \frac{1}{2}p_{\min}t) \leq \exp\left(-\frac{p_{\min}t}{8}\right). \quad (\text{B23})$$

Thus for all $t \geq 2L_\mu/p_{\min}$,

$$\Pr(\tau_0 > t) \leq \eta + \exp\left(-\frac{p_{\min}t}{8}\right). \quad (\text{B24})$$

Finally, choosing $t \geq \frac{8}{p_{\min}} \ln(1/\varepsilon)$ makes the exponential term at most ε , and together with $t \geq 2L_\mu/p_{\min}$ yields Eq. (B11) and the claim. \blacksquare

At step k of the reaction-path discretization, our warm start for $H(s_k)$ is approximately the previous ground state $|E_0(s_{k-1})\rangle$. If our reaction path is *regular* (Definition 2), then $H(s)$ with M terms

$$H(s) = \sum_{a=1}^M h_a(s), \quad (\text{B25})$$

such that each term is uniformly Lipschitz along the path,

$$\|h_a(s) - h_a(s')\| \leq L_h |s - s'| \quad \text{for all } a \text{ and } s, s' \in [0, 1]. \quad (\text{B26})$$

For chemicals in nature, we observe $M = O(N_o)$ [30]. Therefore, for $\delta_k := |s_k - s_{k-1}|$ we have

$$\|H(s_k) - H(s_{k-1})\| \leq \sum_{a=1}^M \|h_a(s_k) - h_a(s_{k-1})\| \leq ML_h \delta_k = O(N_o \delta_k).$$

Consequently, the warm-start excess energy at the new geometry is bounded by

$$\begin{aligned} 0 \leq \langle E_0(s_{k-1}) | H(s_k) | E_0(s_{k-1}) \rangle - E_0(s_k) &\leq 2 \|H(s_k) - H(s_{k-1})\| \\ &\leq 2ML_h\delta_k = O(N_o\delta_k). \end{aligned} \quad (\text{B27})$$

Thus, for an equal-mass (or otherwise bounded-step) mesh with $\delta_k \leq \delta_{\max} = O(1)$, the warm start lies within an extensive energy window:

$$\langle H(s_k) \rangle_{E_0(s_{k-1})} - E_0(s_k) \leq c_E N_o, \quad c_E := 2\left(\frac{M}{N_o}\right)L_h\delta_{\max}.$$

If μ is the dephased (energy-eigenbasis) distribution induced by this warm start at s_k , then $\mathbb{E}_\mu[E_{J_0} - E_0] = \langle H(s_k) \rangle_{E_0(s_{k-1})} - E_0(s_k)$ is $O(N_o)$. This motivates Lemma 6 which shows how we arrive at a mixing time linear in the number of orbitals N_o .

Lemma 7 (Lemma 3 (Formal)). *Adopt the setting of Lemma 6. In our regime, the warm start is supported on an extensive energy range: there exists $c_E > 0$ such that $\Pr_\mu(E_{J_0} - E_0 \leq c_E N_o) \geq 1 - \eta$.*

Then the layer radius may be chosen as $L_\mu \leq \left\lceil \frac{c_E N_o}{\Delta E_{\text{layer}}} \right\rceil$, and consequently, for any $0 < \varepsilon < 1$ it suffices to take

$$t \geq \frac{2}{p_{\min}} \left\lceil \frac{c_E N_o}{\Delta E_{\text{layer}}} \right\rceil + \frac{8}{p_{\min}} \ln \frac{1}{\varepsilon}. \quad (\text{B28})$$

In particular, the cooling time is linear in N_o ,

$$t = O\left(N_o + \ln \frac{1}{\varepsilon}\right). \quad (\text{B29})$$

Proof. On the event $\{E_{J_0} - E_0 \leq c_E N_o\}$ one has $L(J_0) = \left\lceil \frac{E_{J_0} - E_0}{\Delta E_{\text{layer}}} \right\rceil \leq \left\lceil \frac{c_E N_o}{\Delta E_{\text{layer}}} \right\rceil$. Thus,

$$\Pr_\mu(E_{J_0} - E_0 \leq c_E N_o) \geq 1 - \eta, \quad (\text{B30})$$

implies Lemma 6 with chosen

$$L_\mu \leq \left\lceil \frac{c_E N_o}{\Delta E_{\text{layer}}} \right\rceil, \quad (\text{B31})$$

Substituting this into the sufficient condition Eq. (B11) from Lemma 6 yields Eq. (B28) and the stated scaling. \blacksquare

Proof of Theorems 1 & 3

Proof of Theorem 3. We now combine Lemma 5 (geometric Davis-Kahan control of ground-state drift) and Lemmas 6 and 7 to bound the total number of dissipative blocks required to follow a reaction path, and thereby overall gate complexity of this algorithm. Choose a discretization $0 = s_0 < s_1 < \dots < s_{N_H} = 1$ of the reaction coordinate. Starting from an initial warm start ρ_0 at s_0 , for each $i = 0, \dots, N_H - 1$ apply the dissipative channel at geometry s_i for t_i steps to obtain ρ_{i+1} , which is then used as a warm start for the next geometry s_{i+1} . The goal is to achieve a bounded energy error $|\text{tr}(H(1)\rho_{N_H}) - E_0(1)| \leq \epsilon_E$ for some $\epsilon_E > 0$. Choose a discretization $0 = s_0 < s_1 < \dots < s_{N_H} = 1$. Define the resolved geometric density

$$g(s) := \frac{\|\partial_s H(s)\|_2}{\Delta(s)}, \quad C_{\text{DK}} := \int_0^1 g(s) ds.$$

Choose an (approximate) equal-mass mesh,

$$\int_{s_i}^{s_{i+1}} g(s) ds \leq \frac{C_{\text{DK}}}{N_H}, \quad \forall i, \quad (\text{B32})$$

then Lemma 5 yields

$$\|P_{\leq}(s_i) - P_{\leq}(s_{i+1})\|_2 \leq \frac{C_{\text{DK}}}{N_H}. \quad (\text{B33})$$

Eq. (B33) implies a uniform overlap bound between adjacent ground states:

$$1 - |\langle E_0(s_i) | E_0(s_{i+1}) \rangle|^2 \leq \left(\frac{C_{\text{DK}}}{N_H} \right)^2 =: \varepsilon_{dR}. \quad (\text{B34})$$

For each geometry s_i define the excited population (energy-basis tail)

$$\delta_i := 1 - \langle E_0(s_i) | \rho_i | E_0(s_i) \rangle.$$

This quantity is exactly the total population mass outside the absorbing state in the Markov-chain picture of Lemma 6 (equivalently, if one measures ρ_i in the energy basis and draws an index $J \sim p$, then $\delta_i = \Pr(J \neq 0)$). It upper-bounds the energy error via

$$\text{tr}(H(s_i)\rho_i) - E_0(s_i) = \sum_{j>0} (E_j(s_i) - E_0(s_i))p_j \leq \left(\sup\{E_j(s_i) - E_0(s_i) : p_j > 0\} \right) \delta_i, \quad (\text{B35})$$

where $p_j := \langle E_j(s_i) | \rho_i | E_j(s_i) \rangle$. Under the warm-start spectral extensivity assumption $\Pr_{\mu_i}(E_{J_0}(s_i) - E_0(s_i) \leq c_E N_o) \geq 1 - \eta$ (cf. Lemma 7), we may further bound

$$\text{tr}(H(s_i)\rho_i) - E_0(s_i) \leq c_E N_o \delta_i \quad \text{except on an event of probability at most } \eta. \quad (\text{B36})$$

The geometric bound Eq. (B34) implies that even if ρ_i were perfectly cooled at s_i , when reinterpreted at s_{i+1} it acquires at most ε_{dR} additional excited weight (up to universal constants). Thus, suppressing constant factors, we may propagate the schematic recurrence

$$\delta_{i+1} \leq (\text{cooling residual at } s_i) + \varepsilon_{dR}. \quad (\text{B37})$$

Fix a target per-step cooling error parameter ε_{mix} . At each geometry s_i , Lemma 6 provides a step count t_i such that after t_i applications of the dissipative update, the remaining excited population mass is at most $\eta + \varepsilon_{\text{mix}}$, where η is the warm-start layer overflow probability

$$\Pr_{\mu_i}(L(J_0) > L_{\mu_i}) \leq \eta, \quad (\text{B38})$$

with L_{μ_i} the η -quantile layer radius at s_i . Concretely, choosing

$$t_i = \left\lceil \frac{2L_{\mu_i}}{p_{\min}} + \frac{8}{p_{\min}} \ln \frac{1}{\varepsilon_{\text{mix}}} \right\rceil \quad (\text{B39})$$

ensures

$$\delta_{i+1} \leq (\eta + \varepsilon_{\text{mix}}) + \varepsilon_{dR}. \quad (\text{B40})$$

Here p_{\min} is the one-step drift lower bound from Lemma 6.

Iterating Eq. (B40) over N_H steps gives

$$\delta_{N_H} \leq N_H(\eta + \varepsilon_{\text{mix}}) + N_H \varepsilon_{dR} = N_H(\eta + \varepsilon_{\text{mix}}) + \frac{C_{\text{DK}}^2}{N_H}.$$

Combining with Eq. (B36) yields, up to the same exceptional event of probability at most η ,

$$|\text{tr}(H(1)\rho_{N_H}) - E_0(1)| \leq c_E N_o \left(N_H(\eta + \varepsilon_{\text{mix}}) + \frac{C_{\text{DK}}^2}{N_H} \right).$$

Accordingly, one convenient choice is

$$N_H = \Theta\left(\frac{C_{\text{DK}}^2}{\varepsilon_E}\right), \quad \varepsilon_{\text{mix}} = \Theta\left(\frac{\varepsilon_E}{N_H}\right), \quad \eta = \Theta\left(\frac{\varepsilon_E}{N_H}\right), \quad (\text{B41})$$

absorbing the extensive prefactor $c_E N_o$ and universal constants into the $\Theta(\cdot)$ choices (or, equivalently, interpreting ε_E as an accuracy per orbital up to constants).

Hence, the total number of dissipative steps (i.e., applications of the dissipative update) is bounded by

$$\sum_{i=0}^{N_H-1} t_i = O\left(\frac{N_H}{p_{\min}} \left(\bar{L}_\mu + \ln \frac{N_H}{\epsilon_E}\right)\right), \quad (\text{B42})$$

where $\bar{L}_\mu := \max_i L_{\mu_i}$. Substituting $N_H = \Theta(C_{\text{DK}}^2/\epsilon_E)$ yields the compact end-to-end scaling

$$\sum_{i=0}^{N_H-1} t_i = O\left(\frac{C_{\text{DK}}^2 \bar{L}_\mu}{p_{\min} \epsilon_E}\right). \quad (\text{B43})$$

When warm-start spectral extensivity condition holds uniformly we have that $\bar{L}_\mu = O(N_o)$ (Lemma 7), and $p_{\min} = \Theta(1)$. Simulating dissipative dynamics for evolution time t on quantum computers requires $\tilde{O}(t)$ logical quantum resources [53]. Therefore, the total algorithmic runtime (gate) complexity is

$$\tilde{O}\left(\frac{C_{\text{DK}}^2 N_o}{\epsilon_E}\right). \quad (\text{B44})$$

■

For a Hamiltonian along the reaction path as a sum of M terms defined in Eq. Eq. (B25) with each term varying smoothly along the path defined by the Lipschitz constant L_h in Eq. Eq. (B26), if the derivative exists, then $\|\partial_s h_\ell(s)\| \leq L_h$. It follows that $\|\partial_s H(s)\| \leq ML_h$. Now, we have that

$$C_{\text{DK}} = \int_0^1 \frac{\|\partial_s H(s)\|_2}{\Delta(s)} ds \leq \int_0^1 \frac{ML_h}{\Delta_{\min}} ds = O(N_o/\Delta_{\min}). \quad (\text{B45})$$

Therefore, we arrive at an asymptotic runtime (gate) complexity that is *cubic* in system size N_o^3 ,

$$\tilde{O}\left(\frac{\|H\|}{\Delta_{\min}^3} \cdot \frac{1}{\epsilon_E} \cdot N_o^3\right), \quad (\text{B46})$$

where the additional factor of $\|H\|/\Delta_{\min}$ arises from the cost of implementing filtered jump operators, as shown in Section C.

Appendix C: Digital Adiabatic Simulation versus Dissipative Evolution

This section compares (i) large-step digital adiabatic simulation (DAS) along the same nonlinear reaction path $\{H(s)\}_{s \in [0,1]}$ and (ii) our *dissipative continuation* method that transports a warm start between adjacent geometries and re-cools at each step. The key point is that both approaches exploit the smoothness of the reaction path, but they pay for it in different places: DAS pays heavily for small gaps through adiabatic constraints, whereas dissipative continuation pays through the number of path points N_H (controlled by C_{DK}) and the per-step mixing time (controlled by the uniform drift parameter p_{\min} and the target failure probability).

1. Setup and shared parameters

Fix consecutive grid points $s_i < s_{i+1}$ and define the local interval Hamiltonian norm

$$\|H\| := \max_{s \in [s_i, s_{i+1}]} \|H(s)\|_2, \quad \Delta_{\min} := \min_{s \in [s_i, s_{i+1}]} \Delta(s),$$

where $\Delta(s)$ is the ground-state gap at geometry s . Throughout, N_o denotes the number of *spatial* orbitals. We compare *per-segment* cost to transport from s_i to s_{i+1} and then multiply by the number of segments N_H required to reach $s = 1$.

Independent of the transport mechanism, our path-following regime requires a grid fine enough that successive ground states retain overlap. Lemma 5 implies that an “equal-mass” mesh in the DK density $g(s) := \|\partial_s H(s)\|_2/\Delta(s)$ yields a per-step overlap loss $\varepsilon_{dR} = \Theta((C_{\text{DK}}/N_H)^2)$, hence choosing

$$N_H = \Theta\left(\frac{C_{\text{DK}}^2}{\epsilon_E}\right) \quad (\text{C1})$$

is sufficient to keep discretization-induced energy error under control (up to constant/extensive factors; see Section B 2). When $\|\partial_s H(s)\|_2 = O(N_o)$ and $\Delta(s) \geq \Delta_{\min}$ along the path, one typically has $C_{\text{DK}} = O(N_o/\Delta_{\min})$, giving $N_H = \tilde{O}(N_o^2/(\Delta_{\min}^2 \epsilon_E))$.

2. Per-segment cost of dissipative continuation

Our algorithm uses a short-time dissipative primitive (a filtered-jump Lindbladian step) at geometry s_{i+1} initialized by a warm start transported from s_i (e.g., via Procrustes-aligned orbital rotations plus state reuse). Let ϵ denote the target failure probability for cooling at that segment. Under the conditions of Lemmas 6 and 7 provide a per-segment mixing time

$$t_{\text{mix}} = O\left(N_o + \ln \frac{1}{\epsilon}\right), \quad (\text{C2})$$

for fixed layer size ΔE_{layer} and drift parameter p_{\min} .

Each dissipative step is implemented using filtered jump operators, whose circuit depth is governed by the filter time support needed to achieve leakage ϵ_{leak} (Theorem 2). Up to polylogarithmic overheads from Lindbladian simulation, the gate cost per dissipative step scales as the number of distinct real-time evolutions $e^{\pm iHt}$ required by the filter:

$$\text{Cost}_{\text{step}} = \tilde{O}\left(S(\epsilon_{\text{leak}}) \cdot \text{Cost}(U_H)\right), \quad (\text{C3})$$

where U_H is the chosen block encoding / time-evolution primitive. Using the two filter families:

$$S_{\text{SW}}(\epsilon_{\text{leak}}) = O\left(\frac{\|H\|}{\Delta_{\min}} \cdot \frac{1}{\epsilon_{\text{leak}}}\right), \quad (\text{C4})$$

$$S_{\text{G}}(\epsilon_{\text{leak}}) = O\left(\frac{\|H\|}{\Delta_{\min}} \cdot [\log(1/\epsilon_{\text{leak}})]^\alpha\right), \quad \alpha < 1. \quad (\text{C5})$$

Thus, the *per-segment* gate complexity of dissipative continuation is

$$G_{\text{diss}}^{(\cdot)} = \tilde{O}\left(\frac{\|H\|}{\Delta_{\min}} \cdot F(\epsilon_{\text{leak}}) \cdot \left(N_o + \ln \frac{1}{\epsilon}\right)\right), \quad (\text{C6})$$

where $F(\epsilon_{\text{leak}}) = 1/\epsilon_{\text{leak}}$ for the square-wave (Fourier) filter and $F(\epsilon_{\text{leak}}) = [\log(1/\epsilon_{\text{leak}})]^\alpha$ for the Gevrey filter.

Dissipative continuation separates two ‘‘hardness knobs’’: (i) spectral hardness enters *linearly* as $\|H\|/\Delta_{\min}$ through filtering, while (ii) system-size hardness enters through the *mixing time* $O(N_o)$ (from extensivity) and through the *grid size* N_H (from C_{DK}). This is qualitatively different from DAS, where Δ_{\min} controls the required adiabatic runtime more directly.

3. Per-segment cost of large-step digital adiabatic simulation

Large-step DAS aims to prepare $|E_0(s_{i+1})\rangle$ by simulating an adiabatic interpolation on $s \in [s_i, s_{i+1}]$ with a small number of discrete steps, using a large step size $h = \Theta(1/(\|H(s_i)\| + \|H(s_{i+1})\|))$ and an improved analysis of adiabatic error [2]. Abstracting away polylog factors and implementation details, the dominant dependence is that adiabatic state-preparation cost grows rapidly as the gap decreases. In the scaling form used in the main text, the *per-segment* DAS gate complexity is

$$G_{\text{DAS}} = \tilde{O}\left(\frac{\|H\|^3}{\Delta_{\min}^3} \cdot \frac{1}{\epsilon} \cdot \text{poly}(N_o)\right), \quad (\text{C7})$$

where ϵ is the target adiabatic error/failure parameter, and $\text{poly}(N_o)$ accounts for the cost of simulating $e^{-ihH(s)}$ and implementing the schedule. (More refined versions would track the dependence on $\|\partial_s H\|$ and higher derivatives, but Eq. (C7) captures the key spectral-gap sensitivity relevant to transition-state regimes.)

DAS pays a *polynomially higher* price in $1/\Delta_{\min}$ per segment than dissipative continuation. This distinction is most pronounced near transition states, where small gaps are common and where our method is designed to reuse a warm start so that the dissipative dynamics rapidly returns to the instantaneous ground state.

4. End-to-end costs along the full reaction path

Multiplying by the number of segments N_H in Eq. (C1), we obtain the end-to-end scaling. For DAS:

$$N_H \cdot G_{\text{DAS}} = \tilde{O}\left(\frac{C_{\text{DK}}^2}{\epsilon_E} \cdot \frac{\|H\|^3}{\Delta_{\text{min}}^3} \cdot \frac{1}{\epsilon} \cdot \text{poly}(N_o)\right). \quad (\text{C8})$$

For dissipative continuation:

$$N_H \cdot G_{\text{diss}}^{(\cdot)} = \tilde{O}\left(\frac{C_{\text{DK}}^2}{\epsilon_E} \cdot \frac{\|H\|}{\Delta_{\text{min}}} \cdot \text{F}(\epsilon_{\text{leak}}) \cdot \left(N_o + \ln \frac{1}{\epsilon}\right)\right). \quad (\text{C9})$$

If one further uses the coarse bound $C_{\text{DK}} = O(N_o/\Delta_{\text{min}})$, then

$$N_H \cdot G_{\text{DAS}} = \tilde{O}\left(\frac{\|H\|^3}{\Delta_{\text{min}}^5} \cdot \frac{1}{\epsilon_E} \cdot \frac{1}{\epsilon} \cdot \text{poly}(N_o) \cdot N_o^2\right), \quad (\text{C10})$$

$$N_H \cdot G_{\text{diss}}^{(\cdot)} = \tilde{O}\left(\frac{\|H\|}{\Delta_{\text{min}}^3} \cdot \frac{1}{\epsilon_E} \cdot \text{F}(\epsilon_{\text{leak}}) \cdot \left(N_o + \ln \frac{1}{\epsilon}\right) \cdot N_o^2\right), \quad (\text{C11})$$

which is consistent with the heuristic summaries already stated in the paper, while making explicit where the factors arise (grid size vs. per-segment transport).

Appendix D: Phase Randomization and Dynamic Cooling versus Dissipative Evolution

Phase randomization (PR) [31] and dynamic cooling (DC) [35] provide unitary-centric alternatives to using an explicit Lindbladian cooling primitive. Both are useful comparators in the reaction-path setting because they exploit the same structural feature as dissipative continuation: a warm start at s_i is already concentrated in the low-energy subspace of $H(s_{i+1})$ when the path is discretized finely enough. The purpose of this section is to justify the gate-complexity scalings used in Table I, highlighting how the dependence on $\|H\|$, Δ_{min} , and N_o arises from (i) Hamiltonian simulation costs, (ii) the time scale required to resolve gaps, and (iii) the number of randomization / cooling iterations required at each path point.

1. Shared cost model and path discretization

We adopt the standard Hamiltonian-simulation cost model used throughout the paper: implementing time evolution for time t under an interval Hamiltonian $H(s)$ has gate complexity

$$\text{Cost}\left(e^{-iH(s)t}\right) = \tilde{O}(t\|H\|\text{poly}(N_o)), \quad (\text{D1})$$

where $\|H\| := \max_{s \in [s_i, s_{i+1}]} \|H(s)\|_2$ and $\text{poly}(N_o)$ absorbs block-encoding, term-selection, basis-change, and other method-dependent overheads.

Along the reaction path, we discretize $s \in [0, 1]$ into N_H geometries so that the instantaneous ground-state projector does not rotate too quickly between adjacent points. As in Section C, we use a Davis–Kahan (DK) adapted mesh controlled by the DK length C_{DK} , which yields

$$N_H = \Theta\left(\frac{C_{\text{DK}}^2}{\epsilon_E}\right). \quad (\text{D2})$$

In chemistry regimes where $\|\partial_s H(s)\|_2 = O(N_o)$ and $\Delta(s) \geq \Delta_{\text{min}}$ along the relevant portion of the path, we use the coarse estimate

$$C_{\text{DK}} = O\left(\frac{N_o}{\Delta_{\text{min}}}\right), \quad (\text{D3})$$

which is the substitution used in the caption of Table I.

2. Phase randomization

At a fixed geometry s , PR applies $H(s)$ for a random time and averages over that randomness, yielding a dephasing channel in the eigenbasis of $H(s)$:

$$\mathcal{R}_s(\rho) = \mathbb{E}_{t \sim \mu} \left[e^{-iH(s)t} \rho e^{+iH(s)t} \right]. \quad (\text{D4})$$

In the eigenbasis $\{|E_k(s)\rangle\}$, off-diagonal terms obey $\rho_{jk} \mapsto \rho_{jk} \hat{\mu}(E_j - E_k)$, hence choosing μ with $|\hat{\mu}(\omega)| \ll 1$ for $|\omega| \gtrsim \Delta_{\min}$ suppresses coherences between eigenstates separated by at least the minimum gap.

The PR traversal algorithm [31] stabilizes transport along the discretized path by using this dephasing as an approximate projective step. The relevant cost contributions are: (i) the cost per randomized evolution, (ii) the characteristic time scale required to resolve the gap, and (iii) the number of PR attempts (or equivalently, the repetition overhead) needed to achieve an overall success probability p_{succ} .

The gap-resolution requirement sets the evolution-time scale. Any distribution μ that significantly damps frequencies $|\omega| \gtrsim \Delta_{\min}$ must have time spread on the order of

$$t_{\text{PR}} = \Theta\left(\frac{1}{\Delta_{\min}}\right) \quad (\text{D5})$$

(up to polylogarithmic factors depending on the chosen μ). Substituting $t = t_{\text{PR}}$ into the Hamiltonian-simulation model in Eq. (D1) gives the per-attempt cost

$$\text{Cost}_{\text{attempt}} = \tilde{O}\left(\frac{\|H\|}{\Delta_{\min}} \cdot \text{poly}(N_o)\right). \quad (\text{D6})$$

The PR traversal is probabilistic: it returns the correct transported state with probability p_{succ} , yielding a repetition factor $1/(1 - p_{\text{succ}})$ at the level of expected number of attempts. The remaining dependence on Δ_{\min} enters through the path discretization. Transport to the target geometry requires N_H PR-stabilized steps, and under the DK mesh choice of Eq. (D2) together with the coarse estimate from Eq. (D3), one has

$$N_H = \tilde{O}\left(\frac{N_o^2}{\Delta_{\min}^2} \cdot \frac{1}{\epsilon_E}\right),$$

so multiplying the per-step attempt cost from Eq. (D6) by N_H and the repetition factor $1/(1 - p_{\text{succ}})$ yields

$$n_G^{\text{PR}} = \tilde{O}\left(\frac{\|H\|}{\Delta_{\min}} \cdot \frac{N_o^2}{\Delta_{\min}^2} \cdot \frac{1}{\epsilon_E} \cdot \frac{1}{1 - p_{\text{succ}}} \cdot \text{poly}(N_o)\right) = \tilde{O}\left(\frac{\|H\|}{\Delta_{\min}^3} \cdot \frac{1}{\epsilon_E} \cdot \frac{1}{1 - p_{\text{succ}}} \cdot \text{poly}(N_o)\right), \quad (\text{D7})$$

which matches the PR row of Table I. The role of the bound $C_{\text{DK}} = O(N_o/\Delta_{\min})$ is to convert the DK-adapted discretization into the explicit Δ_{\min}^{-2} factor in N_H , which then combines with the Δ_{\min}^{-1} time-resolution factor in Eq. (D6).

3. Dynamic cooling

Dynamic cooling alternates a dephasing/phase-mixing step with an explicitly energy-selective unitary procedure, implemented using QSP/QSVT transformations interleaved with a weak perturbation that induces transitions biased toward lower energies [35]. The scaling used in Table I can be recovered by combining (i) the same Hamiltonian-simulation cost model of Eq. (D1), (ii) the same DK-based discretization $N_H = \Theta(C_{\text{DK}}^2/\epsilon_E)$, and (iii) the DC iteration complexity at each geometry. In the DC analysis, the number of calls to the underlying e^{-iHt} primitive at a fixed geometry is governed by an effective dimension parameter d that controls the schedule/energy-resolution regime of the procedure. In the regime relevant to reaction-path electronic-structure instances, one takes

$$d = O(N_o), \quad (\text{D8})$$

and the number of Hamiltonian-evolution calls per geometry is

$$N_{\text{calls}}^{\text{DC}} = \tilde{O}\left(d^{3/2}\right) = \tilde{O}\left(N_o^{3/2}\right), \quad (\text{D9})$$

as stated in your discussion. Each call is an evolution for a time on the order of $1/\Delta_{\min}$ to resolve the relevant spectral features (analogous to Eq. (D5)), so the per-geometry DC gate complexity is

$$\tilde{O}\left(N_{\text{calls}}^{\text{DC}} \cdot \frac{\|H\|}{\Delta_{\min}} \cdot \text{poly}(N_o)\right) = \tilde{O}\left(\frac{\|H\|}{\Delta_{\min}} \cdot N_o^{3/2} \cdot \text{poly}(N_o)\right). \quad (\text{D10})$$

Transporting along the path multiplies this cost by N_H . Using Eq. (D2) and the coarse estimate Eq. (D3) gives $N_H = \tilde{O}(N_o^2/(\Delta_{\min}^2 \epsilon_E))$, hence

$$n_G^{\text{DC}} = \tilde{O}\left(\frac{\|H\|}{\Delta_{\min}} \cdot \frac{N_o^2}{\Delta_{\min}^2} \cdot \frac{1}{\epsilon_E} \cdot N_o^{3/2} \cdot \text{poly}(N_o)\right) = \tilde{O}\left(\frac{\|H\|}{\Delta_{\min}^3} \cdot \frac{1}{\epsilon_E} \cdot \text{poly}(N_o)\right), \quad (\text{D11})$$

where the $N_o^{3/2}$ factor is absorbed into $\text{poly}(N_o)$ in the table presentation. This recovers the DC row in Table I while making explicit the internal accounting used in your text: the dominant system-size penalty in DC arises because the primitive $e^{\pm iH}$ is called $\tilde{O}(N_o^{3/2})$ times per geometry, in addition to the N_H geometries required by the DK discretization.

Appendix E: Ground-state overlap from occupied-space principal angles

Along a nuclear reaction path, one typically solves an independent Hartree-Fock (or related mean-field) problem at each geometry. This procedure optimizes the electronic energy locally at each point $\mathbf{R}(s_i)$, but it does not enforce continuity of the orbital representation between successive geometries. In particular, Hartree-Fock determines only the occupied subspace at a given geometry, not a unique choice of orbitals spanning that subspace: any unitary rotation among occupied orbitals leaves the Slater determinant (and the Hartree-Fock energy) unchanged, so the numerical orbitals are defined only up to an arbitrary gauge within the occupied space. In order to obtain the maximum overlap between mean-field states between successive geometries $\mathbf{R}(s_k)$ and $\mathbf{R}(s_{k+1})$, we therefore solve for the unitary rotation that maximizes orbital overlap. This motivates our Procrustes alignment procedure, which fixes a consistent gauge along the reaction path. After alignment, the resulting family of Hamiltonians and ground states exhibits the smooth drift behavior required by Theorem 1.

The Procrustes alignment algorithm utilizes Proposition 1 to optimize orbital gauges by computing the singular value decomposition (SVD) of $M_{\text{occ}}^{(k)} = U_{\text{occ}}^{(k)} \Sigma_{\text{occ}}^{(k)} V_{\text{occ}}^{(k)\dagger}$. From the singular values $\{\sigma_i^{(k)}\}$, we can measure the overlaps Eq. (E5) are directly. The Procrustes alignment algorithm starts at the end of the reaction path $\mathbf{R}(s_{N_H} = 1)$ and aligns the orbitals of the previous geometry $\mathbf{R}(s_{N_H-1})$ to the products' orbitals. The process is continued for each geometry until the reactant geometry is reached $\mathbf{R}(s_1 = 0)$. At each step of this process, we solve the Procrustes problem

$$R^{(k)} := \arg \max_R \text{Re}\{\text{Tr}(R^\dagger M_{\text{occ}}^{(k)})\} = U_{\text{occ}}^{(k+1)} (V_{\text{occ}}^{(k+1)})^\dagger. \quad (\text{E1})$$

Then, the occupied molecular orbital coefficient matrix for geometry $\mathbf{R}(s_k)$ is rotated by $R^{(k)}$, $C_k^{\text{occ}} \leftarrow C_k^{\text{occ}} R^{(k)}$. The matrix $M_{\text{occ}}^{(k)}$ is given by

$$M_{\text{occ}}^{(k)} = (C_{k+1}^{\text{occ}})^\dagger S_{k,k+1} C_k^{\text{occ}}. \quad (\text{E2})$$

where the *AO cross-overlap matrix* $S_{k,k+1} \in \mathbb{C}^{N_k \times N_{k+1}}$ is defined entry-wise by

$$(S_{k,k+1})_{\mu\nu} := \langle \chi_\mu^{(k)} | \chi_\nu^{(k+1)} \rangle = \int_{\mathbb{R}^3} d\mathbf{r} \chi_\mu^{(k)}(\mathbf{r})^* \chi_\nu^{(k+1)}(\mathbf{r}), \quad (\text{E3})$$

where $\{\chi_\mu^{(k)}(\mathbf{r})\}_{\mu=1}^{N_k}$ and $\{\chi_\nu^{(k+1)}(\mathbf{r})\}_{\nu=1}^{N_{k+1}}$ denote the (possibly geometry-dependent) atomic-orbital (AO) basis functions associated with $\mathbf{R}(s_k)$ and $\mathbf{R}(s_{k+1})$, respectively.

Proposition 1 (Ground-state overlap from occupied-space principal angles). *Consider $\mathbf{R}(s_k)$ and $\mathbf{R}(s_{k+1})$, two consecutive geometries along the reaction path. Define the atomic orbital (AO) cross-overlap matrix $S_{k,k+1}$, and let $\{\chi_\mu^{(k)}(\mathbf{r})\}_{\mu=1}^{N_k}$ and $\{\chi_\nu^{(k+1)}(\mathbf{r})\}_{\nu=1}^{N_{k+1}}$ denote the (possibly geometry-dependent) atomic-orbital (AO) basis functions. Let the AO cross-overlap matrix be denoted $S_{k,k+1} \in \mathbb{C}^{N_k \times N_{k+1}}$. Let $C_k^{\text{occ}}, C_{k+1}^{\text{occ}} \in \mathbb{C}^{n_{\text{AO}} \times N_{\text{occ}}}$ collect orthonormal occupied molecular orbitals at $\mathbf{R}(s_k)$ and $\mathbf{R}(s_{k+1})$, and let*

$$M_{\text{occ}}^{(k)} = (C_{k+1}^{\text{occ}})^\dagger S_{k,k+1} C_k^{\text{occ}}. \quad (\text{E4})$$

Denote the singular values of $M_{\text{occ}}^{(k)}$ by $\sigma_i^{(k)} = \cos \theta_i^{(k)}$ with principal angles $\theta_i^{(k)} \in [0, \pi/2]$, $i = 1, \dots, N_{\text{occ}}$. Let $|\Phi_0^{(k)}\rangle$ and $|\Phi_0^{(k+1)}\rangle$ be the corresponding closed-shell single-determinant Hartree-Fock states. Then the squared overlap between these two single-determinant states is

$$|\langle \Phi_0^{(k+1)} | \Phi_0^{(k)} \rangle|^2 = \prod_{i=1}^{N_{\text{occ}}} \cos^2 \theta_i^{(k)}. \quad (\text{E5})$$

Proof. For brevity, we suppress spin and treat $\{\phi_p^{(k)}\}_{p=1}^{N_{\text{occ}}}$ and $\{\phi_p^{(k+1)}\}_{p=1}^{N_{\text{occ}}}$ as orthonormal one-particle orbitals spanning the occupied spaces at geometries $\mathbf{R}(s_k)$ and $\mathbf{R}(s_{k+1})$, respectively. The generalization to closed-shell spin-orbital determinants is straightforward and only changes notation.

Let $|\Phi_0^{(k)}\rangle$ and $|\Phi_0^{(k+1)}\rangle$ be the N_{occ} -electron Slater determinants built from these orbitals. In first-quantized notation they are

$$|\Phi_0^{(k)}\rangle = \frac{1}{\sqrt{N_{\text{occ}}!}} \phi_1^{(k)} \wedge \dots \wedge \phi_{N_{\text{occ}}}^{(k)},$$

$$|\Phi_0^{(k+1)}\rangle = \frac{1}{\sqrt{N_{\text{occ}}!}} \phi_1^{(k+1)} \wedge \dots \wedge \phi_{N_{\text{occ}}}^{(k+1)},$$

where \wedge denotes the antisymmetrized wedge product. A standard identity for wedge products (equivalently, the Slater–Condon rule) states that for two sets of one-particle states $\{\psi_i\}_{i=1}^N$ and $\{\varphi_j\}_{j=1}^N$,

$$\langle \psi_1 \wedge \dots \wedge \psi_N | \varphi_1 \wedge \dots \wedge \varphi_N \rangle = \det G, \quad G_{ij} := \langle \psi_i | \varphi_j \rangle. \quad (\text{E6})$$

Applying Eq. (E6) with $\psi_i = \phi_i^{(k+1)}$ and $\varphi_j = \phi_j^{(k)}$ gives

$$\langle \Phi_0^{(k+1)} | \Phi_0^{(k)} \rangle = \det M_{\text{occ}}^{(k)}, \quad M_{\text{occ},ij}^{(k)} := \langle \phi_i^{(k+1)} | \phi_j^{(k)} \rangle. \quad (\text{E7})$$

In the AO basis, the occupied orbitals are $\phi_j^{(k)} = \sum_{\mu} (C_k^{\text{occ}})_{\mu j} \chi_{\mu}^{(k)}$, $\phi_i^{(k+1)} = \sum_{\nu} (C_{k+1}^{\text{occ}})_{\nu i} \chi_{\nu}^{(k+1)}$, and the AO cross overlap is $S_{k,k+1,\nu\mu} = \langle \chi_{\nu}^{(k+1)} | \chi_{\mu}^{(k)} \rangle$. Thus

$$M_{\text{occ}}^{(k)} = (C_{k+1}^{\text{occ}})^{\dagger} S_{k,k+1} C_k^{\text{occ}},$$

as stated in the proposition.

Let the singular value decomposition of $M_{\text{occ}}^{(k)}$ be

$$M_{\text{occ}}^{(k)} = U_{\text{occ}}^{(k)} \Sigma_{\text{occ}}^{(k)} V_{\text{occ}}^{(k)\dagger}, \quad \Sigma_{\text{occ}}^{(k)} = \text{diag}(\sigma_1^{(k)}, \dots, \sigma_{N_{\text{occ}}}^{(k)}), \quad (\text{E8})$$

with singular values $\sigma_i^{(k)} \in [0, 1]$. By definition of principal angles between the occupied subspaces $\mathcal{W}_k = \text{span}\{\phi_j^{(k)}\}$ and $\mathcal{W}_{k+1} = \text{span}\{\phi_i^{(k+1)}\}$, we can write

$$\sigma_i^{(k)} = \cos \theta_i^{(k)}, \quad \theta_i^{(k)} \in [0, \pi/2], \quad i = 1, \dots, N_{\text{occ}}.$$

From Eq. (E7) we have

$$|\langle \Phi_0^{(k+1)} | \Phi_0^{(k)} \rangle|^2 = |\det M_{\text{occ}}^{(k)}|^2 = \det(M_{\text{occ}}^{(k)\dagger} M_{\text{occ}}^{(k)}).$$

But $M_{\text{occ}}^{(k)\dagger} M_{\text{occ}}^{(k)}$ is unitarily similar to $\Sigma_{\text{occ}}^{(k)2}$ and thus has eigenvalues $\{(\sigma_i^{(k)})^2\}_{i=1}^{N_{\text{occ}}}$. Therefore

$$|\langle \Phi_0^{(k+1)} | \Phi_0^{(k)} \rangle|^2 = \prod_{i=1}^{N_{\text{occ}}} (\sigma_i^{(k)})^2 = \prod_{i=1}^{N_{\text{occ}}} \cos^2 \theta_i^{(k)},$$

which is exactly Eq. (E5). ■

Appendix F: Theorem 2 (Time support scaling for Gevrey vs. periodic square-wave filters)

Theorem 4 (Time support scaling for Gevrey vs. periodic square-wave filters). *Let $H = \sum_j E_j |E_j\rangle\langle E_j|$ have a nondegenerate ground state $|E_0\rangle$ and gap $\Delta := \min_{j>0}(E_j - E_0) > 0$. Let A be bounded with $\|A\| \leq 1$. Fix a target leakage $0 < \varepsilon_{\text{leak}} < 1$.*

Then there exist two families of filtered jump operators $K_{\varepsilon_{\text{leak}}}^G$ and $K_{\varepsilon_{\text{leak}}}^{\text{SW}}$ such that

$$\|K_{\varepsilon_{\text{leak}}} |E_0\rangle\| \leq \varepsilon_{\text{leak}}.$$

Moreover, writing $\omega_{\text{max}} := \max_j(E_j - E_0) \leq 2\|H\|$, the required time support (and hence, up to constant discretization factors, the number of distinct real-time evolution calls) can be chosen as:

- **Gevrey filter.** *There exists a Gevrey-class filter with essentially compact time support satisfying*

$$S_G(\varepsilon_{\text{leak}}) = O\left(\frac{\|H\|}{\Delta} [\log(1/\varepsilon_{\text{leak}})]^\alpha\right), \quad \alpha > 1,$$

with α depending only on the Gevrey class [20].

- **Periodic square-wave Fourier filter.** *There exists a truncated periodic square-wave (Dirichlet) filter with time support*

$$S_{\text{SW}}(\varepsilon_{\text{leak}}) = O\left(\frac{\|H\|}{\Delta} \frac{1}{\varepsilon_{\text{leak}}}\right),$$

up to bounded oscillatory factors in the leakage.

Finally, if the filter is implemented by sampling times on a uniform grid with step size $\Delta t = \Theta(1/\|H\|)$, then the number of distinct calls of the form $e^{iHt}(\cdot)e^{-iHt}$ is $\Theta(S(\varepsilon_{\text{leak}}))$.

Proof. Define, for any integrable (or truncated / discretized) kernel f ,

$$K_f := \int_{\mathbb{R}} f(t) e^{itH} A e^{-itH} dt. \tag{F1}$$

In the eigenbasis of H ,

$$e^{itH} A e^{-itH} = \sum_{j,k} e^{it(E_j - E_k)} A_{jk} |E_j\rangle\langle E_k|, \quad A_{jk} := \langle E_j | A | E_k \rangle,$$

so

$$K_f = \sum_{j,k} \hat{f}(E_j - E_k) A_{jk} |E_j\rangle\langle E_k|, \tag{F2}$$

where $\hat{f}(\omega) = \int_{\mathbb{R}} f(t) e^{it\omega} dt$ (same Fourier convention as in the square-wave derivation). Applying to $|E_0\rangle$ gives

$$K_f |E_0\rangle = \sum_{j>0} \hat{f}(E_j - E_0) A_{j0} |E_j\rangle.$$

Hence

$$\|K_f |E_0\rangle\| \leq \left(\sup_{\omega \geq \Delta} |\hat{f}(\omega)| \right) \|A |E_0\rangle\| \leq \sup_{\omega \geq \Delta} |\hat{f}(\omega)|. \tag{F3}$$

Thus it suffices to construct \hat{f} with $\sup_{\omega \geq \Delta} |\hat{f}(\omega)| \leq \varepsilon_{\text{leak}}$.

Let $\text{Si}(x) = \int_0^x \frac{\sin u}{u} du$. For $x > 0$,

$$\frac{\pi}{2} - \text{Si}(x) = \int_x^\infty \frac{\sin u}{u} du = \frac{\cos x}{x} - \int_x^\infty \frac{\cos u}{u^2} du,$$

so

$$\left| \frac{\pi}{2} - \text{Si}(x) \right| \leq \frac{1}{x} + \int_x^\infty \frac{1}{u^2} du = \frac{2}{x}. \quad (\text{F4})$$

For the one-sided step $\widehat{f}(\omega) = \mathbf{1}_{\{\omega < 0\}}$, its inverse transform (in the unit-energy convention) is the Hilbert kernel $f(t) = \frac{1}{2}\delta(t) - \frac{i}{2\pi}\text{PV}(1/t)$, where PV denotes the Cauchy principal value. Rectangular truncation $f_T(t) = \frac{1}{2}\delta(t) - \frac{i}{2\pi}\text{PV}(1/t)\mathbf{1}_{\{|t| \leq T\}}$ yields the closed form

$$\widehat{f}_T(\omega) = \frac{1}{2} - \frac{1}{\pi}\text{Si}(\omega T). \quad (\text{F5})$$

For $\omega > 0$ (the upward Bohr-frequency side relevant to leakage from the ground state), combine Eq. (F4) with Eq. (F5) to get the uniform bound

$$|\widehat{f}_T(\omega)| = \frac{1}{\pi} \left| \frac{\pi}{2} - \text{Si}(\omega T) \right| \leq \frac{2}{\pi\omega T}. \quad (\text{F6})$$

Therefore, for a gap margin $\Delta > 0$,

$$\sup_{\omega \geq \Delta} |\widehat{f}_T(\omega)| \leq \frac{2}{\pi\Delta T}. \quad (\text{F7})$$

(The asymptotic refinement $\widehat{f}_T(\omega) = \frac{\cos(\omega T)}{\pi\omega T} + O((\omega T)^{-2})$ explains the bounded oscillatory factor; Eq. (F7) is the clean envelope.) Choosing $T = \Theta(1/\Delta\varepsilon_{\text{leak}})$ makes the RHS $\leq \varepsilon_{\text{leak}}$, and then Eq. (F3) gives $\|K_f|E_0\rangle\| \leq \varepsilon_{\text{leak}}$.

Now implement the filter by periodizing in frequency with period Ω and truncating to N_ω Fourier modes (Dirichlet partial sum). Choose

$$\Omega \geq 4\|H\| \quad \Rightarrow \quad \omega_{\text{max}} \leq 2\|H\| < \Omega/2, \quad (\text{F8})$$

so that all Bohr frequencies $E_j - E_k$ lie strictly inside the principal interval $(-\Omega/2, \Omega/2)$ (no wrap-around/aliasing in the relevant band). Let $\delta t := 2\pi/\Omega$ and

$$T_{N_\omega} := \left(N_\omega + \frac{1}{2}\right)\delta t.$$

As in the derivation, the Dirichlet kernel rescales to the sinc kernel away from $\omega = 0$, so the truncated periodic square-wave filter converges (for fixed ω and, on any band $|\omega| \geq \Delta$, uniformly up to constants) to the rectangularly truncated filter with horizon T_{N_ω} . In particular, the same envelope bound applies:

$$\sup_{\omega \geq \Delta} |\widehat{f}_{N_\omega}^{(\Omega)}(\omega)| \leq \frac{1}{\Delta T_{N_\omega}}. \quad (\text{F9})$$

Thus it suffices to choose $T_{N_\omega} = \Theta\left(\frac{1}{\Delta\varepsilon_{\text{leak}}}\right)$. Finally, the implementation uses time samples $t_n = n\Delta t$ for $|n| \leq N_\omega$, so the number of distinct real-time evolution calls is $2N_\omega + 1 = \Theta(N_\omega)$, and the number of modes is bounded above and below by

$$N_\omega = \Theta\left(\frac{T_{N_\omega}}{\Delta t}\right) = \Theta(\Omega T_{N_\omega}) = \Theta\left(\frac{\|H\|}{\Delta} \frac{1}{\varepsilon_{\text{leak}}}\right),$$

where we used $\Omega = \Theta(\|H\|)$ as in Eq. (F8). This proves the stated S_{SW} scaling.

The Gevrey part is an existence statement: [20] constructs Gevrey-class filters that approximate the one-sided step outside a spectral margin while keeping the time-domain kernel essentially supported on a window of length $O\left(\frac{\|H\|}{\Delta} [\log(1/\varepsilon_{\text{leak}})]^\alpha\right)$. Applying the same reduction Eq. (F3) yields the leakage guarantee. ■

Appendix G: Reducing the Cost of Simulating Dissipative Dynamics via qDRIFT-inspired Jump Sampling

It is costly to implement the total Lindblad generator $\mathcal{L} = \sum_a \mathcal{L}_a$ at once as this requires a cost at least as much as implementing the first order product formula $\prod_a \exp(\tau \mathcal{L}_a)$. Therefore, we simulate dissipative evolution generated by a sum of Lindblad terms by random sampling one term per short time step. Concretely, we write

$$\overline{\mathcal{L}} = \sum_{a \in \mathcal{A}} \mu_a \mathcal{L}_a, \quad \sum_{a \in \mathcal{A}} \mu_a = 1,$$

and define the single-step randomized channel

$$\mathcal{E}_\tau := \mathbb{E}_{a \sim \mu} [e^{\tau \mathcal{L}_a}] = \sum_{a \in \mathcal{A}} \mu_a e^{\tau \mathcal{L}_a}. \quad (\text{G1})$$

This randomized splitting is the open-system analogue of the qDRIFT protocol for Hamiltonian simulation [69]. Note that by a Taylor expansion,

$$\mathcal{E}_\tau = \mathbb{I} + \tau \bar{\mathcal{L}} + O(\tau^2),$$

so \mathcal{E}_τ matches $e^{\tau \bar{\mathcal{L}}}$ to first order. For total evolution time t we take N_T steps with $\tau = t/N_T$ and approximate

$$e^{t \bar{\mathcal{L}}} \approx (\mathcal{E}_{t/N_T})^{N_T}. \quad (\text{G2})$$

Following [69], the resulting error can be characterized in the diamond norm and scales as

$$\|(\mathcal{E}_{t/N_T})^{N_T} - e^{t \bar{\mathcal{L}}}\|_\diamond = O\left(\frac{\lambda^2 t^2}{N_T}\right), \quad \lambda := \sum_{a \in \mathcal{A}} \|\mathcal{L}_a\|_\diamond,$$

up to constants that depend on the chosen generator norm and the splitting. We have the freedom to control the value of λ by rescaling the simulation time, $\exp(t \mathcal{L}_a) = \exp((t/c) \times c \mathcal{L}_a)$ for some $c > 0$, then $\lambda = \sum_a c \|\mathcal{L}_a\|_\diamond$.

From an implementation standpoint, each randomized step applies only one elementary dissipative update (one chosen jump channel) rather than deterministically applying all $|\mathcal{A}|$ terms per Trotter step. In our construction, this corresponds to repeatedly implementing primitives of the form $e^{-i \frac{\sqrt{\tau}}{2} \sigma_k \otimes A}$. Therefore, sampling a single jump operator per step can yield a lower per-step cost than deterministic first- or second-order Trotterization, while exhibiting the same asymptotic $O(\lambda^2 t^2 / N_T)$ error scaling in the purely dissipative case. Note that, λ scales with the aggregate strength of the jump channels included in the decomposition. Consequently, when our implementation uses only a small number of jump operators, the increase in λ is modest and does not change the overall asymptotic scaling of the method.

Appendix H: Logical Quantum Circuit Construction for Dissipative Ground State Preparation

The approach of Section G reduces the cost of implementing the entire dissipative evolution over all jump operators simultaneously to the cost of single application of an individual randomly sampled jump operator $\text{Cost}(e^{\tau \mathcal{L}_a})$. Each generator has Lindblad form

$$\mathcal{L}_a(\rho) = K_a \rho K_a^\dagger - \frac{1}{2} \{K_a^\dagger K_a, \rho\},$$

where $\{K_a\}$ are the filtered jump operators defined in Definition 6 and Eq. (A5) and we implement a circuit that realizes a CPTP map $e^{\tau \mathcal{L}_a}$.

For a total time $t = N_T \tau$, one realization of the randomized evolution is the *expected (average) channel* is the mixture over all realizations \mathcal{E}_τ . Define the averaged Lindbladian

$$\bar{\mathcal{L}} := \mathbb{E}_{a \sim \mu} \mathcal{L}_a = \mathbb{E}_a [K_a(\cdot) K_a^\dagger - \frac{1}{2} \{K_a^\dagger K_a, \cdot\}]. \quad (\text{H1})$$

Then the ideal expected evolution at time t is $e^{t \bar{\mathcal{L}}}$ in Eq. (G2).

In practice, we can reduce the required quantum resources to implement the dissipative evolution over the entire jump set \mathcal{A} by randomly sampling jump operators for each time step $e^{\tau \mathcal{L}_a}$ where A_a are drawn i.i.d.. Ding et. al. [20] provide an efficient circuit for implementing the dissipative evolution of a single filtered jump operator K_a that only requires a single ancilla in addition to the system register (excluding ancilla for block encodings). The operator $W(\sqrt{\tau})$ acting on n system qubits and one ancilla qubit that approximates a time step of dissipative evolution for the target Lindbladian \mathcal{L} to second order,

$$e^{\tau \mathcal{L}}[\rho] = \text{tr}_{\text{anc}} [W(\sqrt{\tau})(|0\rangle\langle 0| \otimes \rho)W(\sqrt{\tau})^\dagger] + O(\tau^2). \quad (\text{H2})$$

The quantum resources required to implement the quantum channel generated by $W(\sqrt{\tau})$ are determined by the choice of filter function $f(t)$ that removes heating transitions from the unfiltered jump operators A_a . Theorem 2 establishes a link between two different classes of filter functions and the cost of implementing $W(\sqrt{\tau})$.

Our circuit construction is inspired by the Monte Carlo–style quantum algorithm for ground-state preparation in the early fault-tolerant regime [20], which features a Lindbladian whose target state is stationary. In the paper, the authors design a single-ancilla circuit that simulates a Lindblad dynamics step by splitting the evolution into a purely Hamiltonian part and a purely dissipative part with first-order trotter method with just one extra qubit. Each block is a short interaction between the ancilla and a simple system operator, with the ancilla axis encoding the complex filter coefficient, so the whole channel is built from a sequence of elementary ancilla rotations and controlled interactions. We adapt and extend this in our own circuit design along the reaction path.

A Lindbladian naturally decomposes as $\mathcal{L} = \mathcal{L}_H + \mathcal{L}_a$, where \mathcal{L}_H denotes the coherent part and \mathcal{L}_a the dissipative part. Since the coherent factor does not contribute to energy decrement, we neglect analysis on this direct evolution and focus on the evolution of the dissipative part for our cooling analysis. However, it should be noted that the dissipative cooling primitive is still strongly dependent on the the Hamiltonian: recall that the jump operators are filtered through the time evolution of the Hamiltonian (Eq. (A5)). Discretizing the evolution into time steps of duration τ , the dissipative evolution generated by \mathcal{L}_a can be written as

$$e^{t\mathcal{L}_a} \approx (e^{\tau\mathcal{L}_a})^{N_T}.$$

Therefore, we seek an efficient quantum circuit implementation of the dissipative update $e^{\tau\mathcal{L}_a}$ at each time step. We can follow the recent work [70] in which the authors show that Stinespring dilation can be used to implement dissipative evolution via Hamiltonian simulation and measurement.

Adopting a periodic square-wave filter offers a concrete implementation advantage for simulating $e^{-iK_f\sqrt{\tau}}$ in our scheme. Periodizing the one-sided step in frequency ensures that the corresponding time-domain kernel is a discrete comb rather than a continuous function, so the filtered jump operator K_f naturally decomposes as

$$\int_{-\infty}^{\infty} f(s)A(s)ds = K^{\text{SW}} := \sum_{k \in \mathbb{Z}} c_k A(-kT) \quad (\text{H3})$$

where $A(-kT) = e^{iH(kT)}Ae^{-iH(kT)}$ with equally spaced time shift, and c_k are the Fourier coefficients.

Without any discretization error, the integral K_f can be exactly expressed as K^{SW} and its truncated form at $|k| \leq N_\omega$ corresponds to square-wave filter defined as $K_{N_\omega}^{\text{SW}}$ which approximates the dilated Hermitian jump operator of K_f using one ancilla qubit as follows

$$\tilde{K}_{N_\omega}^{\text{SW}} = \begin{pmatrix} 0 & K_{N_\omega}^{\text{SW}\dagger} \\ K_{N_\omega}^{\text{SW}} & 0 \end{pmatrix} =: \sum_{|k| \leq N_\omega} \tilde{H}_k. \quad (\text{H4})$$

with target leakage $\varepsilon_{\text{leak}}$, i.e., $\|K_{N_\omega}^{\text{SW}}|E_0\rangle\| \leq \varepsilon_{\text{leak}}$. The details of this error bound can be found in the proof of Theorem 2 in Section F.

Equation (H4) can further be factorized as

$$H_k = \begin{pmatrix} 0 & c_k^* A(-kT) \\ c_k A(-kT) & 0 \end{pmatrix} = \sigma_k \otimes A(-kT). \quad (\text{H5})$$

For the square wave, the Fourier coefficients c_k have phases restricted to $\{0, \pm\pi/2\}$, implying that the ancilla generators σ_k lie on the $\{X, Y\}$ axes of the Bloch sphere. This yields an even simpler and more uniform circuit architecture, each step of the evolution consists of a single ancilla–system ‘*jump*’ at a randomly chosen discrete time.

Let $\tilde{A}_k(\sqrt{\tau})$ be the k -th kick. We implement

$$\begin{aligned} \tilde{A}_k(\sqrt{\tau}) &:= e^{-i\frac{\sqrt{\tau}}{2}\sigma_k \otimes A} \\ &= (V_{ai} \otimes I_j) \text{iSWAP}_{ij}(\theta_k) (V_{ai}^\dagger \otimes I_j). \end{aligned} \quad (\text{H6})$$

where $V_{ai} = R_z^{(a)}(\phi)H_a\text{CZ}(a, i)$, where H_a is a Hadamard gate on the ancilla qubit (Fig. 7). Finally, we realize an effective Hamiltonian evolution for two consecutive right-ordered product yields $A(-kT)A(-(k+1)T) = e^{iHkT}Ae^{iHT}Ae^{-iH(k+1)T}$.

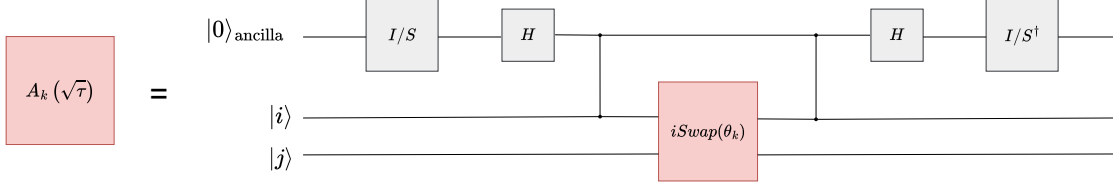


FIG. 7. Circuit for realizing $A_k(\sqrt{\tau}) = \exp(-i\sqrt{\tau}\sigma_k \otimes A_a/2) = \exp(-i\sqrt{\tau}\text{Im}(c_k)\sigma_y \otimes A_a/2)$ for $A_a = (X_i X_j + Y_i Y_j)/2$ using the square wave filter function which only has purely imaginary Fourier coefficients for $\ell > 0$, when $k = 0$, $A_0(\sqrt{\tau}) = \exp(-i\sqrt{\tau}\sigma_x \otimes A_a/4)$, where i, j are corresponding fermionic modes. The circuit costs enough T gates to synthesize 1 R_z gates, 2 acting on the ancilla and the gate decomposition of $i\text{SWAP}(\theta)$ requires only a single R_z leading to a tiny T -gate overhead for implementing local jump operators.

We arrive at a final architecture of a single W operator as implemented by a quantum circuit with a single jump a sampled from the set of the jump operators \mathcal{A} as follows

$$\begin{aligned} & \left[\prod_{|k| \leq N_\omega}^{\rightarrow} (I \otimes e^{iHkT}) \tilde{A}_k(\sqrt{\tau}) (I \otimes e^{-iHkT}) \right] \\ & \times \left[\prod_{|k| \leq N_\omega}^{\leftarrow} (I \otimes e^{iHkT}) \tilde{A}_k(\sqrt{\tau}) (I \otimes e^{-iHkT}) \right] \\ & = (I \otimes e^{-iHS_T}) W(\sqrt{\tau}) (I \otimes e^{iHS_T}), \end{aligned} \quad (\text{H7})$$

where $S_T := N_\omega T$ and

$$\begin{aligned} W(\sqrt{\tau}) := & \left[\prod_{|k| \leq N_\omega}^{\rightarrow} \tilde{A}_k(\sqrt{\tau}) (I \otimes e^{iHT}) \right] \\ & \times \left[\prod_{|k| \leq N_\omega}^{\leftarrow} (I \otimes e^{-iHT}) \tilde{A}_k(\sqrt{\tau}) \right]. \end{aligned} \quad (\text{H8})$$

The quantum channel that we acquire after the exact cancellation of the term $(I \otimes e^{iHkT})$ with the next $(I \otimes e^{-iHkT})$ in Eq. (H7)

$$\begin{aligned} \mathcal{E}_\tau(\rho) := & \text{tr}_{\text{anc}} (W(\sqrt{\tau})(|0\rangle\langle 0| \otimes \rho) W(\sqrt{\tau})^\dagger) \\ & \approx e^{\tau \mathcal{L}^a}[\rho] + O(\tau^2) \end{aligned} \quad (\text{H9})$$

Hence, the total quantum channel averaged over the sampled jump in the set \mathcal{A}_a is

$$\bar{\mathcal{E}} \approx \mathbb{E}_a(\mathcal{E}_\tau^a) \quad (\text{H10})$$

Along the reaction path, if the initial state of the current geometry s_i is ρ_i , then the simulation of Lindbladian dynamics obtains the target state of the corresponding geometry

$$\rho_{s_{i+1}} \approx \bar{\mathcal{E}}(\rho_{s_i}) \quad (\text{H11})$$

where $\rho_{s_{i+1}}$ is also the initial state of the next geometry s_{i+1} .

To implement the jump operator which governs the dissipation part of the Lindbladian Master equation, we follow the structure of [20] by introducing single ancilla qubit for the environment as below

$$\exp\left(-i\frac{\sqrt{\tau}}{2}\sigma_k \otimes A(-kT)\right) = (I \otimes e^{-iHkT}) \underbrace{e^{-i\frac{\sqrt{\tau}}{2}\sigma_k \otimes A}}_{=: \tilde{A}_k(\sqrt{\tau})} (I \otimes e^{iHkT}). \quad (\text{H12})$$

where, $\sigma_0 = |c_0|\sigma_x$ when $k = 0$ and $|c_k|\sigma_y$ otherwise, encoding how strongly the jump operator A is being applied on the system. The operator can also be written as

$$\sigma_k = |c_k|(\cos \phi_k \sigma_x + \sin \phi_k \sigma_y) \quad (\text{H13})$$

where, $\phi_0 = 0$ and $\phi_k = \pi/2$ for $k \neq 0$, with ϕ_k being the phase of the bath correlation defined by the fourier filter $\hat{f}(\omega) = \sum_{k \in \mathbb{Z}} c_k e^{i(\frac{2\pi}{\Omega})k\omega}$. Using the Pauli identity, we can rewrite the expression of σ_k as a sequence of rotation gates

$$\sigma_k = R_z(\phi) X R_z(-\phi) \quad (\text{H14})$$

Then the operation for an arbitrary θ could be realized as

$$\begin{aligned} e^{-i\theta\sigma_k \otimes A} &= (R_z(\phi) \otimes I) e^{-i\theta X \otimes A} (R_z(-\phi) \otimes I) \\ &= (R_z(\phi) H \otimes I) e^{-i\theta Z \otimes A} (H R_z(-\phi) \otimes I). \end{aligned} \quad (\text{H15})$$

We now consider the term $e^{-i\theta Z \otimes A}$, where the operator $Z_{\text{anc}} \otimes A$ induces opposite rotations on the system depending on the ancilla's Z -eigenvalue:

$$e^{-i\theta Z \otimes A} = |0\rangle\langle 0| \otimes e^{-i\theta A} + |1\rangle\langle 1| \otimes e^{+i\theta A} \Rightarrow (CZ_{a,i}) e^{-i\theta A} (CZ_{a,i}) \quad (\text{H16})$$

This holds if and only if every Pauli term in A anticommutes with Z_i , i.e.

$$CZ_{a,i}(P_i) CZ_{a,i} = Z_a^{\text{parity}(P_i)} P_i \quad (\text{H17})$$

where

$$\text{parity}(P_i) = \begin{cases} 1 & \text{if } P_i \in \{X, Y\} \\ 0 & \text{if } P_i \in \{I, Z\}. \end{cases} \quad (\text{H18})$$

In our case, we take $A_a = \{A_{ax}, A_{ay}\}$ as a set of Hermitian operators $A_{ax} = c_a^\dagger c_b + h.c$ and $A_{ay} = i(c_a^\dagger c_b - h.c)$. These two types of operators create a complete set of Hermitian operators. The qubit representation of these two types are $\frac{1}{2}(X_a X_b + Y_a Y_b)$ and $\frac{1}{2}(Y_a X_b - X_a Y_b)$, respectively. Note that, even if $A_{a,b}$ is a non-local operator i.e. a and b are not neighboring qubits in the system, the above condition still holds as $A_{ij} = \frac{1}{2}(X_i S_{i,j} X_j + Y_i S_{i,j} Y_j)$, where, $S_{i,j} = Z_{i+1} \cdots Z_{j-1}$ after JW mapping.

$$\begin{aligned} CZ_{a,i} A C Z_{a,i} &= \frac{1}{2} CZ_{a,i} (X_i X_j) CZ_{a,i} + \frac{1}{2} CZ_{a,i} (Y_i Y_j) CZ_{a,i} \\ &= \frac{1}{2} (Z_a \otimes X_i X_j) + \frac{1}{2} (Z_a \otimes Y_i Y_j) \\ &= Z_a \otimes \frac{1}{2} (X_i X_j + Y_i Y_j) \\ &= Z_a \otimes A. \end{aligned} \quad (\text{H19})$$

Following the identity $U e^A U^\dagger = e^{U e^A U^\dagger}$ and Eq. (H19), we can write

$$CZ_{a,i} e^{-i\theta A_i} CZ_{a,i} = e^{CZ_{a,i} e^{-i\theta A_i} CZ_{a,i}} = e^{-i\theta Z_{a,i} A_i} \quad (\text{H20})$$

The generalized FSim gate

$$\text{FSim}(\theta, \Phi) = \begin{pmatrix} 1 & 0 & 0 & 0 \\ 0 & \cos \theta & -i \sin \theta & 0 \\ 0 & -i \sin \theta & \cos \theta & 0 \\ 0 & 0 & 0 & e^{-i\Phi} \end{pmatrix} \quad (\text{H21})$$

when set to $\Phi = 0$ implements the evolution under $H_{\text{fsim}} = X_i X_j + Y_i Y_j$ i.e.

$$\text{FSWAP}_{ij}(\theta) := i\text{SWAP}_{ij}(\theta) = \exp\left[-i\frac{\theta}{2}(X_i X_j + Y_i Y_j)\right]. \quad (\text{H22})$$

From Eqs. (H15) and (H20), we can implement the circuit as following

$$R_z^{(a)}(\phi) H_a CZ(a, i) i\text{SWAP}_{ij}(\theta_k) CZ(a, i) H_a R_z^{(a)}(-\phi). \quad (\text{H23})$$

where, $\theta = \sqrt{\tau}|c_k|/2$ shown in Figure 7. Note that, to realize A_y , we just need to apply local Z -rotations conjugating $i\text{SWAP}_{ij}(\theta, 0)$ and the above equation looks like

$$\exp(-i\kappa\sigma_k \otimes A_a^{(Y)}) = (I \otimes R_z^{(j)}(\frac{\pi}{2})) \exp(-i\kappa\sigma_k \otimes A_a^{(X)})(I \otimes R_z^{(j)}(-\frac{\pi}{2})). \quad (\text{H24})$$

Operationally, this corresponds to inserting $R_z^{(j)}(\pi/2)$ on fermionic mode j immediately before the $i\text{SWAP}_{ij}(\theta_k)$ block and $R_z^{(j)}(-\pi/2)$ immediately after, leaving the rest of the circuit unchanged.

Finally, we realize that the Hamiltonian evolution from two consecutive modes k and $k+1$ nearly cancels. To see that, recall the filtered jump operator is

$$K_{N_\omega} = \sum_{|k| \leq N_\omega} c_k A(-kT), \quad T = \frac{2\pi}{\Omega}, \quad (\text{H25})$$

with Heisenberg evolution

$$A(-kT) = e^{iHkT} A e^{-iHkT}. \quad (\text{H26})$$

From Eq. (H12), the k -th Fourier mode can be written as

$$U_k := \exp(-i\kappa_k \sigma_k \otimes A(-kT)) = (I \otimes e^{iHkT}) \exp(-i\kappa_k \sigma_k \otimes A) (I \otimes e^{-iHkT}), \quad (\text{H27})$$

for some $\kappa_k \propto \sqrt{\tau}|c_k|$. Taking the ordered product of two consecutive unitaries associated with modes k and $k+1$, respectively, yields

$$\begin{aligned} U_k U_{k+1} &= (I \otimes e^{iHkT}) e^{-i\kappa_k \sigma_k \otimes A} (I \otimes e^{-iHkT}) (I \otimes e^{iH(k+1)T}) e^{-i\kappa_{k+1} \sigma_{k+1} \otimes A} (I \otimes e^{-iH(k+1)T}) \\ &= (I \otimes e^{iHkT}) e^{-i\kappa_k \sigma_k \otimes A} \underbrace{(I \otimes e^{-iHkT} e^{iH(k+1)T})}_{I \otimes e^{iHT}} e^{-i\kappa_{k+1} \sigma_{k+1} \otimes A} (I \otimes e^{-iH(k+1)T}). \end{aligned} \quad (\text{H28})$$

Thus, between neighboring Fourier modes there remains an effective evolution step $(I \otimes e^{iHT})$ of duration T . In our square-wave construction that becomes $I \otimes e^{iH(\pi/2)}$, in the direct correspondence with the discrete-time structure implied by the periodic filter.

Appendix I: Logical Quantum Resources Estimation for Dissipative Ground State Preparation

We estimate the resources for our algorithm in terms of T -gates and logical qubits by explicitly describing the required quantum circuit. Starting from an arbitrary initial state at the first geometry, we apply the CPTP map $e^{\tau\hat{L}}$ until convergence to the target state; this output then serves as the warm start for the next geometry. As the geometry changes, the state drifts from the new ground state, so we reapply our subroutine to approximately prepare the corresponding ground state, and repeat this process along the path. Within the subroutine, a single block $W(\sqrt{\tau})$ is iterated until the state converges to the desired accuracy. Hence, it suffices to estimate the resources for that one block, from which the total cost follows. Along the reaction path, small geometry-dependent variations occur, but the most demanding regime is near the transition state. We therefore report a rough resource estimates which can be obtained by analyzing the single block circuit. A more detailed resource analysis is left to future work.

We use second-order Strang splitting operator $W(\sqrt{\tau})$ with truncated Fourier modes N_ω . The choice of the Fourier modes depends on the Hamiltonian spectral gap Δ . Thus, for each geometry s , the spectral gap of $H(s)$ is different, and therefore we need the most number of Fourier modes N_ω near the transition state. For systems in the milliHartree gap regime $\Delta \sim 0.001$, it suffices to take $N_\omega \geq 1000$ to achieve a sufficiently low leakage bound. Depending on the choice of N_ω , we alternatively repeat the implementation of dilated jump operator $A(\sqrt{\tau})$ and the Hamiltonian simulation circuit according to the Eq. (H9). In the $A(\sqrt{\tau})$ block, the T -cost arises from the implementation of $i\text{SWAP}(-2\theta/\pi)$. For a precision $\epsilon \approx 10^{-5}$, the rough count of T -counts is about 50. To implement each real-time evolution $e^{\pm iHt}$ using quantum singular value transformation (QSVT), which requires N_{U_H} calls the block-encoding unitary U_H per $W(\sqrt{\tau})$.

System	Qubits	Toffolis for $W(\sqrt{\tau})$	Toffolis for QPE
Fe ₂ S ₂ (30e, 20o)	466	2.56×10^8	3.97×10^7
Fe ₄ S ₄ (54e, 36o)	873	1.23×10^9	1.72×10^8
FeMoco (54e, 54o)	1137	1.97×10^9	3.41×10^8
FeMoco (113e, 76o)	1459	8.41×10^9	9.99×10^8
CPD1-P450X (63e, 58o)	1150	3.02×10^9	4.91×10^8
CO ₂ [XVIII] (64e, 56o)	924	1.42×10^9	2.05×10^8
CO ₂ [XVIII] (100e, 100o)	1960	9.00×10^9	1.06×10^9
CO ₂ [XVIII] (150e, 150o)	2870	2.92×10^{10}	2.81×10^9

TABLE II. Qubit counts and Toffoli costs per single dissipative time step $e^{\tau\mathcal{L}(s)}$, implemented by a second-order Strang splitting operator $W(\sqrt{\tau})$ with $N_\omega = 1000$ Fourier modes for the filter function, together with QPE Toffoli counts (for $\sigma_{\text{PEA}} = 1$ mHa) using DFTHC+BLISS+SA block encodings for systems [51].

Appendix J: Reaction path optimization

This appendix records a simple but useful fact: the Davis–Kahan integral

$$C_{\text{DK}} = \int_0^1 \frac{\|\partial_s H(s)\|_2}{\Delta(s)} ds$$

is controlled by a weighted path-length functional of the nuclear trajectory. This provides a direct route for connecting a reaction-path optimization objective (such as the one implemented in our N_3 example) to reductions in C_{DK} , and therefore to reductions in the discretization cost N_H in Theorem 3.

Lemma 8 (Chain-rule bound for the DK integrand). *Let $\mathbf{R} : [0, 1] \rightarrow \mathbb{R}^{3N}$ be a C^1 reaction path and define $H(s) = H_{\text{el}}(\mathbf{R}(s))$. Assume H_{el} is Fréchet differentiable in \mathbf{R} along the image of the path, with derivative $D_{\mathbf{R}}H_{\text{el}}(\mathbf{R}) : \mathbb{R}^{3N} \rightarrow \text{Herm}$. Define the operator-Lipschitz factor*

$$L_H(\mathbf{R}) := \sup_{\|v\|=1} \|D_{\mathbf{R}}H_{\text{el}}(\mathbf{R})[v]\|_2.$$

Then for all $s \in [0, 1]$,

$$\frac{\|\partial_s H(s)\|_2}{\Delta(s)} \leq \frac{L_H(\mathbf{R}(s))}{\Delta(s)} \|\mathbf{R}'(s)\|. \quad (\text{J1})$$

Consequently,

$$C_{\text{DK}} \leq \int_0^1 \frac{L_H(\mathbf{R}(s))}{\Delta(s)} \|\mathbf{R}'(s)\| ds. \quad (\text{J2})$$

Proof. Let $s \in [0, 1]$ be fixed. By the chain rule in Banach spaces,

$$\partial_s H(s) = D_{\mathbf{R}}H_{\text{el}}(\mathbf{R}(s))[\mathbf{R}'(s)].$$

Using the definition of $L_H(\mathbf{R}(s))$ and homogeneity in the direction argument,

$$\|\partial_s H(s)\|_2 = \|D_{\mathbf{R}}H_{\text{el}}(\mathbf{R}(s))[\mathbf{R}'(s)]\|_2 \leq L_H(\mathbf{R}(s)) \|\mathbf{R}'(s)\|.$$

Dividing by $\Delta(s) > 0$ gives Eq. (J1). Integrating both sides from 0 to 1 yields Eq. (J2). ■

Corollary 1 (Uniform bound and a clean geometry surrogate). *Suppose that along the path image one has*

$$L_H(\mathbf{R}(s)) \leq L_{\text{max}} \quad \text{and} \quad \Delta(s) \geq \Delta_{\text{min}} > 0 \quad \text{for all } s \in [0, 1].$$

Then

$$C_{\text{DK}} \leq \frac{L_{\text{max}}}{\Delta_{\text{min}}} \int_0^1 \|\mathbf{R}'(s)\| ds. \quad (\text{J3})$$

In particular, if \mathbf{R} is parameterized by arc-length (so $\|\mathbf{R}'(s)\|$ is constant), reducing the path length $\int_0^1 \|\mathbf{R}'(s)\| ds$ reduces C_{DK} by the same factor.

Proof. Apply Eq. (J2) and upper bound the numerator and lower bound the denominator uniformly:

$$C_{\text{DK}} \leq \int_0^1 \frac{L_H(\mathbf{R}(s))}{\Delta(s)} \|\mathbf{R}'(s)\| ds \leq \frac{L_{\text{max}}}{\Delta_{\text{min}}} \int_0^1 \|\mathbf{R}'(s)\| ds.$$

■

Appendix K: Dissipative Evolution Algorithm Pseudocode

Algorithm 1: Dissipative evolution with reaction-path optimization

Input: Endpoint geometries $\mathbf{R}_R, \mathbf{R}_P$, target geometry s^* , target energy error ϵ_E , jump set \mathcal{A} , filter function $\hat{f}(\omega)$

Output: Approximate transition-state ground state ρ^* and energy estimate E^*

- 1 Choose an initial reaction path $\mathbf{R}_0(s)$ connecting \mathbf{R}_R and \mathbf{R}_P ;
- 2 Optimize the path by minimizing

$$J(\mathbf{R}) = \lambda_{\text{len}} \int_0^1 \|\mathbf{R}'(s)\| ds + \lambda_{\text{curv}} \int_0^1 \|\mathbf{R}''(s)\|^2 ds + \lambda_{\text{CI}} \int_0^1 \Phi_{\text{CI}}(\mathbf{R}(s)) ds$$

to obtain a smooth path $\mathbf{R}(s)$ that avoids sharp projector rotation and small-gap regions;

- 3 Discretize the optimized path into $\{s_i\}_{i=0}^{N_H-1}$ with $s_0 = 0$ and $s_{N_H-1} = s^*$;
- 4 For each s_i , build the electronic Hamiltonian

$$H_i = H_{\text{el}}(\mathbf{R}(s_i))$$

and align neighboring orbital spaces to maintain a smooth gauge along the path;

- 5 Prepare an approximate ground state ρ_0 for H_0 using a tractable classical or hybrid method (e.g., DMRG + dissipative cooling) ;

- 6 **for** $i = 0$ **to** $N_H - 2$ **do**

- 7 Construct filtered jump operators $\{K_a^{(i+1)}\}_{a \in \mathcal{A}}$ for H_{i+1} ;

- 8 Starting from ρ_i , apply the dissipative primitive for t_i steps to obtain

$$\rho_{i+1} \approx \left(e^{\tau \mathcal{L}_{i+1}} \right)^{t_i} (\rho_i),$$

where

$$\mathcal{L}_{i+1}[\cdot] = \sum_{a \in \mathcal{A}} K_a^{(i+1)}(\cdot) K_a^{(i+1)\dagger} - \frac{1}{2} \left\{ K_a^{(i+1)\dagger} K_a^{(i+1)}, \cdot \right\}.$$

- 9 Set $\rho^* \leftarrow \rho_{N_H-1}$ and estimate

$$E^* = \text{Tr}(H_{N_H-1} \rho^*).$$

- 10 **return** (ρ^*, E^*) ;
-